CORRECTION OF IMAGE DISTORTION IN ECHO PLANAR IMAGE SERIES USING PHASE AND INTENSITY

By

Ning Xu

Dissertation

Submitted to the Faculty of the

Graduate School of Vanderbilt University

in partial fulfillment of the requirements

for the degree of

DOCTOR OF PHILOSOPHY

in

Computer Science

May, 2008

Nashville, Tennessee

Approved:

John Michael Fitzpatrick

Robert E. Bodenheimer

Benoit M. Dawant

J. Christopher Gatenby

John C. Gore

Cynthia B. Paschal

ACKNOWLEDGEMENTS

This work would not be possible without the help and support from many people in the past five years.

I am grateful to have Dr. J. Michael Fitzpatrick as my academic advisor. We have been through the most important and difficult part of my Ph.D. study together. He taught me a lot in mathematics, physics, and more importantly, the attitude towards scientific research. I would like to thank him for his patience, generous support, and valuable advice on every piece of work that I have done. This Ph.D. thesis would not be complete without his generous praise and encouragement.

I would like to acknowledge my committee members: Dr. Robert E. Bodenheimer, Dr. Benoit Dawant, Dr. Christopher Gatenby, Dr. John Gore, and Dr. Cynthia Paschal. It is my great pleasure to have so many great professors as my committee members. I would like to express my gratitude for their valuable feedbacks and help on my Ph.D. work. I would also like to thank other professors that I worked with: Dr. Victoria L. Morgan, Dr. David Pickens, and Dr. Ronald L. Cowan.

I would like to thank Dr. Duane Yoder who helped me to get familiar with this field. Dr. Yansong Zhao was very helpful getting me familiar with imaging hardware. I am grateful to collaborate and share ideas with Dr. Yong Li. I would also like to thank all the members in the MIP lab at Vanderbilt. This is a great environment, and I enjoyed being one of them.

Finally, I give my great gratitude to my family. Their support and understanding has been at the bottom of my heart, but has been the source of my confidence and inspiration.

TABLE OF CONTENT

Page

LIST OF FIGURES

Figure Page

LIST OF TABLES

Table Page

CHAPTER I

INTRODUCTION

1.1. Introduction

Magnetic resonance image is a modern imaging modality providing non-invasive access for diagnosis of soft tissue of both human and animals. It has variety of clinical and neurological applications. Among many of the existing MR imaging sequences, gradient-echo (GE) echo-planar imaging (EPI) [1], which can acquire a human brain image within seconds, has become the most common technique for the study of dynamic brain function, using, for example, in-vivo diffusion-tensor imaging [2-5] and perfusion imaging [6-10], for other high-speed applications like cardiac imaging [7;8;11], as well as for basic neuroscience investigations, presurgical planning, and post-therapy evaluation.

However, the usefulness of GE-EPI is limited by the severe geometric and intensity distortion caused by the inhomogeneity in the static magnetic field, which is present to some degree in all MR images but most prominent in GE-EPI. The magnetic field inhomogeneity, while partially caused by imperfect hardware, is largely induced by the susceptibility differences between air and tissues or bone and tissue of the subject being imaged. Hence, field inhomogeneity induced image distortion is also called a "susceptibility artifact". The artifacts are most pronounced around sinuses in human brain imaging. We denote the inhomogeneous field, or "distortion field", as ΔB in this dissertation. Since the magnitude of ΔB caused by susceptibility is proportional to the applied static magnetic field, B_o, larger distortion fields are found in MR scanners with

higher fields. As we will see later, ΔB introduces extra phase in the MR image formation process and degrades the image reconstruction. It has been mathematically proved that these phase errors will cause geometric and intensity distortion in EPI that are acquired with a Cartesian k-space sampling pattern [12;13] and will cause blurring in EPI acquired with a spiral pattern [14], in both cases reducing the accuracy of localization of the image anatomy and of functional analysis. For standard spin-echo (SE) and GE MR images, there is no phase evolution in the phase-encoding direction, so the image distortion is

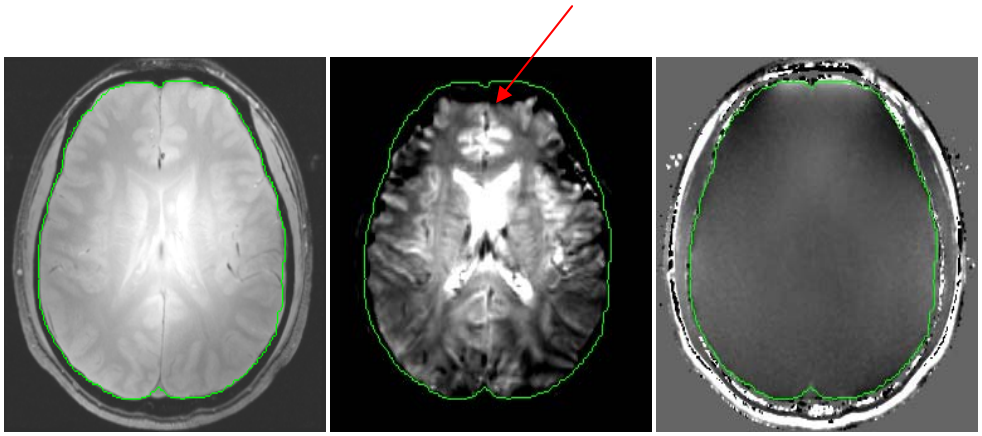

(a) **(b)** **(c)**

Figure 1. MR images and the corresponding field map from Philips Intera Achieva 7T MR scanner. The field of view is 192 mm with the read-out left to right and phase-encoding top to bottom. (a) standard GE: TE/TR= 5/500 ms, 256x256 matrix (b) GE-EPI: TE/TR= 25/990 ms, 128x128 matrix, EPI factor 63 (2 shots) (c) B_o field map: 128x128 matrix. The green outline from (a) is superimposed on (b) and (c), revealing severe distortion in EPI relative to the GE image, especially anteriorly (indicated by a red arrow).

confined to the frequency-encoding direction, also known as the "read-out" direction, and the slice-selection direction. Unlike a standard acquisition, in which each line of *k*-space is acquired in a separate shot, for EPI all *k* -space lines are acquired in one shot or a few shots, both for SE-EPI and for GE-EPI. Hence the phase errors caused by the distortion

field evolve in the phase-encoding direction as well. If the frequency-encoding direction is along x and the phase encoding is along y, then the effective time to traverse one k_y line is about N time longer than one k_x line for a single-shot EPI, where N is the number of lines in the phase-encoding direction with N typically equal to 64 or 128. The severity of the distortion in a given direction is proportional to the time required for the traversal in that direction. The time required for a k_x line is short enough to keep the distortion at a negligible level. Hence the image distortion lies primarily in the phase-encoding direction in EPI and can be quite large [15]. The distortion pattern depends on the inhomogeneity pattern—information which is not present in the reconstructed information. In theory, an accurate field inhomogeneity map can be transformed into a distortion field, which allows us to solve an inverse problem to restore the lost information in the distorted MR image and produce an undistorted MR image. We call the production of an undistorted MR image "distortion correction" in this dissertation. Figure 1 shows (a) a standard multi-shot GE image, (b) a GE-EPI, and (c) the corresponding field inhomogeneity map of the same human subject in Philips Intera Achieva 7T MR scanner. The green line was drawn on the undistorted GE (a) and then superimposed on the EPI (b). Areas where the edges of the EPI do not match the contour of GE indicate that severe image distortion exists in the phase-encoding direction (vertical). They are particularly pronounced at the top (anterior) of the head (indicated by a red arrow) where large gradients in susceptibility exist because of differences arising near the sinuses.

In addition to the static component of field inhomogeneity caused by the susceptibility differences at tissue boundaries, fluctuations in the magnetic field with time, induced by physiological processes such as cardiovascular pulsation and respiration, have been observed in most rapid brain imaging such as functional MRI (fMRI). Moreover, the fact that the subject's head cannot remain still during a long imaging scan makes dynamic image series suffer from bulk motion. Although rigid-body registration has been employed successfully to correct motion among dynamic scans, considerable movement-related effects caused by rotation still remain and cannot be removed easily. The static-field inhomogeneity is determined not only by the spatial distribution of the magnetic

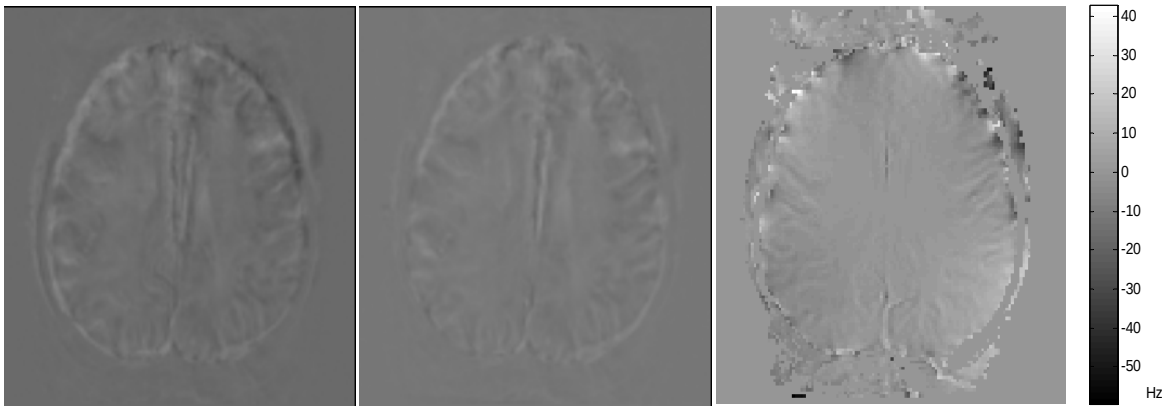

Figure 2. Effect of fluctuations in magnetic field effects on dynamic image series. (a) magnitude difference between two images acquired at two different time points (b) magnitude difference after the two images are realigned by rigid-body registration (c) fluctuation in magnetic field. The non-uniformity of (b) shows that temporal variation in image intensity in dynamic series may not be successfully removed by means of rigid-body registration.

susceptibility but also by the direction of the static magnetic field, B_o relative to the anatomy [16;17]. As pointed out by Jezzard *et al*. [17] and Andersson *et al.* [16], rotation of the object with respect to the applied field alters that relative direction, resulting in a

change in the induced field, and the change is not a rotation of the field. .Figure 2 shows (a) the magnitude difference of two images at two different time points, (b) the magnitude difference of these two images after they are registered using a rigid-body realignment, and (c) the variation of the magnetic field inhomogeneity between these two time points. The large variation in image intensity shown in (b) indicates that rigid-body registration may not successfully remove temporal variations of image intensity in EPI series. The variation of the field inhomogeneity shown (c) indicates that the variation shown in (b) may be due to the fluctuations of magnetic field inhomogeneity.

1.2. Contribution

The focus of this work is the reduction of distortion in EPI series of the brain. It is well known that inhomogeneity in the static field causes spatial variation in the phase of complex MR images, and methods to determine the inhomogeneity from this variation have been termed "field-map" methods. In this work, we introduce an extension of the traditional field-map method, which we will call the "phase-map" method, to accomplish the calculation of inhomogeneity as it changes dynamically throughout the acquisition of a series of GE-EPI images. Our method is based on the idea that the variation of the distortion field is encoded in the temporal phase changes of the EPI. If the distortion field varies sufficiently slowly with time, we can calculate the distortion field for a given EPI based on the distortion field of the previous EPI and their phase differences. Given this distorted field for each EPI, the geometric distortion and the intensity distortion caused by local compression or stretching can be corrected. However, calculation of this field and the correction of image distortion based on this field is made difficult by noise in the

signal and motion of the anatomy. The major contribution of this work is the correction of image distortion in an EPI series in the face of this noise and motion.

The difficulty with noise arises from the fact that the temporal phase changes are small making the field calculation highly sensitive to noise in EPI. We develop a regularization method based on both the phase and the intensity of the image data to reduce the estimation errors. The regularization helps both to produce smoother distortion fields and to extrapolate the estimated field into areas where the SNR is low. The corrected images based on the regularized distortion field have a better image quality than images corrected without the regularization.

The difficulty caused by motion arises from the fact that motion of the anatomy is different from the motion of the image because motion of the anatomy also changes the inhomogeneity patterns. Changes in inhomogeneity lead to changes in image distortion, and the resulting interaction of motion and distortion results in critical issues in the analysis of EPI series. Image registration has been proven to be successful for motion compensation and distortion correction of a single EPI. In this work, we study the methods of using intensity based registration to correct the dynamic distortion of EPI series in the presence of motion, and we suggest a motion compensation strategy based on corrected EPIs. We incorporated a phase-gradient term into an optimization framework for distortion correction of EPI series. The objective function we developed accounts for not only the traditional intensity similarity but also a similarity in the gradient of the distortion field derived from the image phase. Our new phase-gradient term enforces an additional constraint on the estimation of the distortion fields in EPI series using registration methods.

To test the methods that we have proposed to solve these problems, we perform a validation of our proposed methods based on two types of images with known ground truth. Instead of using real human data, which has unknown ground truth and unknown sources of intensity variation, we use simulated images and images of a physical phantom. The simulated images are brain images with realistic motion and image distortion. Our physical phantom is carefully designed to provide a known geometry. Using the simulation and phantom images, we conduct quantitative studies of the performance of our methods in the correction of dynamic image distortion in EPI time series. We also quantify improvements of our methods over existing methods. Finally, we compare different strategies for distortion correction of EPI series in the presence of motion and a varying distortion field and analyze their performance.

1.3. Chapter summaries

The work in this dissertation is organized as follows. Chapter I presents an introduction of this work followed by a summarization of the main contributions of this dissertation.

Chapter II presents the background of this work. The sources of and the nature of the image distortion in EPI series are discussed. Extensive research on existing distortion correction methods in the literature is presented and discussed.

Chapter III starts with a review of EPI formation in the presence of field inhomogeneity. The mathematical formulation of both geometric distortion and intensity distortion is presented. The principle of the traditional field-map method is reviewed. A phase-map method to calculate the dynamic distortion fields based on the temporal phase

changes is proposed. A phase regularization method for the estimation of dynamic distortion fields is described in detail. Finally, the method for correction of EPI series based on dynamic distortion fields is given.

Chapter IV centers on the utilization of image registration methods in the estimation of dynamic distortion fields. Specifically, the limitations of the image registration methods in correction of EPI series are discussed. In order to overcome these limitations, the integration of a phase-gradient term into the registration framework is proposed. A method to calculate the gradients of the distortion field for each EPI based on a wrapped image phase is developed. Finally, an algorithm that utilizes both intensity and phase information from the image to correct the dynamic image distortion is presented.

In Chapter V, a validation of the two methods that we proposed in Chapter III and Chapter IV is conducted based on both simulated brain images and real data of a physical phantom. Experiments to quantitatively analyze and evaluate the performance of our methods based on known ground truth are described. The improvements of our methods are shown by comparing them to the traditional field-map method and to the standard non-rigid registration method. Finally, different strategies for estimation of dynamic distortion fields of an EPI series in the presence of motion and a varying distortion field are compared.

Chapter VI concludes by providing a summary of the work presented in this dissertation accompanied by possible future work regarding distortion correction of EPI series.

CHAPTER II

BACKGROUND

MR imaging is widespread nowadays and routinely used in many clinical settings because it provides excellent contrast for soft tissue. GE-EPI, as a rapid imaging technique, is commonly used in dynamic imaging applications such as fMRI. However, image distortion induced by field inhomogeneity, which is present in all MR images, is severe in GE-EPI with both geometric and intensity distortion being observed in the reconstructed images.

In this chapter, we begin by briefly introducing and describing the sources of, and the nature of, geometric distortion and intensity distortion in MR images, especially that of GE-EPI. Specific issues of image distortion for EPI series are discussed. Existing methods of distortion correction in the literatures are classified and summarized in detail.

2.1. Image distortion in GE-EPI

GE-EPI, which is the most widely used technique for fMRI due to its speed and sensitivity to blood oxygen level dependent (BOLD) contrast [18-22], is strongly affected by inhomogeneity in the static magnetic field, which cause both image warping and spurious changes in intensity. The changes in intensity produce errors in the functional measurements, and the warping causes errors in mapping of measured brain function to anatomical images. Warping is present in all MR images, although the severity of the distortion is dependent on MR sequence type, the trajectory by which the signal data array (k -space) is filled, and field strength, with high fields, as desired for fMRI,

aggravating the problem. Field inhomogeneity arises from errors in the applied field and, more critically, variations in the induced field. The induced field is a function of the complex 3D map of the magnetic susceptibility of the subject [23]. Since different tissues have different susceptibilities, the fields induced vary locally and influence the field in surrounding regions. Chemical shift differences and time-varying imperfections imposed by eddy currents also distort the field. The result is that the field is far from the uniform ideal, especially near the frontal sinus, nasal cavity, and temporal bone, where abrupt spatial changes in susceptibility cause large variations in the field.

With its high temporal resolution and relatively high spatial resolution, especially as compared to positron emission tomography, event-related potentials, and magnetoencephalography, GE-EPI is now used to study dynamic brain function and has applications in basic neuroscience investigations, presurgical planning, and post-therapy evaluation. Unfortunately, in many ways, GE-EPI has become a "black box" technique, used by many investigators who may be unaware of the complexity and limitations of EPI. The accuracy of this approach in functional localization of human brain is limited by spatial distortion as great as 4 pixels out of 64 [24], dramatic signal loss near the frontal sinus, nasal cavity, and temporal bone [25], and subject motion between image acquisitions [26;27]. Image distortion and signal loss in GE-EPI hamper the study of a host of brain functions including language [28;29], memory [30], and olfaction [31]. EPI is also used for *in-vivo* diffusion-tensor imaging [2-5;32], perfusion imaging [6-10], and other high-speed applications like cardiac imaging [7;8;33]. The importance of accuracy in the findings from fMRI studies and from these other EPI applications all urgently motivates the development of methods to correct for image distortion.

The distortion comes in two forms—geometrical distortion and intensity distortion. The latter distortion comprises two types. The first is present for both GE and SE sequences. It is a spurious amplification or diminution of image intensity in regions where the image is compressed or stretched, respectively. Because this latter effect can be modeled mathematically by the Jacobian of the geometrical distortion (more precisely, its determinant) [13], we will call it the Jacobian factor. The second type of intensity distortion is the result of intravoxel dephasing and is present only for GE images. In this work, we will focus only on the intensity distortion that can be corrected with Jacobian–distortion caused by local compression or stretching.

2.2. Single EPI versus EPI series

EPI is a fast imaging technique with a temporal resolution of several seconds. An EPI time series, including hundreds of volumes, is often utilized for temporal image analysis. For example, the acquisition of an EPI time series is a routine protocol for statistical analysis of brain functions in fMRI. Relatively long acquisition times make the images suffer from physiological motion induced by head motion, cardiac motion, and respirations, etc. The concomitant variations of field inhomogeneity in time caused by motion induce confusion in image analysis. Even after realignment, EPI time series still suffer from residual movement-related effects which may cause erroneous analysis and false conclusions.

The static-field inhomogeneity induced by a human subject is determined by the spatial distribution of magnetic susceptibility relative to the direction of the impressed static-field, B_o [16;17]. Translational motion has no effect on distortion, but rotational

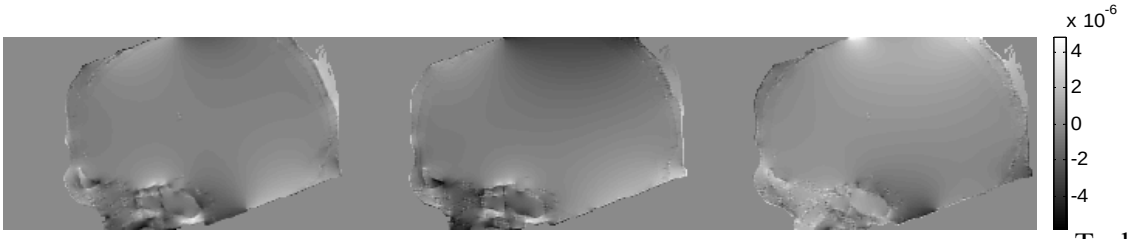

Figure 3. Interaction of field inhomogeneity and motion. (a) is the rotated field map of a head. (b) is the field map of the rotated head. (c) is (a) minus (b). The nonuniformity of (c) reveals the variation of field inhomogeneity induced by head motion.

motion can change its patterns. We will call the type of motion "out-of-plane" motion when the rotation is along an axis other than the B_o direction. The plane referred to here is the one perpendicular to B_o —not necessarily the imaging plane. All other types of motion will be classified as "in-plane" motion. The interaction between motion of the imaged anatomy and distortion will be denoted as "motion-distortion" in the following. To take a close look at this effect, we have calculated two different field maps using an MR simulator [23] with the head of the subject in differing orientations. For comparison, we also simply rotated the field map from orientation 1 to orientation 2. Figure 3 shows a comparison between the rotated field map of a head (a) and the field map of the equivalently rotated head (b). The maps are not the same, as shown by the difference image in (c), which reveals the variation of field inhomogeneity induced by head motion.

The temporal variation of image intensity in an EPI time series is induced by the effect of motion-distortion and by respiration. To understand the resulting distortion patterns it is important to note that the direction of the geometric distortion lies primarily along the phase-encoding gradient. The direction of that gradient during a series acquisition is fixed with the scanner's coordinate system regardless of subject motion. So,

therefore, the direction of the distortion is also fixed with the scanner. Hence if the head is rotated about an axis other than the phase-encoding direction, then the direction of the distortion relative to the head will change, resulting in an effect of motion-distortion. Furthermore, if the head is rotated out-of-plane (see the definition in the preceding paragraph), the magnitude of the distortion field will change and hence the magnitude of the distortion will change as well. These changes arise because the distortion fields are determined not only by the pattern of the susceptibility of the imaging subject but also by the direction of its distribution relative to the static field. Variation due to out-of-plane rotation is a second example of the effect of motion-distortion. Combinations of these effects can occur as well.

A source of temporal variation of the distortion fields in addition to out-of-plane rotation is respiration [34]. Bulk susceptibility variation in the lungs during respiration causes variation in the field inhomogeneity of human head. Image shift and intensity changes in the phase-encoding direction have been noticed during respiration. Variation of the distortion patterns caused by motion-distortion and respiration is the major source of erroneous temporal changes in EPI time series and could cause spurious activation analysis and reduce the significance of true activation.

2.3. Existing distortion correction methods

Numerous techniques for image distortion correction have been proposed. Approaches based on the separate acquisition of a field map are most widely used. A map of static-field inhomogeneity is first measured and the distorted image is warped back to undistorted space according to a relation between the field inhomogeneity and image

distortion. Sekihara *et al.* [35] proposed a method for measuring a field map using an asymmetric spin-echo sequence, where the time interval between the 90^o RF pulse and the 180^o RF pulse is set to be different from the time interval between the 180^o pulse and the spin-echo formation. The field inhomogeneity information can be extracted from the phase shift at each point in the reconstructed image. Sumanaweera in 1993 [36] and Jazzard and Balaban in 1995 [15] suggested using two GE images differing in the values of their echo times (TE). The phase differences between the two reconstruct images were used to calculate a field map. In practice, multiple gradient-echo images are acquired to correct the phase wrapping problem.

Kadah and Hu [37], Munger *et al.* [38] formulize the MR image formation process in the presence of static-field inhomogeneity as a linear equation system in a matrix form. The matrix can be constructed given the field inhomogeneity for each voxel. The solution from approximate matrix inversions gives an image with reduced image distortion.

Typically it takes about minute of scan time to obtain a field map. Unfortunately, a minute is a very long time when compared with the two seconds typically required for each EPI acquisition in the typical time series acquisition, and it is short time with respect to changes in the field due to changes in head orientation and with respect to changes in the field due to respiration. Thus, with the use of the field map the quality of distortion correction of a series of images that are acquired before or after the field-map acquisition can be seriously degraded by head motion. To reduce the scan time for field mapping, Reber *et al.* [39] propose to use two EPIs differing in the values of their echo times to compute a field map. Because the EPIs are geometrically distorted, the field map

calculated from EPIs will be warped the same way as the EPIs. With a field map acquired via EPIs the correction method is slightly different from that with a field map acquired via GE images.

Rather than measuring a field map, some groups [40-44] propose to measure the phase modulation caused by static-field inhomogeneity directly from multiple reference scans and use the measured phase modulation to generate a modified *k*-space data. A corrected image is then generated after taking the Fourier transform. This technique collects information from multiple reference scans and encodes the phase errors coming from field inhomogeneity, eddy current and chemical shift. However, the prolonged acquisition time required for this method is not affordable for most imaging studies.

A technique based on a spatially varying point-spread function employs an additional phase-encoding gradient along any of the spatial directions, which enables the measurement of a point-spread function for each image voxel directly so that the geometric distortion for each voxel is known accordingly. This technique was originally proposed by Robson *et al.* [45] and later used for image distortion correction [46;47]. This correction method incorporates the image distortion coming from various sources such as static-field inhomogeneity, eddy current, and chemical shift. However, as for the method based on multi-reference scans, a prohibitively long acquisition time is required.

Another retrospective technique for image distortion correction is based on non-rigid registration of the distorted images to other images of the same subject [48-50]. For example, in fMRI applications, in addition to an EPI time series, a so-called "anatomical image" is acquired by means of a different acquisition protocol. The anatomical image has negligible distortion and much higher resolution than the EPI, but requires a longer

scan time. While adequate distortion correction can be achieved with these methods under some circumstances when smoothly varying functions are incorporated, one would not expect the correction to be as accurate as those methods where each voxel is corrected individually based on prior-knowledge. Furthermore, image distortion in an EPI of the head is very local. A large number of degrees of freedom are needed to model the distortion field, which prolongs the correction process. In addition, EPI often has low resolution and suffers from signal loss in some regions, which makes it difficult to register the EPI to an anatomical image.

Some other techniques attempt to minimize errors in the applied and induced fields by means of shimming either globally or locally [51-53], although this is typically insufficient. More complex shimming techniques calculate a field map (via chemical-shift imaging [54;55], phase-sensitive imaging [56;57], multiple spin-echo images [12;35;58], or double-echo gradient-echoes [59], and then a corrective field is fit to the field map [55-57] and implemented as well as possible by the shim coils [59].

Forward-reverse methods, also known as gradient-reversal methods, which involve two acquisitions with reversed gradients and thus reversed geometric distortion, have been investigated by Chang & Fitzpatrick and several other groups [13;60-69]. While these studies have demonstrated useful corrections at low fields and small distortion, the utility of forward-reverse at high fields, where the distortion will be much larger, is likely to be limited. The primary problem is that the basic assumptions of the method are violated by the presence of noise, and the violation increases strongly with increasing distortion. Efforts to solve the problem by means of new algorithms for combining the forward and reversed images have been advanced by Kannengiesser [64],

Anderson and Skare [65;67], Reinsberg *et al.* [63;68], and recently Weiskopf *et al.* propose a modification of the method that involves the acquisition of a third image [66]. A requirement of the forward-reverse methods is that at least one pair of corresponding points be identified in each line of the image. The identification of corresponding points in two images that have poor image quality and severe signal loss is problematic and prevents its *in-vivo* use in such situations.

The parallel imaging method called "SENSitivity Encoding" (SENSE) [70] reduces warping in EPI by reducing the required number of phase encodings, which reduces the time spent sampling *k*-space, but it also decreases the SNR. Alternatively, higher in-plane resolution can also be achieved using parallel imaging, so the effects of in-pane intravoxel dephasing are expected to be reduced, although with the reduction of SNR and with minimal or no reduction in warping.

The majority of the existing techniques for distortion correction are limited in the ability to correct EPI time series because only a single field map or distortion field is obtained or modeled for correcting the distortion in the entire series. While they are effective when there is negligible change in the inhomogeneity pattern between the map-measurement scan and the EPI scans, these techniques may fail when gross motion or physiological activity is present during the acquisition of the dynamic scans. The temporal variation of field inhomogeneity results in varying image distortion, and the image distortion in an EPI time series cannot be corrected accurately using a single field map. Hence, in the process of field mapping it is desirable to account not only for the inhomogeneity before or after the series is acquired but also for the changes in

inhomogeneity throughout the series—both changes that are caused by gross motion of the head and those caused by physiological changes in anatomy outside the head.

To determine these changes in inhomogeneity, some groups have explored the possibility of acquiring a separate field map for each scan of the series. Hutton *et al.* [71] suggest acquiring a series of extra EPIs to compute multiple field maps and performing the distortion correction for each image in an fMRI time series individually. Unfortunately the time for the series acquisition is doubled in this way and, more importantly, the temporal resolution of the temporal signal is cut in half. Roopchansingh *et al.* [72] propose a dynamic field-mapping method with the field map acquisition embedded in the EPI pulse sequence. Unfortunately, only a very low resolution field map can be obtained in this way because of T2* decay, and the reduction in resolution results in a reduction in accuracy of the correction. Navigator echoes [73-75] have been employed to measure the phase changes induced by physiological effects, but the assumptions are that the variations of field inhomogeneity caused by physiological activities are either global or linear in space, which is invalid because the spatial variation of the physiological effects is not necessarily linear [76].

2.4. Phase method versus intensity method

A field map can be derived directly from image phase. With the phase evolution induced by ΔB from two GE images, a map of field inhomogeneity can be calculated. The field map accurately determines image distortion because there is a simple proportionality relation between a field map and the corresponding image distortion and the proportionality constant is determined by the known strength of an image-acquisition

gradient. Unfortunately, the field-map method did not find its role in the correction of dynamic image distortion in EPI series because normally an extra scan is necessary for the calculation of the distortion field for each time point. The resulting reduction in temporal resolution is not affordable in applications requiring fast imaging. There is a need to develop new techniques for dynamic field mapping to correct the image distortion of EPI series. In later chapters, we will see that not only a static distortion field but also a series of distortion fields can be estimated from temporal phase evolution.

Another class of methods for the correction of image distortion is based on image intensity. In these methods, a distortion field is estimated from image intensity rather than image phase. The distortion field is either calculated for each voxel, such as in the forward-reverse method [13] or modeled as a non-linear function, as in the non-rigid-registration method [77]. The idea of image intensity methods for distortion correction is to find a template image which has either minimal distortion or opposite distortion. The distortion field is then estimated by finding the spatial correspondence between the distorted image and the template image automatically. Once the correspondence is identified, the distortion field is calculated straightforwardly.

Non-rigid registration has the advantage over standard field-map methods of not requiring extra scan time. Its greatest disadvantage is problem sub-optimal local minima, and it also suffers from slow convergence whether or not it is trapped in a suboptimal local minimum. Both problems are made worse by the requirement that a large number of degrees of freedom need to be optimized. A review of existing methods for distortion correction via non-rigid registration can be found in [78]. Several groups have explored the feasibility of using non-rigid methods to correct for EPI, but the majority of these

methods are confined to correcting the distortion of a single EPI. The application of non-rigid registration methods in correcting dynamic distortion of EPI time series has yet been fully explored. There are two major problems when we apply non-rigid registration methods to the problem of correcting dynamic image distortion. First, motion is present in all EPI time series. Although rigid-body realignment can compensate for motion to a large extent, inaccurate motion compensation induced by dynamic distortion fields can result in false warping when a non-rigid registration is applied afterwards. The false warping is a critical problem for temporal data analysis. Andersson *et al.* [16] introduce a mathematical model to account for the effect of motion-distortion in their intensity based method. However, their method is also based on the assumption that an accurate motion compensation is provided by some other means and that the variation of the distortion fields can be approximated as a first order Talyor expansion in of the motion components.

Another limitation of non-rigid-registration for distortion correction is that the distortion field is modeled as a non-linear function with a large number of degrees of freedom. The distortion field is estimated by performing a non-linear optimization, which is prone to find a suboptimal local minimum when the number of unknown parameters is large [79]. To reduce these problems various constraints based on the physics of the imaging process have been developed to limit the space of optimization in the methods based on non-rigid registration.

2.5. Relationship of this dissertation to the state of the art

This dissertation is focused on the reduction of distortion in series acquisitions of EPI of the brain. In particular, it is concerned with geometrical distortion and with intensity distortion that results from compression or stretching in the geometrical distortion pattern. Existing methods are based on shimming, field-mapping, or image registration. Shimming is incapable of handling the complex distortion patterns caused by the susceptibility of the head. Field-mapping methods are available only for static inhomogeneity, which requires that the head not move and respiration cease, for dynamic inhomogeneity when temporal resolution can be sacrificed, or for dynamic inhomogeneity with linear spatial variation. Registration methods suffer from the requirement that the distortion pattern be modeled by a spatial function of high dimensionality leading to suboptimal solutions and false warpings. At present no reliable method exists for the determination of distortion maps that accommodates dynamic inhomogeneity with full temporal resolution and accurate spatial variation. The focus of this dissertation is to develop methods to generate such dynamic maps efficiently and accurately.

We present two methods in this dissertation for the estimation of dynamic distortion maps in GE-EPI time series. They are presented in Chapter III and Chapter IV, respectively. Their validation is presented in Chapter V.

CHAPTER III

ESTIMATION OF DYNAMIC DISTORTION FIELDS VIA PHASE MAPS

In this Chapter, a method to estimate dynamic distortion fields in EPI time series via phase maps is introduced. Acquiring a field map with extra scans for each EPI individually is typically not affordable for most fast imaging applications. The temporal changes of distortion fields, however, are encoded in the phase changes of the distorted EPIs themselves. When the distortion fields vary sufficiently slowly with time, which is a valid assumption during fast imaging scans, such as EPI, the temporal changes of the image phase have minimum or correctable phase wrapping. Hence, the temporal phase changes provide useful information to generate a separate distortion field for each EPI in a time series.

Given a field map for each time point, the image distortion of each EPI can be corrected individually. The estimation errors of the distortion field caused by noisy phase could potentially introduce artifacts into the corrected EPI. As a result, regularization of the estimated field is necessary and has a large influence on the image quality of the corrected images. In this chapter, we extend an existing approach for field-map regularization. A regularization term is incorporated into a maximum likelihood (ML) framework in which the regularized distortion field for each time point is calculated iteratively.

In this chapter, we start with an overview of MR image formation in the presence of field inhomogeneity. The geometric distortion and intensity distortion of EPI image are formularized. This is followed by an introduction of our phase-map method for the

estimation of dynamic distortion fields. A regularization approach for the phase map is described in detail. In the end, the distortion correction method for EPI time series using dynamic fields is described.

3.1. GE image formation in the presence of magnetic field inhomogeneity

Considering a multi-slice MR image sequence, a slab of spins of a slice of interest at z_1 is excited by an RF pulse and a slice-selection gradient. The frequency-encoding gradient and phase-encoding gradient at time t are represented by $G_x(t)$ and $G_y(t)$. The image signal s received by the RF coil in a rotating frame can be represented as follows:

$$s(t) = A\iint \rho(x,y,z_1)\, e^{-\frac{t}{T2^*(x,y)}} \left(1 - e^{-\frac{TR}{T1(x,y)}}\right) e^{-i2\pi\gamma\left(x\int_0^t G_x(t')dt' + y\int_0^t G_y(t')dt'\right)} dxdy, \qquad (1)$$

where $\rho(x,y,z_1)$ is the spin density, γ is the gyromagnetic ratio ($\gamma = 42.5774\times10^6$ Hz/Tesla for hydrogen and $\gamma = 2\pi\gamma$), A is a scaling constant, T1 and T2* represent longitudinal relaxation time and transverse relaxation time, respectively, and TR is the repetition time. The integral in Eqn. (1) is over 2D image space. We define

$$\begin{aligned} k_x &= \gamma\int_0^t G_x(t')dt' \\ k_y &= \gamma\int_0^t G_y(t')dt' \end{aligned} \qquad (2)$$

Ignoring the T1 and T2* effects, we can write Eqn. (1) as

$$s\left(k_x,k_y\right)=A\iint\rho\left(x,y,z_1\right)e^{-i2\pi\left(xk_x+yk_y\right)}dxdy\,. \tag{3}$$

It can be seen that $s\left(k_x,k_y\right)$ forms a 2D Fourier transform of the spin density $\rho\left(x,y,z_1\right)$. k_x and k_y are the two spatial frequency components. The collected signal we formularized is commonly called *k*-space data. If the *k*-space data is properly collected, we will get $\rho\left(x,y,z_1\right)$ after taking the inverse Fourier transform. This process is the fundamental basis for MRI image reconstruction. Different ways of filling the *k*-space data trajectory correspond to different MR pulse sequences.

The previous discussions are based on the assumption that there is no static field inhomogeneity ΔB. In practice, ΔB, either caused by hardware imperfection or susceptibility differences at air/tissue or bone/tissue interfaces, will cause accumulated phase other than that induced by the frequency-encoding gradient and the phase-encoding gradient. This phase will compromise the spatial encoding achieved by the imaging gradients and will cause problems in image reconstruction. The *k*-space data in the presence of field inhomogeneity will have a form given by

$$s\left(k_x,k_y\right)=A\iint\rho\left(x,y,z_1\right)e^{-i2\pi\left(x\int_0^t G_x(t')dt'+y\int_0^t G_y(t')dt'+\Delta B(x,y,z_1)t\right)}dxdy\,. \tag{4}$$

Here, we assume that the field inhomogeneity ΔB is constant during the collection of the image signal. What we will show later on is that the field inhomogeneity can also be

modeled as a function of time and varies slowly with time, a variation potentially caused by motion and physiological activity.

GE imaging is one of the most important classes of MR imaging sequences. A combination of a RF pulse and a slice-selection gradient G_z excites a slice of interest. A subsequent reversed gradient is applied to refocus the spins within the slice. In this work, we ignore any errors in this refocusing. Suppose the phase-encoding gradient is applied for time τ_p with a strength G_y. Then, a defocusing gradient $-G_x$ is applied for time $t_f/2$ followed by the frequency-encoding gradient G_x, which is applied for time t_f. If we set the echo time TE as the zero time point, then during the application of the frequency-encoding gradient, the phase of spins at location (x, y, z_1) at time t has the form

$$\phi(x, y, z_1, t) = -2\pi\gamma\left(xG_x t + yG_y\tau_p + \Delta B(x, y, z_1)t + \Delta B(x, y, z_1)\mathrm{TE}\right). \qquad (5)$$

Let $k_x = G_x t$ and $k_y = G_y\tau_p$, we can rewrite the *k*-space data as

$$s(k_x, k_y) = A\iint p(\omega(x, y, z_1) - \omega_1)\rho(x, y, z_1)e^{-i2\pi\gamma\left(xk_x + yk_y + \Delta B(x,y,z_1)\left(\frac{k_x}{G_x} + \mathrm{TE}\right)\right)}dxdy, \qquad (6)$$

where we introduce a slice-selection function $p(\omega(x, y, z_1) - \omega_1)$ with

$$\begin{aligned}\omega(x,y,z_1) &= \gamma\left(\mathrm{B_o} + zG_z + \Delta\mathrm{B}(x,y,z)\right)\\ \omega_1 &= \gamma\left(\mathrm{B_o} + z_1 G_z\right)\end{aligned} \tag{7}$$

in which $\mathrm{B_o}$ is the static magnetic field. Simplifying Eqn. (6), we have

$$s(k_x,k_y) = A\iint p\left(\gamma G_z\left(z+\Delta\mathrm{B}(x,y,z_1)/G_z - z_1\right)\right)\rho(x,y,z_1)e^{-i2\pi\left(k_x\left(x+\frac{\Delta\mathrm{B}(x,y,z_1)}{G_x}\right)+k_y y+\Delta\mathrm{B}(x,y,z_1)\times\mathrm{TE}\right)}dxdy\,. \tag{8}$$

We now transform the variables of integration $\mathbf{r}(x,y,z_1)$ as follows, where the primed variables (e.g., x') define positions within a warped image:

$$\begin{aligned}x'(\mathbf{r}) &\equiv x + \Delta\mathrm{B}(\mathbf{r})/G_x\\ y'(\mathbf{r}) &\equiv y\\ z'(\mathbf{r}) &\equiv z + \Delta\mathrm{B}(\mathbf{r})/G_z\end{aligned}\,. \tag{9}$$

Assume that the inverse transformation $\mathbf{r} = \mathrm{T}^{-1}(x',y',z')$ exists, which means that the Jacobian $J(\mathbf{r})$ (*i.e.*, the determinant, $|\partial\mathbf{r}'/\partial\mathbf{r}|$) of the transformation is non-zero. From Eqns. (9), it can be shown that

$$J(\mathbf{r}) = 1 + \frac{1}{G_x}\frac{\partial\Delta\mathrm{B}}{\partial x} + \frac{1}{G_z}\frac{\partial\Delta\mathrm{B}}{\partial z}\,. \tag{10}$$

Therefore $J > 0$, and hence the inverse transformation exists, in regions for which the following relationships hold:

$$\left|\frac{\partial \Delta \mathrm{B}}{\partial x}\right| \ll G_x, \left|\frac{\partial \Delta \mathrm{B}}{\partial z}\right| \ll G_z . \tag{11}$$

Using Eqns. (9) in Eqn. (8) yields

$$\begin{aligned} s\left(k_x, k_y\right) = \; & A \iiint p\left(\gamma G_z\left(z' - z_1\right)\right) \rho(\mathbf{r}) \times \\ & \exp\left(-i\gamma \Delta \mathrm{B}(\mathbf{r}) \times \mathrm{TE}\right) \times \\ & \exp\left(-i\left(k_x x' + k_y y\right)\right) J(\mathbf{r})^{-1} \, d\mathbf{r}', \end{aligned} \tag{12}$$

The reconstructed image intensity at a point $\mathbf{r}_1 \equiv x_1, y_1, z_1$ is produced by taking the inverse Fourier transform $\Im^{-1}$ of the *k*-space data,

$$\begin{aligned} i(\mathbf{r}_1) = \; & \Im^{-1}\left\{s\left(k_x, k_y, z_1\right), x_1, y_1\right\} \\ = \; & C \int p\left(\gamma G_z\left(z' - z_1\right)\right) \times \\ & \rho(\mathbf{r}) \exp\left(-i\gamma \Delta \mathrm{B}(\mathbf{r}) \times \mathrm{TE}\right) J(\mathbf{r})^{-1} \, dz' \end{aligned} \tag{13}$$

If the spin density $\rho(\mathbf{r})$ is assumed to be constant within the slice of interest, we have

$$i(\mathbf{r}_1) = C\rho(\mathbf{r}) \exp\left(-i\phi_0(\mathbf{r})\right) \exp\left(-i\gamma \Delta \mathrm{B}(\mathbf{r}) \times \mathrm{TE}\right) J(\mathbf{r})^{-1}, \tag{14}$$

where $\phi_0(\mathbf{r})$ is the residual phase error caused by imperfect slice excitation. Hence, a GE MR image at position $\mathbf{r}_1$ in the presence of field inhomogeneity has an intensity value proportional to the spin density modified by a Jacobian factor at position $\mathbf{r}$, and the phase is linearly related to $\Delta B(\mathbf{r})$.

3.2. Field mapping based on dual-echo images

According to the above mathematical derivation, the phase of a reconstructed GE image is linearly related to the distortion field ΔB. Image phase can be computed from the imaginary part and real part of a complex image $i(\mathbf{r}_1)$ using

$$\tan^{-1}\left(\text{imag}\left(i(\mathbf{r}_1)\right)/\text{real}\left(i(\mathbf{r}_1)\right)\right). \tag{15}$$

Based on Eqn. (14), the image phase is related to $\Delta B(\mathbf{r})$ by

$$\phi(\mathbf{r}_1) = -\left(\gamma \Delta B(\mathbf{r}) \times TE + \phi_o(\mathbf{r})\right). \tag{16}$$

If the phase error $\phi_o(\mathbf{r})$ is negligible, we have

$$\phi(\mathbf{r}_1) \approx -\gamma \Delta B \times TE\,. \tag{17}$$

The field inhomogeneity information is encoded in the image phase of the reconstructed GE image. Unfortunately, a direct computation of ΔB is difficult because the TE value is typically large and we have

$$\phi(\mathbf{r}_1) = \tan^{-1}\left(\text{imag}\left(i(\mathbf{r}_1)\right)/\text{real}\left(i(\mathbf{r}_1)\right)\right) + 2k\pi, k = 0, \pm 1, \pm 2, \ldots. \quad (18)$$

However, the value of the $\tan^{-1}$ function lies only in the range of $[-\pi, \pi]$, while the true phase change may be well outside that range, as indicated by Eqn. (18). This ambiguity is the well-known "phase wrapping" problem, and because of it a phase map computed via Eqn. (15) can be expected to exhibit severe phase wrapping. Calculation of a field inhomogeneity map from a wrapped phase map will be highly inaccurate. This problem is demonstrated in Figure 4 and Figure 5. In Figure 4, the left image is a true field map. The right image is the field map calculated by means of Eqn. (15). The discontinuity in the right image demonstrates the phase wrapping ambiguity. A profile plot of both images (locations are indicated by red lines in Figure 4) is shown in Figure 5. The disagreement in some areas demonstrates phase wrapping ambiguity.

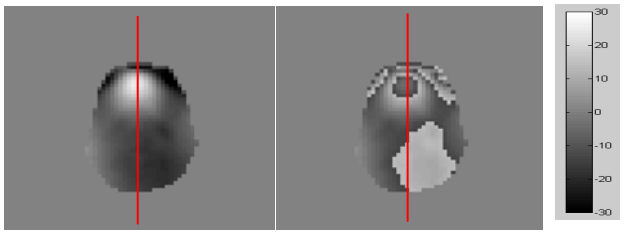

Figure 4. A true field map (left) and the field map calculated from a wrapped phase map (right). Discontinuity in the right image demonstrates phase wrapping ambiguity.

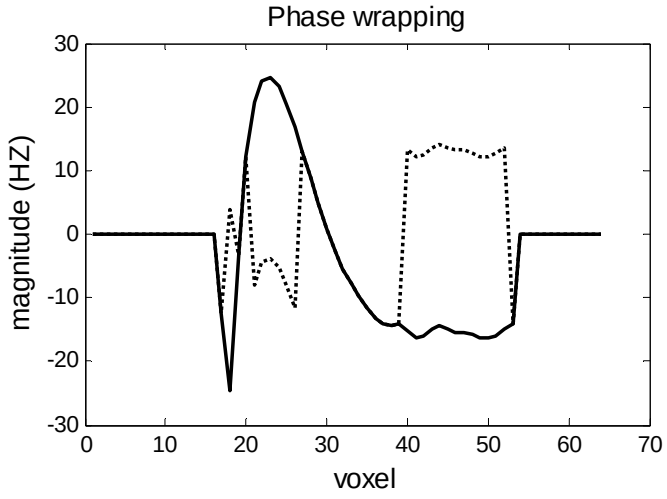

Figure 5. A profile (red lines in Figure 4) plot of the true field map (solid line) and the field map calculated via Eqn. (15) (dotted line). The disagreement in some areas demonstrates phase wrapping ambiguity.

The map of field inhomogeneity, however, can be computed from two or more GE images acquired with differing values of TE [15;36]. According to our derivation, two GE images differing in their echo time by $\Delta\mathrm{TE}$ can be represented by

$$i_{\mathrm{TE}}\left(\mathbf{r}_{\mathrm{l}}\right)=C\rho\left(\mathbf{r}\right)\exp\left(-i\phi_{0}\left(\mathbf{r}\right)\right)\exp\left(-i\gamma\Delta\mathrm{B}\left(\mathbf{r}\right)\times\mathrm{TE}\right)J\left(\mathbf{r}\right)^{-1} \tag{19}$$

and

$$i_{\mathrm{TE}+\Delta\mathrm{TE}}\left(\mathbf{r}_{\mathrm{l}}\right)=C\rho\left(\mathbf{r}\right)\exp\left(-i\phi_{0}\left(\mathbf{r}\right)\right)\exp\left(-i\gamma\Delta\mathrm{B}\left(\mathbf{r}\right)\times\left(\mathrm{TE}+\Delta\mathrm{TE}\right)\right)J\left(\mathbf{r}\right)^{-1}. \tag{20}$$

These two GE images share the same imaging parameters except for echo time and it is assumed that they are scanned closely in time so that the field inhomogeneity remains static. We will call this pair of images "dual-echo" images. If $\Delta\mathrm{TE}$ is chosen to be small enough, a map of field inhomogeneity can be calculated from these two complex images by

$$\Delta\mathrm{B}(\mathbf{r}) = \frac{\mathrm{angle}\left(i_{\mathrm{TE}}(\mathbf{r}_1) / i_{\mathrm{TE}+\Delta\mathrm{TE}}(\mathbf{r}_1)\right)}{\gamma \Delta\mathrm{TE}}. \tag{21}$$

Here, we use "angle" to denote the phase of a complex image, and use / to denote a complex division of two complex images. For traditional GE images, geometric distortion is negligible in most applications because of high bandwidth in this type of pulse sequence. Hence, $\mathbf{r} \approx \mathbf{r}_1$ and $\Delta\mathrm{B}(\mathbf{r}) \approx \Delta\mathrm{B}(\mathbf{r}_1)$ holds. We denote the field map acquired using two traditional GE images as an "undistorted field map" because the field map computed has minimum warping. Because of the image quality of GE images, the computed field map has a high SNR and high resolution and can be utilized to correct the image distortion of EPI. However, the acquisition of a pair of GE images typically takes a couple of minutes of scan time. Motion of human subject during that time is likely, and it will decrease the effectiveness of distortion correction methods relying on this acquisition.

Now we consider a "blipped" GE-EPI sequence in which movement along the k_y (nominal phase-encoding) axis is accomplished by means of G_b gradient pulses and the readout is performed back and forth in the k_x direction while the G_x gradient directs the *k*-space trajectory. Figure 6 shows the pulse sequence and the path through *k*-space. Note

that we have set the echo time as the time origin. Thus, the 90° excitation pulse is at $t = -\mathrm{TE}$.

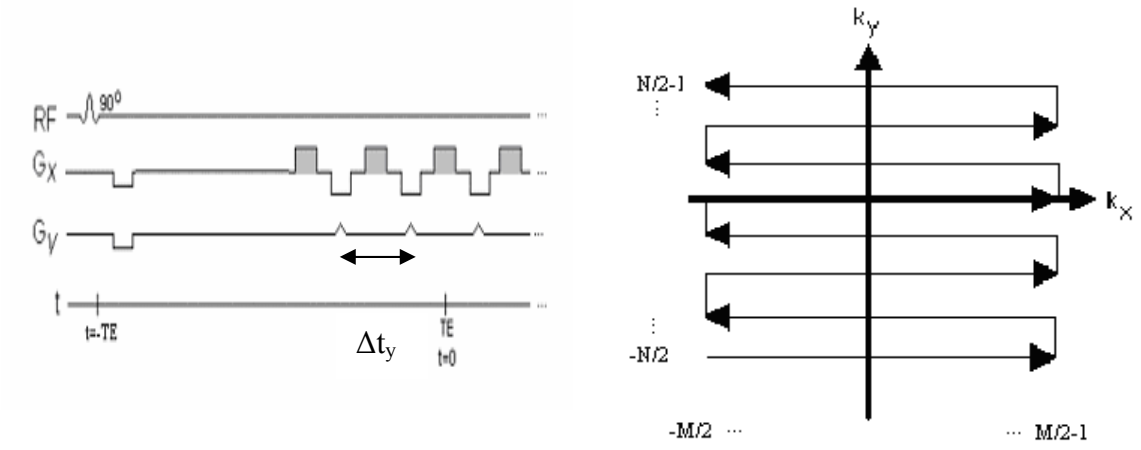

Figure 6. Part of pulse sequence diagram for a blipped GE-EPI sequence. The readout for each k_y line occurs during the shaded G_x. Adjacent *k*-space points in the k_y direction is acquired with a time interval of Δt_y

Similar to our previous derivation, we have the *k*-space representation for a multi-slice GE-EPI sequence as follows:

$$\begin{aligned} s(k_x, k_y, z_1) = \; & A\int p\left(\gamma G_z\left(z + \Delta \mathrm{B}(\mathbf{r})/G_z - z_1\right)\right)\times \\ & \rho(\mathbf{r})\exp\left(-i\gamma\Delta \mathrm{B}(\mathbf{r})\times \mathrm{TE}\right)\times \\ & \exp\left(-i\left(k_x\left(x + \Delta \mathrm{B}(\mathbf{r})/G_x\right) + \right.\right. \\ & \left.\left. k_y\left(y + \Delta \mathrm{B}(\mathbf{r})/G_y\right)\right)\right) d\mathbf{r}, \end{aligned} \tag{22}$$

with each variable having the same meaning as before except G_y. Here we define G_y as the "effective gradient" in the phase-encoding direction defined as

$$G_y \equiv \int_0^{\tau_p} G_{\mathrm{b}}(t)\,dt \Big/ \Delta t_y \tag{23}$$

with τ_p being the interval of time during which the blipped gradient is applied. With a similar variable transformation, $\mathbf{r}' \equiv x', y', z' = \mathrm{T}(x, y, z)$, as before, the following holds for the EPI:

$$\begin{aligned} x'(\mathbf{r}) &\equiv x + \Delta\mathrm{B}(\mathbf{r})/G_x \\ y'(\mathbf{r}) &\equiv y + \Delta\mathrm{B}(\mathbf{r})/G_y \\ z'(\mathbf{r}) &\equiv z + \Delta\mathrm{B}(\mathbf{r})/G_z \end{aligned}. \tag{24}$$

The Jacobian of the variable transformation can be shown to be

$$\begin{aligned} &J(\mathbf{r}) = \\ &1 + \frac{1}{G_x}\frac{\partial \Delta\mathrm{B}}{\partial x} + \frac{1}{G_y}\frac{\partial \Delta\mathrm{B}}{\partial y} + \frac{1}{G_z}\frac{\partial \Delta\mathrm{B}}{\partial z} \end{aligned}. \tag{25}$$

Compared with Eqn. (9) and Eqn. (10), we can see that EPI has image distortion caused by field inhomogeneity in all three directions while GE image has distortion only in the frequency-encoding direction and the slice-selection direction. Another important fact is that

$$G_y \gg G_x \text{ or } G_z. \tag{26}$$

With this fact, the image distortion in EPI is approximately confined to the phase-encoding direction only. The corresponding spatial transformation of the image induced by field inhomogeneity can be rewritten as

$$\begin{aligned} x'(\mathbf{r}) &\equiv x \\ y'(\mathbf{r}) &\equiv y + \Delta\mathrm{B}(\mathbf{r})/G_y \,. \\ z'(\mathbf{r}) &\equiv z \end{aligned} \tag{27}$$

The corresponding Jacobian factor simplifies to

$$J(\mathbf{r}) = 1 + \frac{1}{G_y}\frac{\partial \Delta\mathrm{B}}{\partial y} \,. \tag{28}$$

Based on the above derivation, the reconstructed EPI at $\mathbf{r}_1(x_1, y_1, z_1)$ in the presence of field inhomogeneity is produced by taking the inverse Fourier transform $\Im^{-1}$ of the *k*-space data represented by Eqn. (22),

$$i(\mathbf{r}) = C\rho(\mathbf{r})J(\mathbf{r})^{-1}\exp\left(-i\gamma\Delta\mathrm{B}(\mathbf{r})\times\mathrm{TE}\right) \tag{29}$$

where C is a scaling constant, the difference between $\mathbf{r}_1$ and $\mathbf{r}$ represent the geometric distortion of EPI, and $J(\mathbf{r})$ represents the intensity distortion induced by the geometric transformation of the image. $-\gamma\Delta\mathrm{B}(\mathbf{r})\times\mathrm{TE}$ represents the image phase. Eqn. (29) is guaranteed to have a solution as long as the Jacobian is nonzero. Note that we have

ignored the effects caused by intravoxel dephasing, which could induce more intensity distortion. In this work we focus on correction only of geometric distortion and the component of intensity distortion induced by geometric deformation of the image.

Based on two EPIs with slightly different TEs, a field map can be calculated. The SNR of a standard GE scan is superior to that of a GE-EPI scan, but, because an EPI scan is much faster than a GE scan, the potential for patient motion is reduced during the acquisition. On balance, field-mapping based on dual-echo EPIs is superior to that based on dual-echo GE images.

3.3. Estimation of dynamic distortion fields for a EPI time series

The above field-mapping techniques indeed provide an effective solution to compute the distortion field for the correction of the distortion of a single EPI. However, as we have described, the distortion field induced by the susceptibility differences of air-tissue or bone-tissue varies not only spatially but also temporally because of motion and respiration. A fast imaging application requires acquisition of a hundred or more volumes over a period of three or more minutes, and therefore it would be inappropriate to approximate the dynamic distortion fields for a whole time series with a static distortion field. Because each EPI in a time series is distorted differently, the desired temporal variation is corrupted by changes due to the changes in distortion, termed “temporal noise” in the signal. Estimation of dynamic image distortion for EPI time series can help to reduce the temporal noise in EPI time series. Hence, it is desirable to have a separate distortion field for each time point individually.

As we have seen, the phase of GE images encodes field inhomogeneity information. However, because of phase wrapping ambiguity it is not possible to extract a distortion field from the image phase directly. Intuitively, when the distortion field changes in time, the phase will change accordingly. On the other hand, the phase changes in time encode the temporal variation of the distortion field. If the distortion field changes sufficiently slowly with time, the corresponding temporal phase changes between adjacent volumes in the series will have minimum or correctable phase wrapping. So the variations of the distortion field in time can be computed from the image phase directly. Based on this idea, a separate distortion field for each EPI image can be derived.

Suppose we have two EPIs (i_o and i_1) that are acquired at the beginning of an EPI time series with a difference of $\Delta\mathrm{TE}$ in their echo times. According to Eqn. (29), the phase of the reconstructed images can be written as follows:

$$\phi_o \approx -\gamma \Delta \mathrm{B}_1 \times \left(\mathrm{TE}+\Delta\mathrm{TE}\right) \tag{30}$$

and

$$\phi_1 \approx -\gamma \Delta \mathrm{B}_1 \times \mathrm{TE}\,. \tag{31}$$

Because i_o and i_1 are acquired closely in time, we can assume that they have the same field inhomogeneity $\Delta\mathrm{B}_1$. Consider another EPI which is acquired immediately after the acquisition of i_1 with the same echo time as i_1. We call this image i_2, and, because of

patient motion or respiration it experiences a different distortion field represented by ΔB_2. Its phase can be written as

$$\phi_2 = -\gamma \Delta B_2 \times TE . \tag{32}$$

Although each of the phases ϕ_0, ϕ_1, and ϕ_2 is so large that a direct calculation based on Eqn. (15) will suffer from the angular ambiguity due to phase wrapping, the phase differences between i_o and i_1 and the differences between i_1 and i_2 tend to be small and have minimum phase wrapping. Here minimum phase wrapping means either no phase wrapping or the phase wrapping can easily be corrected. The small size of these differences can be explained by the fact that (a) $\phi_1 - \phi_0 = \gamma \Delta B_1 \times \Delta TE$ is small if ΔTE can be made sufficiently small and (b) $\phi_1 - \phi_2 = \gamma \left(\Delta B_2 - \Delta B_1 \right) \times TE$ is small if the variation of ΔB at a given point in scanner space is sufficiently slow in time. Based on this idea, the distortion fields corresponding to two time points can be calculated with the assistance of one extra EPI i_o. Formulas for inhomogeneity are given as follows:

$$\begin{aligned} \Delta B_1(\mathbf{r}) &= \text{angle}\left(\frac{i_1(\mathbf{r})}{i_0(\mathbf{r})} \right) \Big/ (\gamma \Delta TE) \\ \Delta B_2(\mathbf{r}) &= \Delta B_1(\mathbf{r}) + \text{angle}\left(\frac{i_1(\mathbf{r})}{i_2(\mathbf{r})} \right) \Big/ (\gamma TE) \end{aligned} . \tag{33}$$

Note here that we use $\mathbf{r}$ to represents a position that is fixed with respect to the scanner's coordinate system (i.e., not fixed with respect to the patient's head). Because

the field map is computed from the warped EPI and because the patient's head may move between acquisitions, $\mathbf{r}$ will in general lie at different points in the patient's head at different points in time, and therefore for different values of k, $\Delta B_k(\mathbf{r})$ denotes the inhomogeneity at different points in the head. We will discuss this further later in this chapter.

It is straightforward to alter Eqns. (33) to compute the distortion field for any given time point in terms of the distortion field and the image at the preceding time point as follows:

$$\begin{aligned} \Delta B_1(\mathbf{r}) &= \text{angle}\left(\frac{i_1(\mathbf{r})}{i_0(\mathbf{r})}\right) \Big/ (\gamma \Delta TE) \\ &\ldots \\ \Delta B_k(\mathbf{r}) &= \Delta B_{k-1}(\mathbf{r}) + \text{angle}\left(\frac{i_{k-1}(\mathbf{r})}{i_k(\mathbf{r})}\right) \Big/ (\gamma TE), k = 2,3,\ldots \end{aligned} \quad . \qquad (34)$$

Note that we only need one extra image $i_o(\mathbf{r})$ to perform all the calculation. Hence, the extra scan time for a fast imaging applications requiring a hundred or more acquisitions is almost negligible.

3.4. Regularization of phase maps

Correction of EPIs can be performed with the distortion fields calculated from Eqns. (34), but any estimation error of the distortion fields will propagate to the corrected images. The distortion field we calculate is based on the phase of EPIs, which are notorious noisy. Regularization of the distortion fields has a strong impact on the

corrected images. Regularization is necessary because the temporal variations of the distortion fields tend to be subtle and sensitive to noise.

A low-pass spatial filter provides a simple regularization method for a noisy field map, but the estimation errors in the field map could propagate to other regions by using this approach. A more promising regularization method was recently proposed by Fessler *et al.* [80]. A regularized field map is estimated from two complex GE images based on maximum likelihood (ML). We extend their regularization method to estimate dynamic distortion fields of EPI time series using our phase-map method. In the following, we will briefly describe their approach followed by our modifications.

Suppose two complex GE images with a difference of ΔTE in their echo times are represented by y and z. Then each reconstructed voxel j ($j = 1:N$ and N is the number of voxels) has a form as follows:

$$\begin{aligned} y_j &= f_j + \varepsilon_j \\ z_j &= f_j e^{ix_j} + \eta_j \end{aligned}, \tag{35}$$

where f_j denotes a complex voxel, $x_j = -\gamma \Delta \mathrm{B}_j \times \Delta \mathrm{TE}$, ε_j and η_j denote complex noise that is assumed to have a Gaussian distribution with zero-mean and σ standard deviation. In the equation, y and z are the observed data (complex intensities after image reconstruction) and f and x are unknown variables. A solution based on ML can be carried out as follows. The joint log-likelihood for the estimation of f and x given y and z is

$$\log p(y; f) + \log p(z; f, x) = \frac{-1}{2\sigma^2} \sum_{j=1}^{N} \left| y_j - f_j \right|^2 + \left| z_j - f_j e^{ix_j} \right|^2 . \quad (36)$$

After simplification, the ML cost function for estimation of x is given as

$$\Psi(x) = \sum_{j=1}^{N} \left| y_j z_j \right| \left[1 - \cos\left(\text{angle}\left(z_j \right) - \text{angle}\left(y_j \right) - x_j \right) \right]. \quad (37)$$

In the absence of noise, the cost function is minimized when $x_j = \text{angle}\left(z_j \right) - \text{angle}\left(y_j \right)$ ($\left| \ \right|$ denotes the computation of a magnitude from a complex image), which is exactly the same as the traditional dual-echo field mapping defined in Eqn. (21).

In order to suppress noise effect, a regularization term can be incorporated into the cost function (37) based on the *a priori* knowledge that the field map tends to be smooth in space. Hence, the penalized ML cost function to estimate the distortion field from two complex GE images can be constructed as follows:

$$\Psi(\Delta \text{B}) = \sum_{j=1}^{N} \left| y_j z_j \right| \left[1 - \cos\left(\text{angle}\left(z_j \right) - \text{angle}\left(y_j \right) - x_j \left(\Delta \text{B}_j \right) \right) \right] + \beta R(\Delta \text{B}), \quad (38)$$

where β is the coefficient to control the smoothness of the estimated field and $R(x)$ is a spatial roughness penalty term. Following Fessler, we base the penalty on the differences in values of the distortion field between horizontal and vertical neighboring voxels. The regularized distortion field can then be estimated by iteratively solving Eqn. (38).

We aim to extend Fessler's approach for field-map regularization and apply it to our phase-map method. A direct extension, however, is complicated by the fact that, image i_{k-1} and i_k may not share the same image magnitude at each reconstructed voxel j because the patient's head may move or be warped differently between acquisitions and voxel j will in general lie at different points within the patient's head at different points in time, whereas the assumption in Fessler's application is that both images have magnitude $\left|f_j\right|$. In order to accommodate differences in intensity, we only consider the noise in image phase. While the complex image is corrupted by Gaussian noise, the noise distribution in image phase could be complicated. We make the approximation that the image phase is corrupted by Gaussian noise. This assumption does not agree with the assumption of additive complex noise made by Fessler, which is based on the observed noise patterns in MR signal acquisition, but we make it in order to simplify this problem. A more complicated noise model for the image phase still allows us to apply a regularization approach (see future work described in Chapter VI). The phase differences between images i_0 and i_1 and between images i_{k-1} and i_k can be represented by

$$\begin{aligned}
&\Delta\phi_1(\mathbf{r}) = \phi_0(\mathbf{r}) - \phi_1(\mathbf{r}) = \gamma \Delta \mathrm{B}_1(\mathbf{r}) \times \Delta\mathrm{TE} + \eta(\mathbf{r}) \\
&\Delta\phi_k(\mathbf{r}) = \phi_k(\mathbf{r}) - \phi_{k-1}(\mathbf{r}) = \gamma\left(\Delta \mathrm{B}_k(\mathbf{r}) - \Delta \mathrm{B}_{k\text{-}1}(\mathbf{r})\right) \times \mathrm{TE} + \varepsilon(\mathbf{r}), \qquad (39) \\
&k = 2, 3, \ldots.
\end{aligned}$$

where $\eta(\mathbf{r})$ and $\varepsilon(\mathbf{r})$ denotes Gaussian noise at location $\mathbf{r}$. In Eqns. (39), $\Delta\phi_k(\mathbf{r})(k = 1, \ldots)$ is the observed data, ΔTE and TE are known parameters, and

$\Delta \mathrm{B}_{\mathrm{k}}(\mathbf{r})$ are the unknowns. For each image we define a ML function as the weighted sum of the squared difference between the observed phase differences $\Delta\phi$ and the phase that can be modeled as function of $\Delta \mathrm{B}$. For image i_1 the function can be written as

$$\psi_1 = \sum_{j=1}^{N} w_1(\mathbf{r})\left(\Delta\phi_1 - f\left(\Delta \mathrm{B}_1, \Delta \mathrm{TE}\right)\right)^2, \tag{40}$$

where $f(x, y) = \gamma xy$. The weighting function, $w_1(\mathbf{r})$, is defined as the product of the image intensity of the two images from which the phase differences are computed:

$$w_1(\mathbf{r}) = \left|i_0(\mathbf{r}) i_1(\mathbf{r})\right|. \tag{41}$$

Similarly, a function ψ_k to estimate the distortion field of image i_k is defined as

$$\psi_k = \sum_{j=1}^{M} w_k(\mathbf{r})\left(\Delta\phi_k - f\left(\Delta \mathrm{B}_k - \Delta \mathrm{B}_{k-1}, \mathrm{TE}\right)\right)^2, \tag{42}$$

and $w_k(\mathbf{r}) = \left|i_{k-1}(\mathbf{r}) i_k(\mathbf{r})\right|$. As we know, the phase differences between adjacent image volumes can be written as

$$\begin{aligned}\Delta\phi_1 &= \text{angle}\left(\frac{i_1(\mathbf{r})}{i_0(\mathbf{r})}\right)\\ \Delta\phi_k &= \text{angle}\left(\frac{i_{k-1}(\mathbf{r})}{i_k(\mathbf{r})}\right)\end{aligned}. \tag{43}$$

Following Fessler, *a priori* knowledge about the distortion field can be incorporated into Eqn. (40) and Eqn. (42) in the form of a penalty function. The resulting penalized ML functions to compute the distortion fields for multiple time points can be written as

$$\begin{aligned}\Psi(\Delta\mathrm{B}_1) &= \sum_{j=1}^{M}|i_o i_1|\left(\text{angle}\left(\frac{i_1(\mathbf{r})}{i_0(\mathbf{r})}\right)-f\left(\Delta\mathrm{B}_{1,\mathrm{j}},\Delta\mathrm{TE}\right)\right)^2+\beta R(\Delta\mathrm{B}_1)\\ \Psi(\Delta\mathrm{B}_2) &= \sum_{j=1}^{M}|i_1 i_2|\left(\text{angle}\left(\frac{i_1(\mathbf{r})}{i_2(\mathbf{r})}\right)-f\left(\Delta\mathrm{B}_{2,j}-\Delta\mathrm{B}_{1,j},\mathrm{TE}\right)\right)^2+\beta R(\Delta\mathrm{B}_2)\\ &\cdots\\ \Psi(\Delta\mathrm{B}_k) &= \sum_{j=1}^{M}|i_{k-1} i_k|\left(\text{angle}\left(\frac{i_{k-1}(\mathbf{r})}{i_k(\mathbf{r})}\right)-f\left(\Delta\mathrm{B}_{k,j}-\Delta\mathrm{B}_{k-1,j},\mathrm{TE}\right)\right)^2+\beta R(\Delta\mathrm{B}_{\mathrm{k}})\end{aligned}, \tag{44}$$

where

$$\begin{aligned}R(\Delta\mathrm{B}) = &\sum_{n=1}^{N-1}\sum_{m=1}^{M-1}\sum_{k=1}^{K-1}\varphi\left(\Delta\mathrm{B}[n,m,k]-\Delta\mathrm{B}[n-1,m,k]\right)+\\ &\sum_{n=1}^{N-1}\sum_{m=1}^{M-1}\sum_{k=1}^{K-1}\varphi\left(\Delta\mathrm{B}[n,m,k]-\Delta\mathrm{B}[n,m-1,k]\right)\\ &+\sum_{n=1}^{N-1}\sum_{m=1}^{M-1}\sum_{k=1}^{K-1}\varphi\left(\Delta\mathrm{B}[n,m,k]-\Delta\mathrm{B}[n,m,k-1]\right)\end{aligned}. \tag{45}$$

with N, M, and K being the number of voxels of the field map volume and $\varphi(t)$ being a differentiable function. Again, following Fessler, we choose $\varphi(t) = t^2 / 2$.

Eqns. (44) represent a nonlinear optimization problem that can be solved iteratively using Newton's approach. The iterative solution is given by Eqn. (46), where l is the iteration number. Regularized distortion fields can be then estimated.

$$\Delta \mathrm{B}^{(l+1)} = \Delta \mathrm{B}^{(l)} - \nabla \Psi\left(\Delta \mathrm{B}^{(l)}\right) \Big/ \nabla^2 \Psi\left(\Delta \mathrm{B}^{(l)}\right) \tag{46}$$

Essentially, it can be seen from Eqns. (44) that our estimation method tends to extrapolate the estimated fields in areas where the intensity is low ($\left|i_{k-1} i_k\right|$ is small) while relying on local phase information where the intensity is high. The trade-off is controlled by the coefficient β. In practice, this regularization method is quite efficient. Several iterations are sufficient to generate estimated fields with proper regularization. One drawback of the regularization approach is that the coefficient β has to be chosen manually. A high β value is preferred when the image has a low signal-to-noise ratio. The spatial resolution of the estimated field map, however, is reduced with a high value of β. The effect of β on the local frequency response of the regularization estimator is discussed in [81].

3.5. Correction of an EPI when the distortion field is known

By taking the absolute value of both sides of Eqn. (29) and letting $i_c(\mathbf{r}) = C\rho(\mathbf{r})$ we find that $i_c(\mathbf{r}) = i(\mathbf{r}_1)J(\mathbf{r})$. Using this relation and Eqns. (27) and Eqn. (28), we can perform the correction of an EPI when the distortion field $\Delta \mathrm{B}(\mathrm{r})$ is given as follows:

$$\begin{aligned} & i_c(\mathbf{r}) = i(\mathbf{r}_1)J(\mathbf{r}) \\ & y_1 = y + \Delta \mathrm{B}(y)/G_y \\ & x_1 = x \\ & J(\mathbf{r}) = 1 + \frac{\partial \Delta \mathrm{B}(y)}{\partial y} \Big/ G_y . \end{aligned} \quad . \tag{47}$$

We call this calculation a "backward" correction when the distortion field is provided in "undistorted" space. The field-mapping approach based on standard GE images generates a field map that lies in undistorted space. The backward correction is applicable in this case. However, when we estimate the distortion field from EPIs, because the EPIs themselves are warped, the estimated field lies in "distorted" space. If the distorted image and the undistorted image have one-to-one spatial correspondence, the following relation holds:

$$\begin{aligned} & i_c(\mathbf{r}) = i(\mathbf{r}_1)J(\mathbf{r}) \\ & y_1 - \Delta \mathrm{B}(y_1)/G_y = y \\ & x_1 = x \\ & J(\mathbf{r}) = \frac{dy_1}{dy} = 1 \Big/ \frac{dy}{dy_1} = 1 \Big/ \left(1 - \frac{\partial \Delta \mathrm{B}(y_1)}{\partial y_1} \Big/ G_y \right) \end{aligned} \quad . \tag{48}$$

A "forward" correction can be used to correct the distorted EPI. In fact, the distortion field can be converted from distorted space to undistorted space or vice versa according to the following relation:

$$\begin{aligned} \mathbf{r}_1 &= \mathbf{r} + \Delta \mathrm{B}(\mathbf{r}) \\ \mathbf{r}_1 - \Delta \mathrm{B}(\mathbf{r}_1) &= \mathbf{r} \end{aligned}, \tag{49}$$

where $\mathbf{r}_1$ is a warped position of $\mathbf{r}$.

This is an important fact that we need to keep in mind because a correction method must account for the space in which the distortion field lies. To see the difference between a distortion field in distorted space and one in undistorted space, a comparison is made in Figure 7 and Figure 8. Figure 7 denotes (a) a field map in undistorted space, (b) the corresponding field map in distorted space, and (c) their difference. The difference is caused by the geometric distortion of the EPIs used to calculate the field. (b) contains the field as calculated directly from two EPIs, while (a) is the result of correcting (b) for the geometric distortion in the EPI. A profile plot along one vertical line in both field maps (positions are marked as red lines in Figure 7) is shown in Figure 8, where a difference is noticeable. The distortion field can be converted from either space to the other, but the corresponding distortion correction method will be slightly different as Eqn. (47) and Eqn. (48) show. We will be using this fact in Chapter IV.

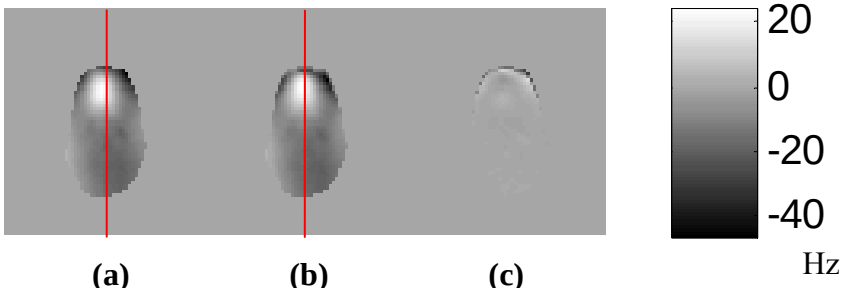

Figure 7. (a) an undistorted field map, (b) a distorted field map, and (c) their difference. We can see the difference when we get a field map in undistorted space and distorted space.

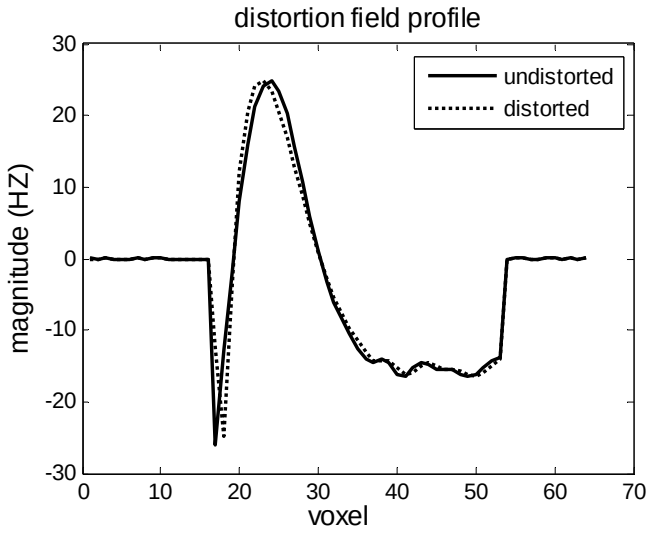

Figure 8. A profile plot (indicated by red lines in Figure 7) of a field map in undistorted space (solid line) and distorted space (dashed line). Slight differences are noticeable because of geometric distortion of EPI.

3.6. Conclusion

Correction of EPIs is typically performed using the traditional field-map method, in which the distortion field is computed from the phase differences of two GE images. However, the field-map method cannot encode the temporal variations of distortion fields

induced by respiration and motion in EPI time series. Each EPI in a time series could potentially experience different image distortion, which makes the field-map method invalid.

We have developed a method to estimate the dynamic distortion fields in EPI time series via image phase. The temporal variation of the image phase encodes the variation of the distortion field, which provides useful information to correct the dynamic image distortion. The phase information of the EPIs, in conjunction with one extra EPI, helps to compute a separate distortion field for each EPI in a time series. A regularization term based on maximum likelihood is incorporated in the estimation of dynamic distortion fields to suppress the effect of noise. Once this distortion field is determined, each EPI can be corrected accordingly. A validation of this method is presented in Chapter V.

CHAPTER IV

ESTIMATION OF DYNAMIC DISTORTION FIELDS VIA BOTH PHASE AND INTENSITY

In last chapter, we introduced a phase-map method to estimate dynamic distortion fields in EPI time series using image phase information. However, there are two potential issues with the phase-map method. First, when there is sufficient movement during the time series, the phase variation for some physical locations may not be available because they have moved into the background area of the previous image. The variations of distortion fields cannot be determined in these regions because of lack of phase information. Second, the calculation of dynamic distortion fields is based on assumption that the distortion fields vary sufficiently slowly with time. When the variation of the distortion fields between adjacent volumes is large, the induced phase differences could suffer from phase wrapping. Integration of image intensity information via image registration has the potential to mitigate both these issues.

Rigid-body registration based on image intensity is a standard method for motion compensation of EPI time series. Correction of a single EPI image using non-rigid registration methods has also been intensively studied. However, the potential for using both rigid and non-rigid registration to estimate the dynamic distortion fields in EPI time series has not yet been fully explored. In this chapter, we study the feasibility of employing image registration to perform motion compensation and distortion correction of EPI time series. A mathematical framework that characterizes the effect of motion-distortion in EPI time series is described. The limitations of using non-rigid registration

to correct the EPI image series are analyzed. To overcome these limitations we propose to incorporate the phase information in the standard registration framework for the estimation of the dynamic distortion fields in EPI time series. Our phase-map method from Chapter III is in the present chapter used as an adjunct to the registration method by applying it to the original EPI series to obtain a more accurate first approximation to motion compensation via rigid-body registration. We then develop a phase-gradient term from the image phase map. This term is incorporated in standard non-rigid registration based on the minimization of a sum of cost functions. The phase gradients are time-dependent and approximately proportional to the gradients of the distortion field of the EPI, and when used as a cost function help to impose a spatial constraint on the estimated distortion field. In summary, in this chapter, a strategy is suggested for the correction of dynamic image distortion in EPI time series using a method of registration that incorporates both phase information and intensity information.

4.1. Motion compensation in EPI series

In EPI time series, the majority of the erroneous variation of image intensity is attributable to the rigid motion of the imaging subject [82] and respiration-induced Bo fluctuations [75]. An image realignment based on intra-subject rigid-registration is available in most packages that are designed for data analysis of MR series imaging. To perform motion compensation, a "template" image (usually the first EPI) is chosen as a target image. All other EPIs, termed the "source" images are registered to the template image. Since all EPIs in a time series share the same resolution, modality, and intensity, the measure of difference between images used as a cost function for image registration is

typically the sum of the squared differences (SSD) in intensity. Both rotation and translation parameters are estimated by minimizing the cost function to make the transformed source images more similar to the template image.

We let the source image be I_S and the template image be I_T. Suppose the rigid transformation from I_S to I_T is unknown and represented by six parameters including rotation and translation $\vec{q} = [q_1, ..., q_6]$. The homogeneous matrix of the corresponding transformation can be represented by

$$T = \begin{bmatrix} \cos(q_5)\cos(q_6) & -\cos(q_4)\sin(q_6)+\sin(q_4)\sin(q_5)\cos(q_6) & \sin(q_4)\sin(q_6)+\cos(q_4)\sin(q_5)\cos(q_6) & q_1 \\ \cos(q_5)\sin(q_6) & \cos(q_4)\cos(q_6)+\sin(q_4)\sin(q_5)\sin(q_6) & -\sin(q_4)\cos(q_6)+\cos(q_4)\sin(q_5)\sin(q_6) & q_2 \\ -\sin(q_5) & \sin(q_4)\cos(q_5) & \cos(q_4)\cos(q_5) & q_3 \\ 0 & 0 & 0 & 1 \end{bmatrix}. \quad (50)$$

Then the sum of the squared differences between the transformed source image and the template image is written as

$$\psi_{\text{int}} = \left\| T(\vec{q}) I_S - I_T \right\|^2, \quad (51)$$

where the subscript "int" means "intensity" and signifies that the cost is based entirely on the intensity at each point in the two images. In this equation, we use $\| \ \|^2$ to denote the sum of the squared differences of corresponding voxels between I_S and I_T. If the source image and the template image differ only by a rigid-body transformation, the cost function Eqn. (51) is decreased when the estimated parameters $\vec{q}$ approach the true

transformation parameters $\vec{q}_0$. Hence, motion compensation in EPI time series is essentially a nonlinear optimization process in which a measure of difference in intensity patterns is minimized. The optimization process is formularized as

$$\arg\min_{\vec{q}} \psi \,. \tag{52}$$

In the above method for motion compensation, the source EPI and the template EPI are assumed to differ only by a rigid transformation. However, it is well known that EPI is distorted, as described in Chapter III. Moreover, each EPI can experience a different image distortion from others in the series. In previous work, we have shown that when the source EPI and template EPI experience different image distortion, motion compensation using Eqn. (52) can be biased [83]. It is more appropriate to correct the images before motion compensation is performed. There are three scenarios by which the motion compensation can be performed on an EPI series. The first one is to perform rigid-body motion compensation directly on the EPI series. In this case, the effect of image distortion is totally ignored. We denote the estimated transformation from the source image to the template image in this scenario as T . In the second scenario, the template EPI and each source EPI are corrected using the same distortion field. It represents the case in which only a static distortion field is available. We denote the estimated transformation in this case as T_{fld} . In the third scenario, the template EPI and each source EPI are corrected with a separate distortion field. As we have discussed, the dynamic distortion fields are typically not available. To perform a separate distortion correction for the source EPI and the target EPI, we will utilize the phase-map method

that we introduced in Chapter III. Each EPI is corrected with an estimated distortion field based on our phase-map method. The motion compensation is then performed on the corrected EPI. We denote the estimated transformation matrix using this method as T_{pha}.

4.2. Estimation of dynamic distortion fields using non-rigid registration

Non-rigid registration methods have been employed to correct the image distortion of EPI in which a distorted EPI is warped to a template image. There are mainly two applications of using non-rigid registration in correction of EPI. The first one is for functional localization in the human brain. In this application, the image distortion of EPI needs to be corrected in order to map the activation regions to anatomic regions correctly. A typical template image for registration is an anatomical image (e.g a standard GE image). The distorted EPIs are warped to the anatomical image. The similarity measure is typically based on mutual information because the EPI and the anatomical image have different contrast patterns. Since the distortion of EPI is confined by physics constraints, many groups have developed non-rigid methods for distortion correction by imposing specific constraints on the estimation of deformation fields. For example, Studholme *et al.* [77] suggest using a unidirectional constraint and employing the Jacobian factor of the transformation to estimate the distortion field using a non-rigid registration method. Li *et al.* [84] account for the signal loss of EPI when registering the EPI to an anatomical image and further propose to use a scheme with spatially varying scale for modeling the distortion field based on *a priori* knowledge.

There is another application of non-rigid registration in correction of EPI. In this application the EPI is corrected to reduce the erroneous variation of image intensity in an

EPI time series. The purpose of this application is to reduce the spurious activations or temporal variation induced by dynamic distortion fields or motion-distortion. The pioneering wok regarding the effect of motion-distortion has been laid out by Andersson *et al.* [16] in which a mathematical model was described to estimate motion-dependent distortion fields by using a non-rigid registration method. In this application, the direct application of non-rigid registration tends to be more difficult because of the motion confound. An inappropriate warping of the EPI could generate false distortion fields. Standard registration methods have to be altered before they can be applied to remove the motion-related image distortion in EPI series. This will be the focus of the work we present in this chapter.

As for the motion compensation method, a template image ought to be chosen to perform a non-rigid registration. Typically, a template image would be the first EPI in an image series. It is important to correct the template image before another EPI is warped to this template. We use ΔB_S and ΔB_T to represent the distortion fields for the source image and the template image. The corrected template image is represented by

$$f\left(I_T, \Delta B_T\right). \tag{53}$$

where f represents the correction function defined in Eqns. (48). After the corrected template image $f\left(I_T, \Delta B_T\right)$ has been calculated, a standard rigid-body registration method can be employed to first realign the source EPI with the corrected template image to get an estimated rigid transformation T. Then the rigidly-transformed source EPI is corrected by warping it to match the corrected template EPI.

Note that the distortion in EPI is confined to the phase-encoding direction, which is known and is typically either the vertical or horizontal direction of the EPI. However, if the source EPI is rotated by T when it is registered to the template image, then its distortion direction is rotated as well. Rotation is almost always present, and thus, the image distortion of the transformed source EPI will almost always, contain components in all three directions—phase-encoding, readout, and slice-selection. To avoid that complication, a better strategy is to transform the corrected template EPI to the source EPI with the inverse transformation T^{-1}. Then, the distorted EPI can be warped to the corrected and rigidly-transformed template EPI. This way, we should be able to estimate the distortion field ΔB_S properly by confining the distortion to be unidirectional, as in all other distortion correction methods based on image registration [77]. The cost function that contains the distorted EPI and the transformed template EPI is given as follows:

$$\psi = \left\| f\left(I_S, \Delta B_S\right) - T^{-1}\left(\vec{q}\right) f\left(I_T, \Delta B_T\right) \right\|^2 . \tag{54}$$

The distortion field ΔB_S is estimated by solving the following optimization problem:

$$\arg\min_{\Delta B_S} \psi . \tag{55}$$

. As we can see from this derivation, the accuracy of the rigid realignment T is critical to estimate ΔB_S accurately based on subsequent non-rigid registration. Unfortunately, finding an accurate T depends on knowledge of ΔB_S ! As a way out of

this loop, we note that, according to our theory in Chapter III, an estimation ΔB_{S0} of the distortion field ΔB_S can be calculated by using our phase-map method. ΔB_{S0} could potentially suffer from isolated phase wrapping or inaccurate estimation near the edges of foreground image—the two issues cited at the beginning of this chapter. However, because T is a rigid registration, which has only six degrees of freedom ($\vec{q}$), these local errors should have only a small effect on it, and thus we can expect that a T based on a I_S that has been corrected by using ΔB_{S0} is likely to be more accurate than one based on the original image. In other words, we can use the T_{pha} in Eqn. (54) rather than T or T_{fld} (both defined in previous section). With this in mind, we could rewrite Eqn. (54) as follows:

$$\psi = \left\| f\left(I_S, \Delta B_S\right) - T_{pha}^{-1}\left(\vec{q}, \Delta B_{S0}\right) f\left(I_T, \Delta B_T\right) \right\|^2 . \tag{56}$$

By minimizing the function defined in Eqn. (56), we should be able to estimate the dynamic distortion field ΔB_S more accurately. We will verify this hypothesis in Chapter V. The approximation ΔB_{S0} can also be employed as an initial estimation of ΔB_S when solving Eqn. (56), as suggested in [50], dramatically reducing the convergence time of the optimization.

The distortion field in the traditional field-map method or our phase-map method is represented voxel by voxel. In non-rigid registration, a non-linear function is typically used to represent the estimated distortion field to reduce the degrees of freedom and increase the optimization efficiency. The distortion field is typically modeled as a

combination of basis functions such as B-spline [85], radial basis function [86], or discrete cosine function [16]. This way, the distortion field is uniquely determined by the corresponding coefficients of the basis functions rather than being explicitly specified for each individual voxel. The number of coefficients may be chosen to be much smaller than the number of voxels, thus simplifying greatly the minimization problem. In our work, we have tested both the Cubic B-spline and the radial basis function to model the distortion field. We found no substantial difference between them in our application. We employed the Cubic B-spline to model the distortion field because of its nice properties. The first derivative and the second derivative of Cubic B-spline with respect to the spatial coordinates are also smooth functions and can be calculated easily. Moreover, the B-spline is locally supported, and thus it is more efficient to perform the optimization of distortion field modeled with B-spline than with other splines such as thin-plate spline.

When multiple 1-D B-spline functions are placed evenly on some control points with a spacing of 1, four pieces of polynomial functions lie in the range of [0, 1]. These four pieces of functions are represented as follows:

$$\begin{aligned} B_0(u) &= (1-u)^3/6 \\ B_1(u) &= \left(3u^3-6u^2+4\right)/6 \\ B_2(u) &= \left(-3u^3+3u^2+3u+1\right)/6. \\ B_3(u) &= u^3/6 \\ 0 &\le u \le 1 \end{aligned} \tag{57}$$

Figure 9 (a) shows these four pieces of functions. The B-spline basis function at each control point then consists of four segments. Figure 9 (b) shows a basis function $\phi\left(\mathrm{r}\text{-}\mathrm{r}_j\right)$

locating at control point r_j (2 in this example). The transition from solid line to dotted line shows the transition from one piece of the spline to the next. .

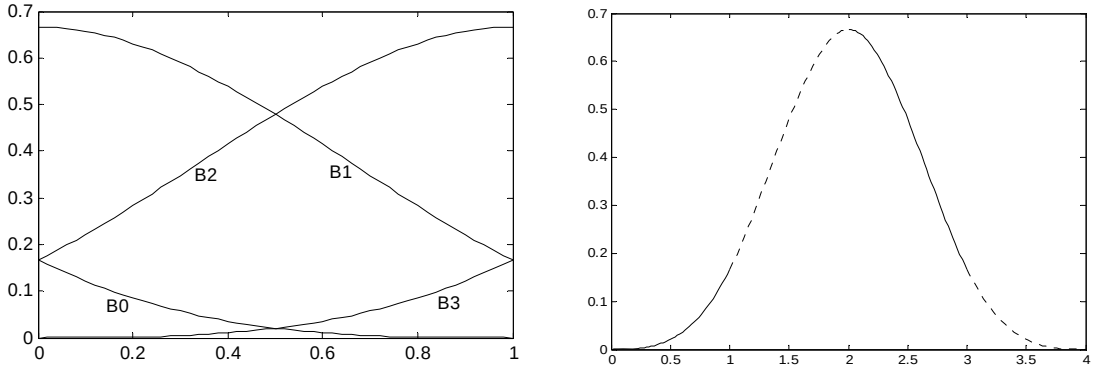

(a) (b)

Figure 9. Cubic B-spline basis function. It consists of four pieces of polynomial functions. (a) The four pieces, B0, B1, B2, B3, as functions of u. (b) $\phi(\mathrm{r}-2)$ formed from B3, B2, B1, B0 (solid, dashed, solid, dashed) shifted right by 0, 1, 2, and 3 units, respectively.

The unknown distortion field can be represented as a linear combination of the basis functions uniformly distributed over the image as follows:

$$\Delta \mathrm{B}(\mathrm{r}) = \sum_{j=1}^{M} c_j \phi(\mathrm{r}\text{-}\mathrm{r}_j), \tag{58}$$

where M is the number of control points on the image and c_j is the corresponding coefficient. Figure 10 shows, as an example, a fitting of a 1D distortion field (dotted line)

with a combination of B-spline basis functions (solid lines). The basis functions are evenly distributed in the image space (horizontal axis). The extension from a 1D B-spline to two dimensions is straightforward:

$$\Delta \mathrm{B}(x, y) = \sum_{i,j} c_{ij} \phi(x - x_i) \phi(y - y_j) \tag{59}$$

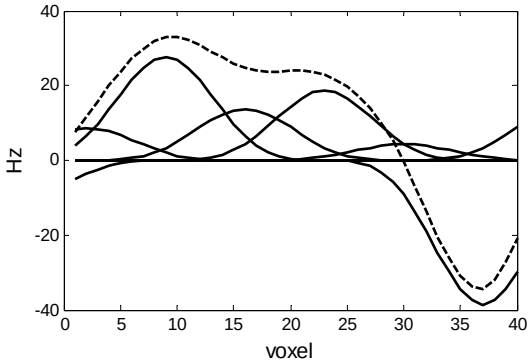

Figure 10. Fitting of 1D distortion field by Cubic B-spline. The dotted line is the fitted distortion field and the solid lines represent the basis functions.

4.3. Limitations of non-rigid registration for estimation of a distortion field.

According to Eqn. (56), the estimation of a distortion field based on non-rigid registration is equivalent to solving a nonlinear optimization problem, in which unknown parameters are estimated. The number of degrees of freedom is equal to the number of control points used to model the distortion field. The cost function is defined as the sum of the squared differences (SSD) between a distorted EPI and a corrected and rigidly-transformed template EPI. To model the distortion field with sufficient accuracy, it is required to place sufficient control points on an image. The number of control points is

determined by their spacing. If, for example, we place B-spline basis functions on every third voxel of in the horizontal and vertical direction of an EPI with a resolution of 64x64, there would be 22x22 unknown parameters to optimize. When the similarity measure is defined as SSD, infinite solutions to the distortion field exist to make it small. An optimization with this many degrees of freedoms is prone to a suboptimal local minimum. Wahba [87] was among the earliest to suggest incorporating a regularization term into a cost function to estimate unknown parameters based on observed data A regularization term that is commonly used is to penalize the second derivative of the estimated field with respect to space to make the estimated field smooth. This regularization represents the so called "bending energy" [85;87;88] of a 2D distortion field, which is defined, in analogy to the energy in the stretching of an elastic medium, as follows:

$$\psi_{\text{smooth}}\left(\Delta \mathrm{B_S}(\mathrm{r})\right) = \left\| \frac{\partial^2 \Delta \mathrm{B_S}}{\partial x^2} \right\|^2 + 2\left\| \frac{\partial^2 \Delta \mathrm{B_S}}{\partial x \partial y} \right\|^2 + \left\| \frac{\partial^2 \Delta \mathrm{B_S}}{\partial y^2} \right\|^2 . \tag{60}$$

Even with this regularization term, a non-rigid registration could still produce a distortion field that is not accurate. As we discussed in Section 4.2, numerous methods have been developed to enforce specific constraints on the estimation of the distortion field in non-rigid registration. However, those constraints are not closely related to the estimated distortion field. The optimization process in these non-rigid registration methods still relies entirely on the intensity information.

4.4. Computation of gradients of a distortion field

According to Eqns (27) to (29), the information about the distortion field of each EPI is encoded in the image phase. However, the distortion field cannot be extracted directly from the wrapped phase. Fortunately, as we discussed before, the changes of phase reflect the changes of the distortion field and vice versa. Because the distortion field in an MR image tends to be spatially smooth, the phase variations in space are expected to be small. In other words, the phase differences between neighboring voxels in the phase image are sufficiently small to have only correctable phase wrapping. This fact can be formularized as follows:

$$\begin{aligned} \text{angle}\left(I^*\left(x_j\right)/I^*\left(x_{j\text{-}1}\right)\right) &\approx \gamma \frac{\partial \Delta \text{B}(\text{r})}{\partial x} v_x \text{TE} \in (-\pi, \pi) \\ \text{angle}\left(I^*\left(y_j\right)/I^*\left(y_{j\text{-}1}\right)\right) &\approx \gamma \frac{\partial \Delta \text{B}(\text{r})}{\partial y} v_y \text{TE} \in (-\pi, \pi) \end{aligned}, \qquad (61)$$

Here we use I^* to denote a complex image in order to clearly distinguish it from a magnitude image, alternatively called an "intensity" image. The subscript j is the voxel index, and v_x, v_y are the voxel dimensions. It can be shown that the left side of Eqn. (61) suffers from minimum phase wrapping provided the magnitude of the angular difference between neighboring voxels in the complex image is less than π. In Figure 11, we show why. Suppose the complex vector $I^*\left(x_j\right)$ lies in the first quadrant and the complex vector $I^*\left(x_{j-1}\right)$ lies in the fourth quadrant and the true phase difference is the angle α_1 as shown. Then, the "angle" function in Eqn (61) will give the correct phase difference.

Now suppose instead that $I^*\left(x_{j-1}\right)$ lies in the third quadrant and the true phase difference from $I^*\left(x_j\right)$ is the angle α_2. In this case, angle function will give the wrong answer, because it always chooses the smallest possible angular difference—in this case β, which is equal to $\alpha_2 - 2\pi$. There is an infinity of possible angles in each of these cases because additions of any integral multiple of 2π are possible as well. In order to produce an unambiguous result, the calculation performed by the angle function must be limited to a range of width 2π. Since angles of small absolute value are to be expected, the optimum range is $(-\pi, \pi)$. Thus, Eq. (61) gives the correct answer if the angular difference lies in this range so the errors of this calculation are minimized when the phase differences between neighboring voxels in the phase image are sufficiently small.

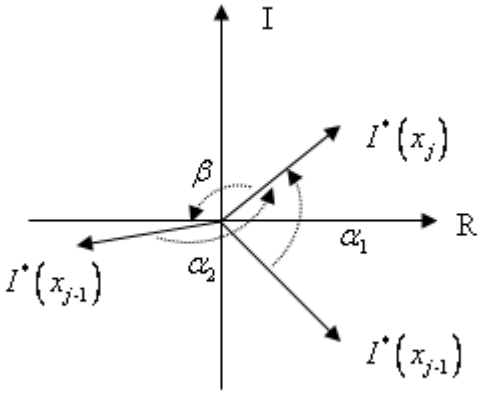

Figure 11. A complex plane demonstrating the validity of our phase-gradient calculation. R refers to the real component; I refers to the imaginary component. See text for explanation.

Based on the above analysis, we can compute the approximate gradients of the distortion field $\partial\Delta\mathrm{B}(\mathrm{r})/\partial x$ and $\partial\Delta\mathrm{B}(\mathrm{r})/\partial y$, from a complex image I^* (or its phase map). We treat the left sides of Eqns. (61) as the *x* and *y* components of a "phase-gradient" because they

are computed from the image phase, and we denote these components $g_x\left(I^*\right)$ and $g_y\left(I^*\right)$. Because the distortion field tends to be spatially smooth, the difference in phase angle between neighboring voxels can be expected to exceed π only rarely. As result any phase wrap between them is due simply to the restriction of the phase to the range $(-\pi,+\pi)$, and it is easy to show that such phase wrap will never cause error in the calculation of the angular difference in Eqn. (61). In those rare cases in which the difference exceeds π, the error is correctable by means of unwrapping. Thus the magnitude of the phase-gradient is approximately proportional to the local spatial variation of the distortion field $\Delta\mathrm{B}\left(\mathrm{r}\right)$. Figure 12 shows (a) a wrapped phase map. Figure 12 (b) and (c) are the computed g_y and g_x, respectively. As it shows, the phase-gradient maps have minimum phase-wrapping. A wrapped phase map computed using Eqn. (15) and the true phase $\gamma\Delta\mathrm{B}\times\mathrm{TE}$ share a common gradient. In Figure 13, we show a profile plot (indicated by a red line in Figure 12) of the wrapped phase map, the true phase map, and their common gradient. The phase-gradients are approximately proportional to the gradients of the distortion field.

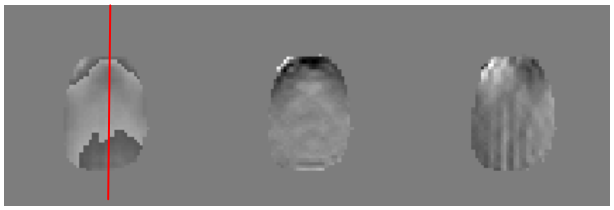

(a) **(b)** **(c)**

Figure 12. Computation of gradient maps of a distortion field from a wrapped phase map. (a) is a wrapped phase map. The gradient map of the distortion field in the *y* direction is shown in (b). The gradient map in the *x* direction is shown in (c). As it shows, the gradient maps have minimum phase wrapping because the distortion field tends to be spatially smooth.

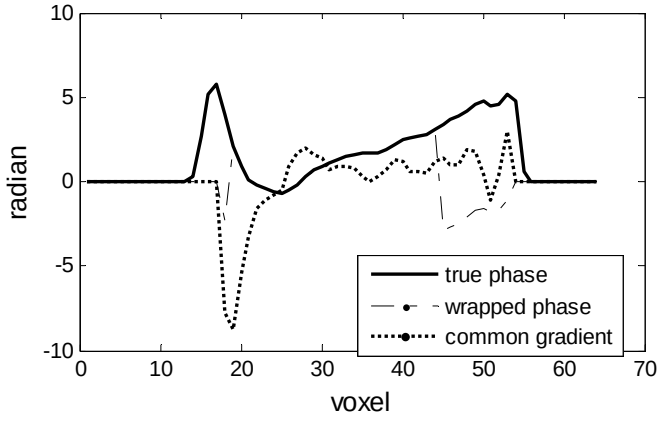

Figure 13. Profile plots. The solid line is a profile of a true phase. The dashed line is a profile of the corresponding wrapped phase. The dotted line is their common gradient. The gradients of a distortion field can be computed form a wrapped phase map.

As we discussed in Section 3.4 of Chapter III, the distortion field computed from a complex EPI lies in distorted space. Similarly the gradients we computed using Eqns. (61) are actually the gradients of the "distorted" distortion field $\Delta B(\mathbf{r}_1)$. The distortion field estimated using the image registration method based on Eqn. (56) is "undistorted" ($\Delta B(\mathbf{r})$). Hence, we have to perform a forward warping on the estimated field $\Delta B(\mathbf{r})$ before we can make a proper comparison between the gradients of the estimated

distortion field computed based on Eqn. (56) and the gradients computed based on Eqns. (61).

Given the above knowledge about the distortion field, we can construct a new cost function to estimate the distortion field ΔB_S. The new cost function contains three terms. The first term is the intensity term, given by Eqn. (56), which penalizes the intensity differences between the source EPI and the corrected and rigidly-transformed template EPI. The second term is the regularization term defined in Eqn. (60). We add a third term which penalizes disagreement between the gradients of the estimated distortion field ΔB_S and the gradients g_x and g_y based on Eqn. (61). This term is formularized as follows:

$$\psi_{\text{pha}}\left(\Delta B_S, I_S^*\right) = \left\| \frac{\partial h\left(\Delta B_S\right)}{\partial x} - g_x\left(I_S^*\right) \right\|^2 + \left\| \frac{\partial h\left(\Delta B_S\right)}{\partial y} - g_y\left(I_S^*\right) \right\|^2 . \qquad (62)$$

Note that we use h to represent the forward warping of the distortion field ΔB_S based on Eqn. (49). Eqn. (62) is a cost function that compares the gradients of the estimated distortion field with those computed from the image phase. We call this function the "gradient disagreement" of the distortion field. The complete cost function for estimation of the distortion field ΔB_S is given by

$$
\begin{aligned}
&\psi = \psi_{\text{int}} + \lambda_1 \psi_{\text{pha}} + \lambda_2 \psi_{\text{smooth}} \\
&\psi_{\text{int}} = \left\| f\left(I_{\text{S}}, \Delta \text{B}_{\text{S}}\right) - T_{\text{pha}}{}^{-1}\left(\vec{q}, \Delta \text{B}_{\text{S0}}\right) f\left(I_{\text{T}}, \Delta \text{B}_{\text{T}}\right) \right\|^2 \\
&\psi_{\text{pha}} = \left\| \frac{\partial h\left(\Delta \text{B}_{\text{S}}\right)}{\partial x} - g_x\left(I_{\text{S}}^*\right) \right\|^2 + \left\| \frac{\partial h\left(\Delta \text{B}_{\text{S}}\right)}{\partial y} - g_y\left(I_{\text{S}}^*\right) \right\|^2 \\
&\psi_{\text{smooth}} = \left\| \frac{\partial^2 \Delta \text{B}_{\text{S}}}{\partial x^2} \right\|^2 + 2\left\| \frac{\partial^2 \Delta \text{B}_{\text{S}}}{\partial x \partial y} \right\|^2 + \left\| \frac{\partial^2 \Delta \text{B}_{\text{S}}}{\partial y^2} \right\|^2 \\
&\arg\min_{\Delta \text{B}_{\text{S}}} \psi \\
&\Delta \text{B}_{\text{S}}\left(\text{r}\right) = \sum_{i,j} c_{ij} \phi\left(x - x_i\right) \phi\left(y - y_j\right)
\end{aligned}
\qquad (63)
$$

As with the standard non-rigid registration, this cost function matches the intensity of a distorted EPI to a corrected and rigidly-transformed template EPI. The motion compensation relies on $T_{\text{pha}}{}^{-1}$. Unlike standard methods, the gradients computed from the estimated distortion field are compared to those computed from the image phase. The constants λ_1 and λ_2 are weights that control the relative importance of each term and are obtained experimentally. The gradient disagreement term ψ_{pha} imposes a local spatial constraint on the estimated distortion field. This term is time dependent because it is computed from the EPI itself. With this new cost function, both the phase and the intensity of the EPI will affect the entire optimization process for the estimation of $\Delta \text{B}_{\text{S}}$. Hence, it is expected that the estimated distortion field based on this cost function will be more accurate than that computed with intensity information alone. This hypothesis will be verified in Chapter V.

Many methods are available to solve the non-linear optimization problem defined in Eqns. (63), and because the source EPI and the template EPI in Eqns. (63) share

exactly the same imaging parameters, it is relatively easy to minimize ψ and hence relatively easy to find an estimation of the distortion field based on non-rigid registration. We have found that a simple gradient-descent method is sufficient, in which the gradient of the cost function with respect to each of the unknown parameters, namely the coefficients of the basis functions c_{ij}, are computed. The parameters are updated along the directions with steepest gradients. Because the initial estimate of the distortion field ΔB_{S0} is close to the true distortion field ΔB_S, a fixed number of iterations is chosen as the stopping criterion.

The gradient of the cost function in Eqns. (63) with respect to each unknown coefficient of the basis functions can easily be computed. For ψ_{int} and ψ_{smooth}, analytic calculation is possible because of the smoothness property of the B-spline basis function, the computation of $\partial f / \partial c_{ij}$ being performed using chain rule. The gradient of ψ_{pha} with respect to the unknown parameters cannot be computed analytically because of the form of h. For this term a finite difference method is employed instead. We use ΔB_{S0} as an initial estimation of the distortion field. ΔB_{S0} is first fitted with B-splines, and then the coefficients after this fitting are provided as the initial values for the unknown coefficients c_{ij}.

4.5. Suggested algorithm to estimate dynamic distortion fields

Step 0: One image in an EPI series, typically the first, is chosen as a "template" image, I_T. The remaining images of the series are designated as "source" images. The

image distortion of the template image is corrected using the field-map method to produce $f\left(I_{\mathrm{T}},\Delta \mathrm{B}_{\mathrm{T}}\right)$.

For each source image I_{S} the following steps are taken:

Step 1: An approximate inhomogeneity field $\Delta \mathrm{B}_{\mathrm{S0}}$ is calculated using the phase-map method (Chapter III), and distortion correction is performed on the source image using $\Delta \mathrm{B}_{\mathrm{S0}}$ to produce $f\left(I_{\mathrm{S}},\Delta \mathrm{B}_{\mathrm{S0}}\right)$.

Step 2: A rigid transformation T_{pha} for motion compensation of the source relative to the template is computed based on the corrected template and the approximately corrected source.

Step 3: The template EPI is transformed according to ${T_{\mathrm{pha}}}^{-1}$ to produce ${T_{\mathrm{pha}}}^{-1}\left(\vec{q},\Delta \mathrm{B}_{\mathrm{S0}}\right) f\left(I_{\mathrm{T}},\Delta \mathrm{B}_{\mathrm{T}}\right)$.

Step 4: The gradients, g_x and g_y of the distortion field are computed based on the phase of the distorted EPI.

Step 5: With $\Delta \mathrm{B}_{\mathrm{S0}}$ as an initial value, the unknown distortion field $\Delta \mathrm{B}_{\mathrm{S}}$ is estimated by minimizing the cost function defined in Eqn. (63). The optimization stops with a defined criterion.

4.6. Conclusion

Image registration is an important post-processing technique for motion compensation and distortion correction of EPI series. Rigid-body registration is insufficient to remove the effect of motion-distortion in EPI time series, and the success

of non-rigid registration in the estimation of dynamic distortion fields in EPI series depends on accurate motion compensation and effective constraints. We have proposed in this chapter an optimization framework for estimating dynamic distortion fields in EPI time series based on rigid and non-rigid registration in which both the intensity and the phase of EPIs are utilized throughout the optimization process.

The phase-map method, which we described in Chapter III provides in this chapter an initial estimation of the dynamic distortion field from which a more accurate motion compensation is obtained. The phase of each EPI provides gradient information for its distortion field. This gradient information is utilized to constrain the estimation of the distortion field in a non-rigid registration method. It is expected that these phase gradients enforce an effective constraint to mitigate the local minimum problem in the non-rigid registration. Furthermore, the registration method, because of the integration of intensity information, serves to reduce the estimation errors in the phase-map method and to generate a smoother distortion field with reduced artifacts. An evaluation of this method is presented in next chapter.

CHAPTER V

VALIDATION AND COMPARISON

In chapter III and chapter IV, we proposed a phase-map method and a registration method, respectively, for the estimation of dynamic distortion fields in EPI time series. We have presented theoretical derivations in detail. In this chapter, we aim to validate these two methods with experiments and quantitative evaluations. We conduct a validation based on two types of image data. In order to isolate the temporal variation of image intensity in EPI series caused by unknown motion and unknown sources, we use simulated EPI series of human brain with realistic distortion fields and realistic motion. We evaluate the performance of our proposed methods by comparing our results with the known distortion fields and a distortion-free EPI, which provide ground truth. We quantify the estimation errors of the distortion field and analyze the capability of our methods in the correction of dynamic image distortion. We also compare the performance of our methods with the traditional field-map method and the standard non-rigid registration method.

We also employ our methods on real EPI data from Philips 3T MR scanner. A physical phantom is carefully designed to provide a known geometry. We create a variation in the distortion field of the phantom by rotating the physical phantom inside the scanner. The ground-truth field maps are acquired by using the field-mapping method with dual-echo GE-EPIs. Our phase-map method is then applied to estimate the distortion field when the phantom lies in a new orientation. We compare our estimation results with

the ground truth. The geometry of the EPI before and after a correction with the traditional field-map method and our phase-map method is quantitatively compared.

Finally, we compare different strategies that are based on image phase and image intensity for the estimation of dynamic distortion fields. The evaluation is performed based on simulated EPI series with motion and a varying distortion field. The variation of the distortion field is generated using an MR simulator [23] based on the orientation of the susceptibility distribution of air-tissue of a human head. The estimation errors of the distortion fields of different strategies are quantified.

5.1. Simulated EPI series

To validate our methods, we create simulated EPI series with known ground truth [23;83]. A static distortion field is generated from a real field map acquired experimentally. The field map is then processed and regularized in order to reduce artifacts. GE-EPI series are simulated with an image size of 64x64x28, phase-encoding bandwidth of 2000 Hz, and echo time of 35 ms. The field of view is 240 mm in the *x*-*y* plane and 137.2 mm in the *z* direction. Each EPI has a voxel size of 3x3x4.9 mm. The phase-encoding direction is Anterior and Posterior (AP). A distortion-free EPI is generated by simply turning off the static field inhomogeneity in the simulation. EPIs with a TE of 27 ms are also simulated as reference images for performing both the field-map method and our phase-map method. Gaussian noise is added to the real channel and imaginary channel of the simulated images separately. Both the magnitude and the phase of the EPI are saved for further processing. Figure 14 shows (a) the intensity of the distortion-free EPI (multiple slices), (b) the distorted EPI, (c) magnitude (b) minus

magnitude (a) , and (d) the corresponding distortion field that we applied. A plot of the intensity profile and the distortion field profile (indicated by red vertical lines in Figure 14) is shown in Figure 15 to demonstrate the intensity changes of the EPI caused by image distortion.

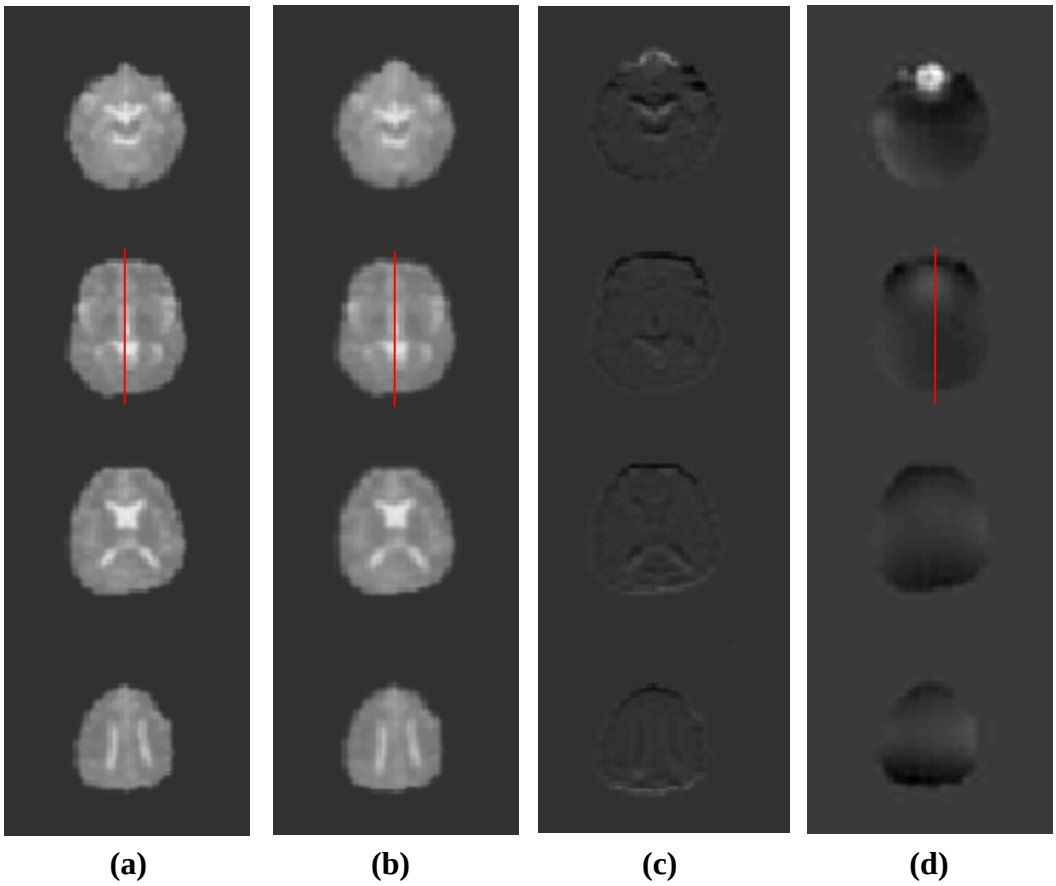

Figure 14. (a) Simulated distortion-free EPI, (b) distorted EPI, (c) magnitude (b) minus magnitude (a), and (d) the corresponding distortion field. Noticeable image distortion can be observed in (c). The geometric distortion is confined to the phase-encoding direction which is vertical in this figure.

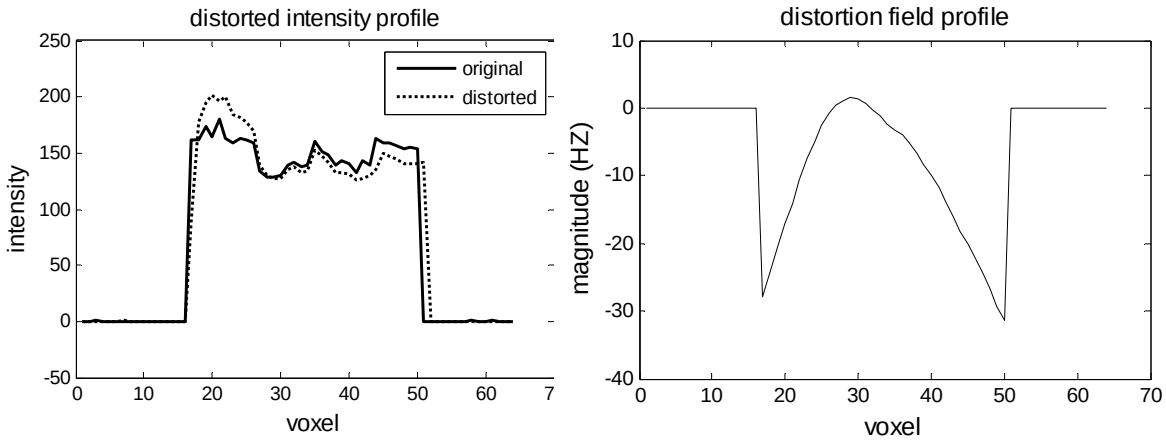

Figure 15. Changes of intensity profile (shown on the left) caused by distortion field (shown the right). Both geometric shift and intensity distortion are noticeable. The position of this profile is shown as red lines in Figure 14.

In order to simulate the variations of the distortion field caused by external sources (e.g. variation of distortion field induced by respiration) in EPI, we create a perturbed distortion field by modifying the original distortion field. We extract the fluctuation of distortion fields between two adjacent time points from a real EPI time series. Then we vary the scale of this fluctuation to simulate variation in the size of the distortion field, as for example during respiration. A slice of the original distortion field and the corresponding perturbed distortion field (in the unit of voxel shift) are shown in Figure 16. By changing the scale of this fluctuation, we can alter the magnitude of the distortion-field variation. According to a study from Raj *et al.* [34;89], the susceptibility changes caused by respiration for a 1.5 T scanner may lead to a shift of image on the order of 0.1 pixel. At 7 T, it is expected that there could be a shift of about half of an pixel or higher in the EPI caused by respiration. We choose the scale of the distortion-

field variation based on this expectation to simulate the dynamic distortion fields induced by respiration.

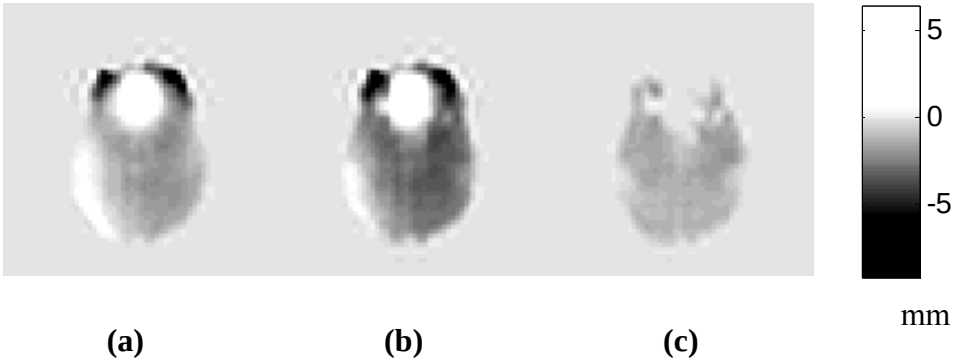

Figure 16. Generation of perturbed distortion field. (a) is the original field map, (b) is the perturbed distortion field, and (c) equals (b) – (a), which is the distortion-field variation. The distortion-field variation is extracted from the fluctuation of distortion fields in a real EPI series. The scale of this fluctuation is chosen according to the expected effect of respiration.

We generate simulated EPI time series with motion sequences extracted from real fMRI studies and a varying distortion field induced by motion. Two types of motion are employed. One type of motion is in-plane motion (perpendicular to the B-field, as defined in Chapter II). In the series of EPI with in-plane motion, only the direction of the image distortion will vary with time. The other type of motion is out-of-plane motion (also defined in Chapter II). For this type of motion, not only the direction but also the magnitude of the image distortion varies with time. We chose two motion sequences of each type, which were extracted from a typical human head in fMRI. The rotation is within a range of -4^{o} to 4^{o}, and the translation is within a range of -2 mm to 2 mm. To simulate the magnitude changes of the distortion field induced by motion, we start with a distortion field calculated for a given head orientation, then we choose an out-of-plane

motion pattern for the head and calculate the temporal variation of the distortion field induced by that motion using an MR simulator [23]. Each EPI at each time point in the series is then distorted differently according to the corresponding distortion field calculated at that time point.

5.2. Real EPI data of a physical phantom

We designed a physical phantom to validate our methods. The phantom is a cylinder that is 6 inches in diameter and 6 inches in height. It is made of plastic with susceptibility close to that of water. The liquid in the cylinder is water solution of 0.1 mM $MnCL_2$. There are five small cylinders within in the 6-inch cylinder whose axes are parallel to that of the larger cylinder with diameters of 0.5 inch, 0.75 inch, and 1 inch. The smaller cylinders are filled with powdered bone, with tightly fitting glass rods or with air (half of the cylinder is inserted with glass to reduce loss of signal) in order to create a spatially varied field inhomogeneity with local variations. A schematic of the phantom is shown in Figure 17.

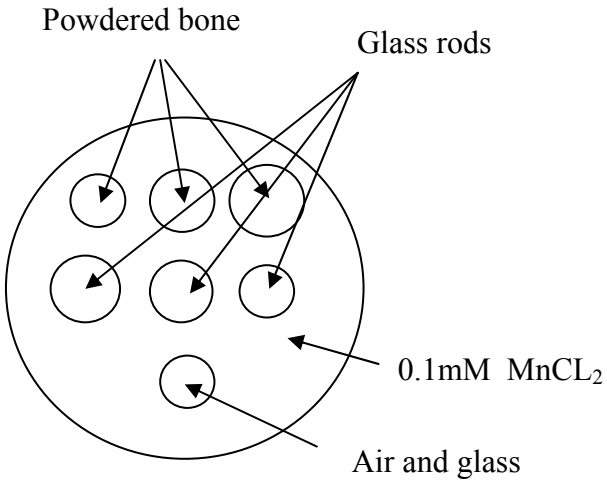

(a)

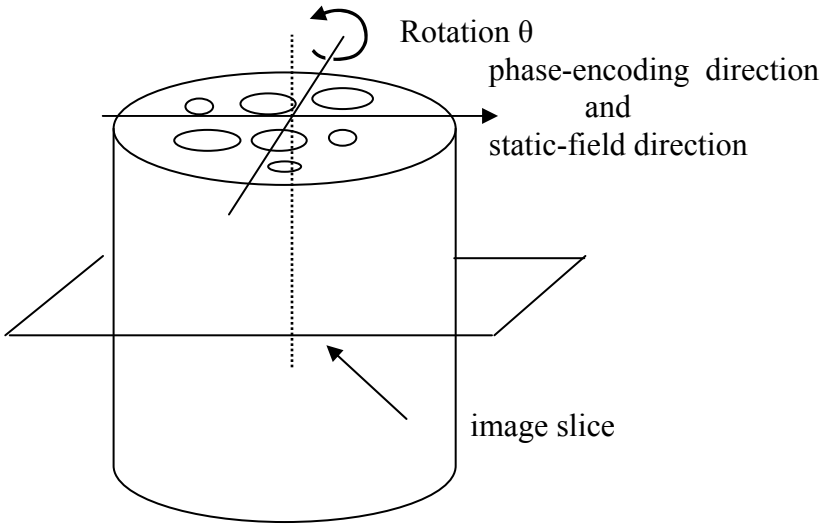

(b)

Figure 17. Physical phantom. Several small cylinders with different diameters filled with powdered bone, glass rods, and air are placed within a cylinder containing a solution of Manganese Chloride to create spatially varied field inhomogeneity. The rotation is described in the text.

The phantom is placed in the scanner so that its cylindrical axes are perpendicular to the static field. The orientation of the image acquisition relative to the static field and the phase-encoding gradient is shown in Figure 17 (b). Two-shot GE-EPI images are obtained on a Philips 3T MR scanner with an image size of 80x80x24, a phase-encoding bandwidth of 4497 Hz, and a TE of 12 ms. The field of view is 240 mm in *x*-*y* plane and 108 mm in *z* direction. The image has a voxel size of 3x3x4.5 mm. A reference GE-EPI with a TE of 13 ms TE is also acquired for calculating a field map. We also acquired a multi-shot GE image as an "anatomical" image because of the similarity of the acquisition parameters to that of the anatomical image acquired to accompany a fMRI series. Figure 18 shows three views of the anatomical images of the phantom (top rows)

and the corresponding EPI (bottom rows). The majority of the field inhomogeneity is seen near the interfaces of tissues with differing susceptibility. Since glass has a susceptibility that is closer to that of water, the cylinders with glass experience less image distortion than the cylinders with bone and air. Air is supposed to induce more image distortion than bone and glass. The bigger the cylinder is, the more distortion we will have. It can be seen in the regions indicated by the red arrows that the cylinders with bone, glass, and air experience different extents of image distortion.

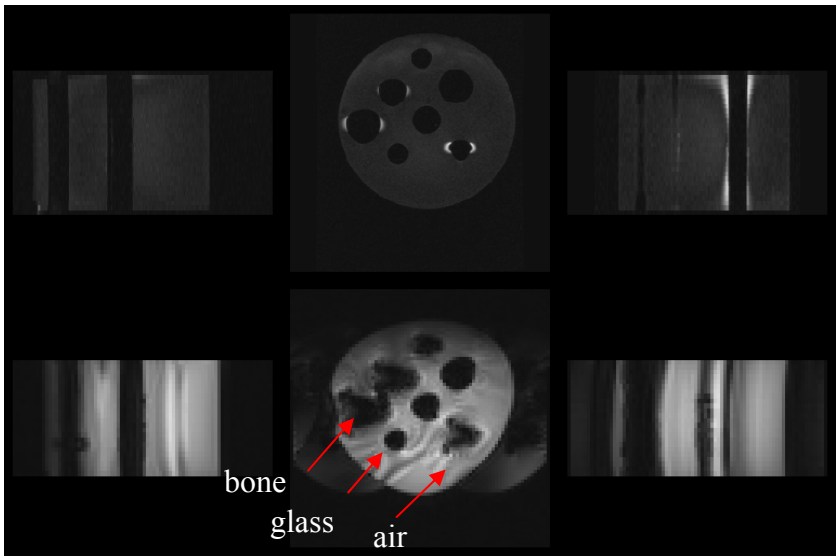

Figure 18. Anatomical image (top row) and the corresponding GE-EPI (bottom row) in three different views. Severe image distortion can be observed at tissue interfaces (indicated by red arrows). Different susceptibility patterns induce different extents of image distortion.

Both the magnitude and the phase of the acquired EPI are saved for processing. In order to create temporal variation for the distortion field, we rotate the phantom in the scanner slightly (5 to 10 degrees) about an axis other than the static field direction (Figure 17 (b)) and then re-acquire the EPI. This way, we expect to have an EPI with

slightly different distortion field. Again, a reference EPI with a TE of 13 ms is acquired to compute a ground-truth field map at the new orientation.

5.3. Validation of our phase-map method

The temporal variation of the distortion fields in EPI time series of the head can be caused either by external sources (e.g. respiration) or by head motion. In our experiments, we consider both effects. Our first experiment is to validate our phase-map method in recovering the temporal variation of the distortion field induced by respiration. As we mentioned in the previous section, we perturbed an original distortion field to represent a variation of the field with time other than that resulting from movement of the head itself. The resulting image distortion of the EPI will then vary with time because of the temporal variation of the distortion field. Figure 19 shows the percentage of the temporal variation of image intensity of the EPI caused by the variation of the distortion field. Comparison with Figure 15(c), which shows the variation of the distortion field, confirms that temporal intensity changes occur where the distortion field varies temporally.

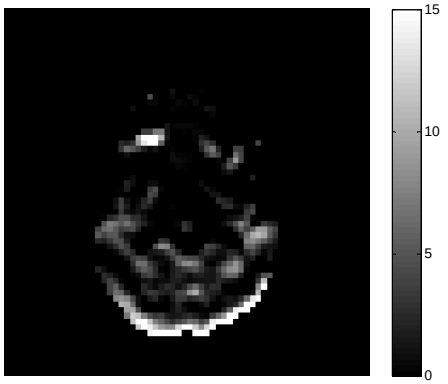

Figure 19. The percentage of intensity changes of the EPI is caused by the temporal variation of the distortion field.

We can estimate this variation of the distortion field using our phase-map method. The result is compared with the true variation of the distortion field we modeled. The comparison results are shown in Figure 20. As it shows, our phase-map method properly recovers the variation of the distortion field from external sources when the head remains stationary.

Figure 20. Estimated variation of the distortion field (left) using our phase-map method and the true variation of the distortion field (right). Their similarity indicates that, when the head remains stationary, our phase-map method can recover the variation of the distortion caused by external sources (respiration).

To evaluate the performance of our method on the correction of dynamic image distortion from external sources, the EPI before and after our correction and after the traditional field-map correction are demonstrated in Figure 21. Figure 21 shows a set of difference images that result from subtracting a distortion-free EPI from (a) the magnitude of the original EPI, (b) the magnitude of the EPI corrected with the traditional field-map method, (c) the magnitude of the EPI corrected with our phase-map method and (d) the EPI corrected with the ground-truth distortion field. Not surprisingly, (a) demonstrates severe image distortion. Using the field-map method, the image distortion is largely removed as shown in (b), but noticeable intensity error induced by the variation

of the distortion field still exists (indicated by red arrows). Our correction method reduced the image distortion to a great extent in the internal region (c) with a performance comparable to (d), which is the image correction resulting from the use of the ground truth field.

Figure 21 Difference images obtained by subtracting a distortion-free EPI from (a) the magnitude of the original EPI, (b) the magnitude of the EPI corrected with the traditional field-map method, (c) the magnitude of the EPI corrected with our phase-map method and (d) the EPI corrected with the ground-truth distortion field. Difference (d) represents the best scenario that can be achieved by means of distortion correction. The red arrows highlight internal errors remaining in (b) that are reduced in (c).

In our phase-map method, we make the assumption that the distortion field varies slowly with time, so that the temporal phase variation has correctable phase wrapping. By altering the magnitude of the distortion field, we are able to evaluate the capability of our phase-map method to recover the temporal variation of the distortion field. In Figure 22, we show an estimated field-variation (left) and the ground-truth field-variation when the when the field variation reaches a level about 20HZ, which is equivalent to about 2.3 mm spatial shift in image space. The large estimation errors (indicated by a red arrow) indicate that the assumption that the distortion field varies slowly with time is violated

when the change in the distortion field exceeds 20 Hz. As a result, the temporal change in image phase, which is induced by the variation of the distortion field, experiences phase wrapping. Fortunately, the temporal variation of the distortion field in EPI time series induced by external sources such as respiration is typically small [34] increasing the likelihood of success for our method. However, the phase-map method will fail in those regions where the distortion field has dramatic temporal variations. In this case, an incorporation of intensity information into our registration approach, which we described in Chapter IV, will help to reduce the estimation errors. We will explore that reduction in Section 5.4.

Figure 22. Example of error in our estimation of distortion-field variation caused by temporal phase-wrapping. The left is the estimated distortion-field variation, and the right is the ground-truth distortion-field variation. Large errors occur in regions where the distortion field has dramatic temporal variations.

We use simulated EPI series with both in-plane motion and out-of-plane motion (motion is described in Section 5.1) to evaluate the performance of our phase-map method on the correction of the effect of motion-distortion. The distortion field at each time point of the time series is estimated using our method. In the traditional field-map

method, only a static distortion field can be accessed. It is expected that there will be large field-estimation errors when the dynamic distortion fields are approximated by a static distortion field. In order to visualize this effect, a comparison is made in Figure 23. The left column shows the errors when we use a static distortion field to approximate a dynamic distortion field at a selected time point. The right column shows the errors when we represent the dynamic distortion field with our phase-map method. As expected, noticeable errors are found when we approximate the dynamic distortion field using a static field map. Our phase-map method provides a much more accurate representation of the distortion fields in EPI series except in a few isolated areas of very large distortion.

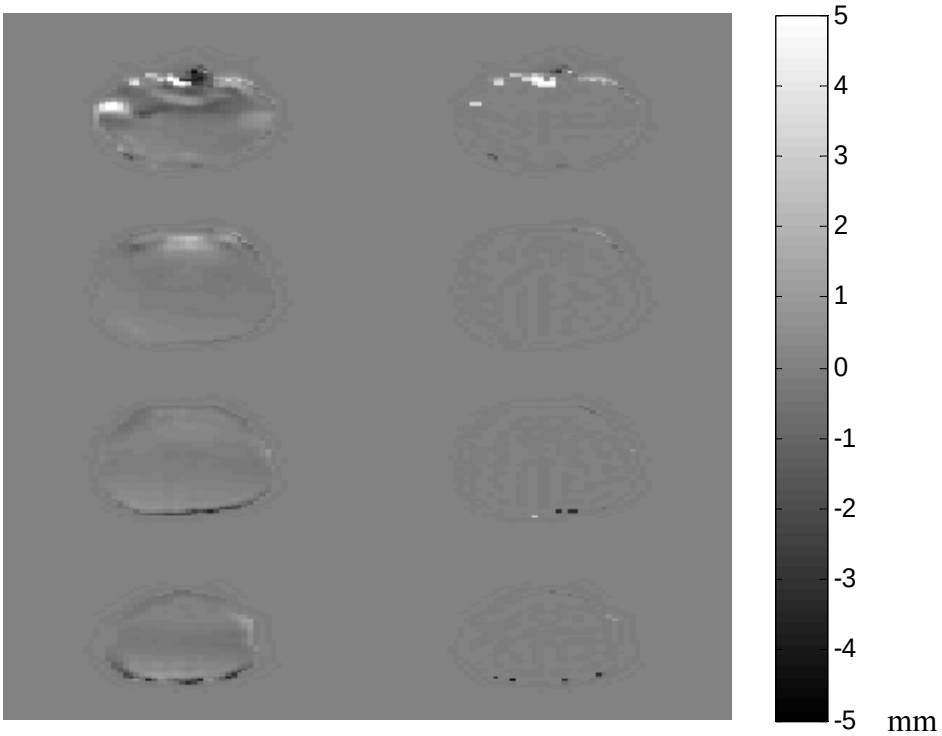

Figure 23. Estimation errors of the distortion field (multiple slices are shown). The result from approximating the dynamic distortion field with a static distortion field is shown on the left. The estimation result with our phase-map method is shown on the right. Noticeable errors found on the left demonstrate the importance of having a dynamic distortion field for each EPI. Our phase-map method properly estimates the dynamic distortion fields except in a few isolated areas of very large distortion.

To show the difference between using distortion correction based on the field-map method and that based on our phase-map method, the distorted EPI at a selected time point before and after correction is compared with distortion-free images. The results are shown in Figure 24. Figure 24 shows difference images obtained by subtracting the magnitude of the distortion-free EPI from (a) the magnitude of the original EPI, (b) the magnitude of the EPI corrected with the field-map method, and (c) the magnitude of the EPI corrected with our phase-map method. As can be seen, the intensity variations in EPI series caused by dynamic distortion field have been reduced noticeably using our phase-map method.

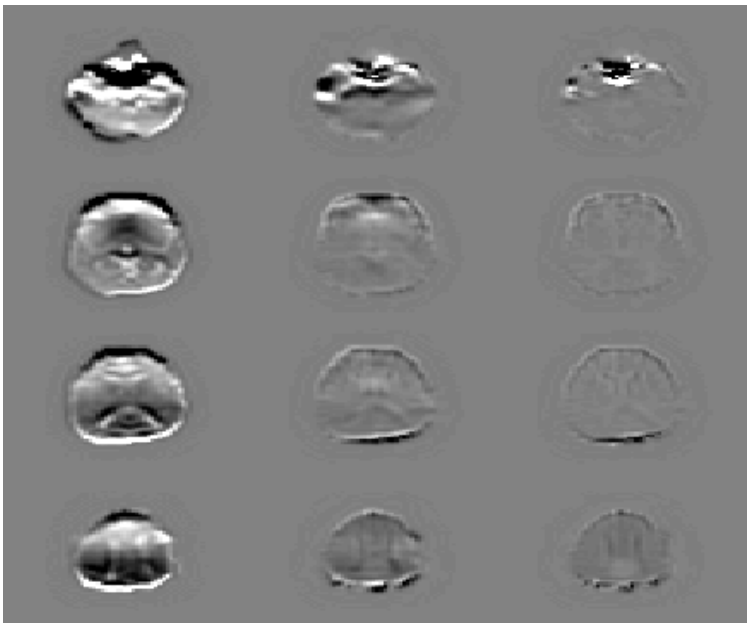

(a) **(b)** **(c)**

Figure 24. Difference images obtained by subtracting the magnitude of the distortion-free EPI from (a) the magnitude of the original EPI, (b) the magnitude of the EPI corrected with the field-map method, and (c) the magnitude of the EPI corrected with our phase-map method As it shows, except for a few strongly perturbed areas, our phase-map method noticeably reduces the temporal intensity variation caused by dynamic image distortion.

To further quantify the improvements of using our phase-map method over the traditional field-map method approach, the temporal evolution of Root Mean Square (RMS) intensity variation of the original EPI series with both in-plane motion and out-of-plane motion are calculated based on the sum of the squared differences between the magnitude of the EPI at each time point and that of the first EPI (corrected). The ideal value would be zero throughout the series. The same calculation is also applied to the EPI series after distortion correction with the traditional field-map method and with our phase-map method. The motion compensation that we described in Chapter IV is applied to the EPI series before we perform the calculation. The results are shown in Figure 25.

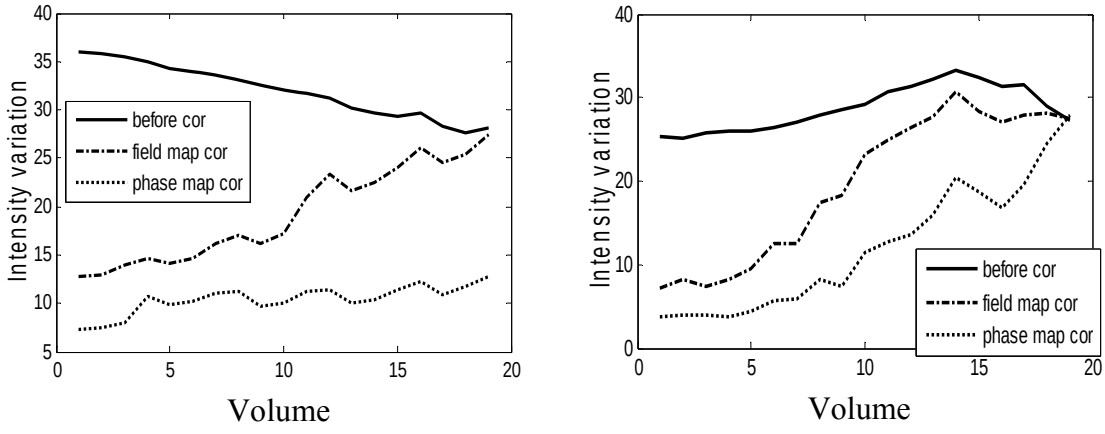

Figure 25. Temporal RMS intensity variation of EPI series before and after correction. The left is with only in-plane motion, the right is for the EPI time series with only out-of-plane motion. Solid lines indicate the original RMS intensity variation. Dashed lines indicate the RMS intensity variation after the field-map correction. Dotted lines indicate the RMS intensity variation after our phase-map correction. As can be seen, the field-map correction works fairly well at the beginning of the time series when the field has not changed much but fails badly later in the series. Our phase method effectively reduces the temporal RMS intensity variation for in-plane motion throughout the series and suffers from about half the error through the first 10 to 12 time points.

As expected, the distortion correction based on the traditional field-map method works well at the beginning of the time series when the dynamic distortion field does not deviate from the static distortion field much. Our phase-map method is more effective in reducing the temporal intensity variations of the original image series than the field-map method, and it keeps the errors low throughout the series for in-plane motion. As time progresses, however, the correction performance is markedly reduced for out-of-plane motion. The fact that the intensity errors get larger for out-of-plane motion for phase-map correction can be explained by the fact that, when there is sufficient movement during the time series, the required phase information at some physical locations is not be available because they have moved into the background area of the previous images. The variation of the distortion field can be determined accurately only in those regions with sufficiently high SNR in both the current EPI and the previous EPI. The other regions will exhibit high estimation errors primarily near the boundaries of the foreground of the image volume. These errors can be reduced by incorporating intensity information via the registration method that we described in Chapter IV.

To quantify the correction in areas away from the image boundaries and to evaluate the potential effects of the correction of dynamic distortion in EPI series on activation analysis in these areas, an interior region of interest in the EPI is chosen (shown as a red circle in Figure 26), and the mean temporal intensity variation in this region is computed.

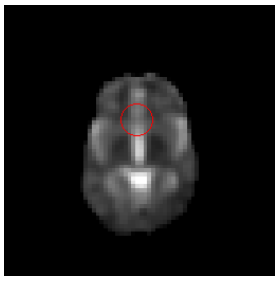

Figure 26. A region of interest in EPI for evaluation.

We plot the percentage of the temporal RMS intensity variation of the distorted EPI in the region of interest relative to the first EPI (corrected) in the time series. The results are shown in Figure 27. As it shows, both the traditional field-map method and our phase-map method help to reduce errors in this region. However, there is still about 10% intensity variation in the time series after the field-map correction. The intensity variation is considerably above the typical activation level (2-4%) for fMRI and thus can seriously compromise activation analysis. After our phase-map correction, the intensity changes are reduced below this level.

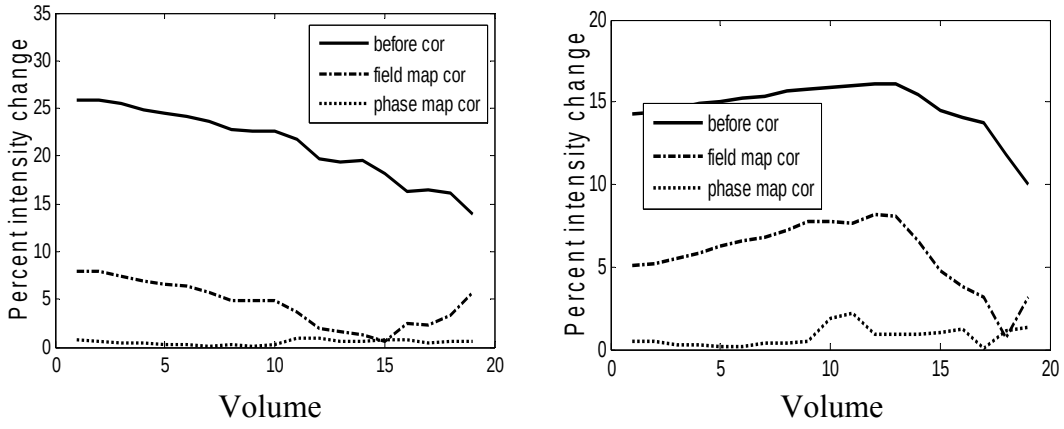

Figure 27. Percentage of temporal RMS intensity variation in region of interest for EPI time series with in-plane motion(left) and out-of-plane motion(right). As it shows, both the field-map method and our phase-map method help to reduce error in this region. But there is still about 10% intensity variation in the time series after the field-map correction, which is above the typical activation level. After our phase-map correction, the intensity variation is reduced below the activation level.

We now examine motion compensation, in which we apply rigid-body realignment on the original EPI series, on the EPI series corrected with the traditional field-map method, and on the EPI series corrected with our phase-map method. We found that for purely in-plane motion, motion estimation for all these methods agrees with the ground truth to within one-half mm translation and one-half degree rotation. The

motion compensation of the EPI series with out-of-plane motion, however, was strongly affected by the effect of motion-distortion. Figure 28 shows the results for out-of-plane motion. It can be seen that a more accurate motion estimation was achieved after a distortion correction with our phase-map method than a correction with the field-map method or no correction on the original EPI series. As we can see, the estimation of the out-of-plane rotation angle is biased when we calculate it on the basis of the original EPI series and on the series that is corrected with the traditional field-map method. The motion compensation on the EPI series that is corrected with our phase-map method is also biased but is closer to the ground truth. This verifies the hypothesis we proposed in Chapter IV that a transformation T_{pha} will be more accurate than either T or T_{fld}. Thus, our experiments show that motion compensation should be performed on the EPI series that have been corrected by means of dynamic distortion fields.

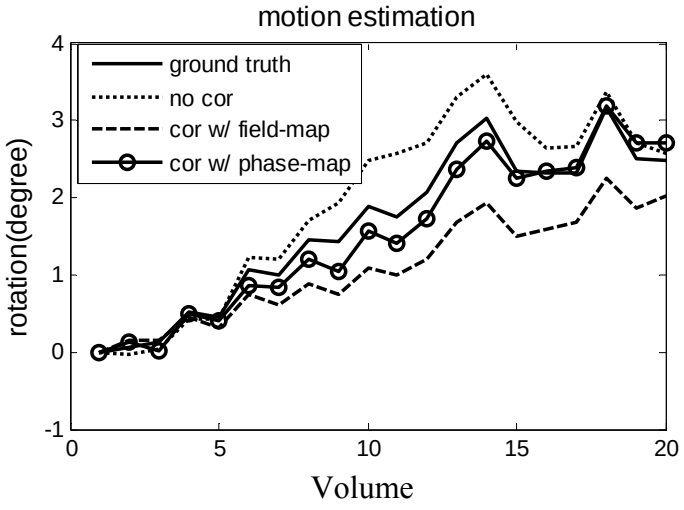

Figure 28. Effect of distortion correction on motion compensation. It shows that the motion compensation should be performed on the EPI series with a correction by means of dynamic distortion fields.

We also validated motion compensation for our phase-map method based on the phantom EPI data that we acquired. When the phantom lies in two different orientations (the rotational axis is shown in Figure 17 (b)), the corresponding EPIs experience different distortion fields. At the first orientation, dual-echo EPIs were acquired. These two images can be used to compute the corresponding distortion field. According to our theory, if we are given the phase information of an EPI corresponding to a new orientation, then we can use our phase-map method to estimate an updated distortion field. Figure 29 shows the estimation error of the distortion field (absolute difference) for a new orientation using both the traditional field-map method (left image) and our phase-map method (right image). As it shows, our phase-map method reduces the estimation errors in most internal areas of the image. Note that the estimation errors near the edges of the foreground of the right image, indicated by red arrows, are largely due to the fact that a part of the phantom has moved into a position formerly outside the phantom, so that it is not possible to get an accurate measurement of the phase change, as explained above. This effect remains to be an issue in the phase-map method, but it can be mitigated by means of image registration as we will see in Section 5.4

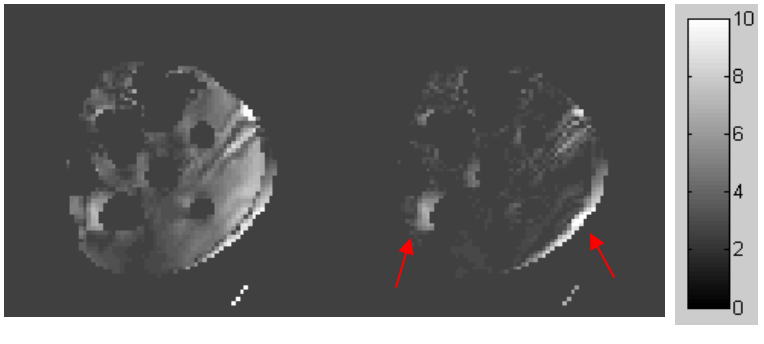

Figure 29. Absolute difference between estimated distortion field and ground truth. Left is from the field-map method. Right is from our phase-map method. As it shows, the field-map method is not accurate when the distortion field varies with time. Our phase-map method reduced the estimation errors.

To quantify the performance of our methods, we plotted the mean absolute difference between the estimated distortion field for the new orientation of the phantom and the ground truth distortion field versus slice number, and the results are shown in Figure 30 . As expected, an approximation of the distortion field for a new orientation using a static field-map suffers from large errors (solid line in Figure 30). The estimation errors are reduced by using our phase-map method (dashed line). Another important fact we noticed is that, because the real EPI data has a very low SNR, the utilization of the regularization factor, which we described in Chapter III further reduced the estimation errors (dotted line). Regularization had a negligible effect on the computer simulations above, in which SNR was higher.

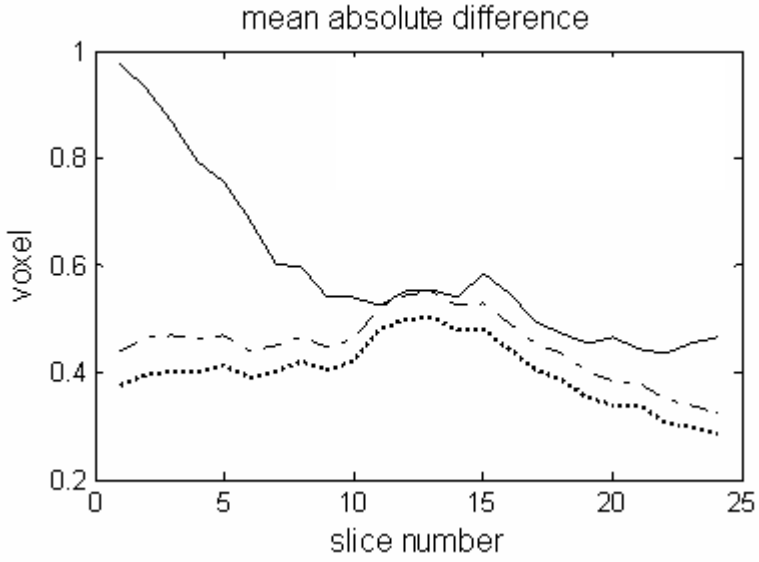

Figure 30. Mean absolute difference between the estimated distortion field and the ground truth. Field-map approximation (solid line) suffers from large errors near one end of the phantom. Our phase-map method (dashed line) dramatically reduced the estimation errors. The integration of a regularization term (dotted line) is also important when the SNR of the EPI is slow.

We performed distortion correction of the EPI at the new orientation using both the field-map method and our phase-map method. We approximated the distortion-free EPI with a corrected EPI by means of a field map that is calculated based on an extra scan at the new orientation. We compared the corrected EPI using the traditional field-map method and the corrected EPI using our phase-map method with the distortion-free image. Figure 31 shows the mean absolute difference of the image intensity between the corrected EPI and the distortion-free EPI for all slices. (The mean absolute intensity for the phantom is about 1000). As it shows, a correction based on our phase-map method (dashed line) reduces intensity errors somewhat more than the traditional field-map method (solid line), but the incorporation of a phase regularization factor has a large influence on the reduction of intensity errors (dotted line).

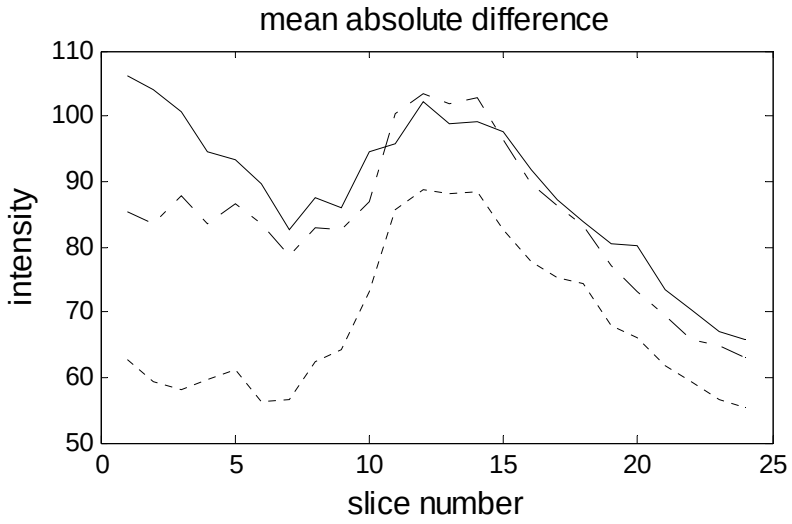

Figure 31. Correction of EPI. A correction based on our phase-map method (dashed line) reduced intensity errors somewhat more than the traditional field-map method (solid line), but the incorporation of a phase regularization factor (dotted line) greatly increased the reduction.

In our phase-map method, a phase-unwrapping step needs to be taken when we compute the temporal phase variation. We need to pre-process the phase-map difference defined in Eqn. (43) before it can be used in our phase-map method. Figure 32 shows the original phase-map difference (left image) and the phase-map difference after phase unwrapping (right image). As it shows, the phase-wrapping ambiguity (indicated by red arrows) in the original phase-map difference is removed in the processed phase-map difference by means of a phase-unwrapping algorithm proposed in [90].

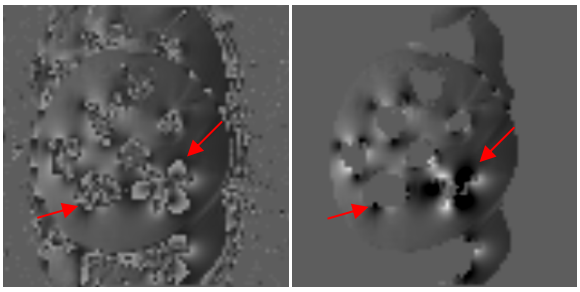

Figure 32. Temporal phase unwrapping in our phase-map method. Left is the original temporal phase difference. Right is the phase difference after phase unwrapping. Note that most regions in the left image exhibit minimum phase wrapping, which makes it relatively easy to perform a successful phase unwrapping for a whole image.

Figure 33 shows the original phantom EPIs and the corrected EPIs. Figure 33 (a) is the corrected EPI with a ground-truth field map, which represents a distortion-free EPI. It represents the best image quality that can be achieved by means of a distortion correction obtainable by using a field map acquisition for each EPI acquisition. Figure 33 (b) is the original distorted EPI. The corrected EPIs with the traditional field-map method and our phase-map method are shown in (c) and (d) respectively. We draw the contours

of the cylinders in the distortion-free EPI with green lines, and then superimpose them onto the other EPIs.

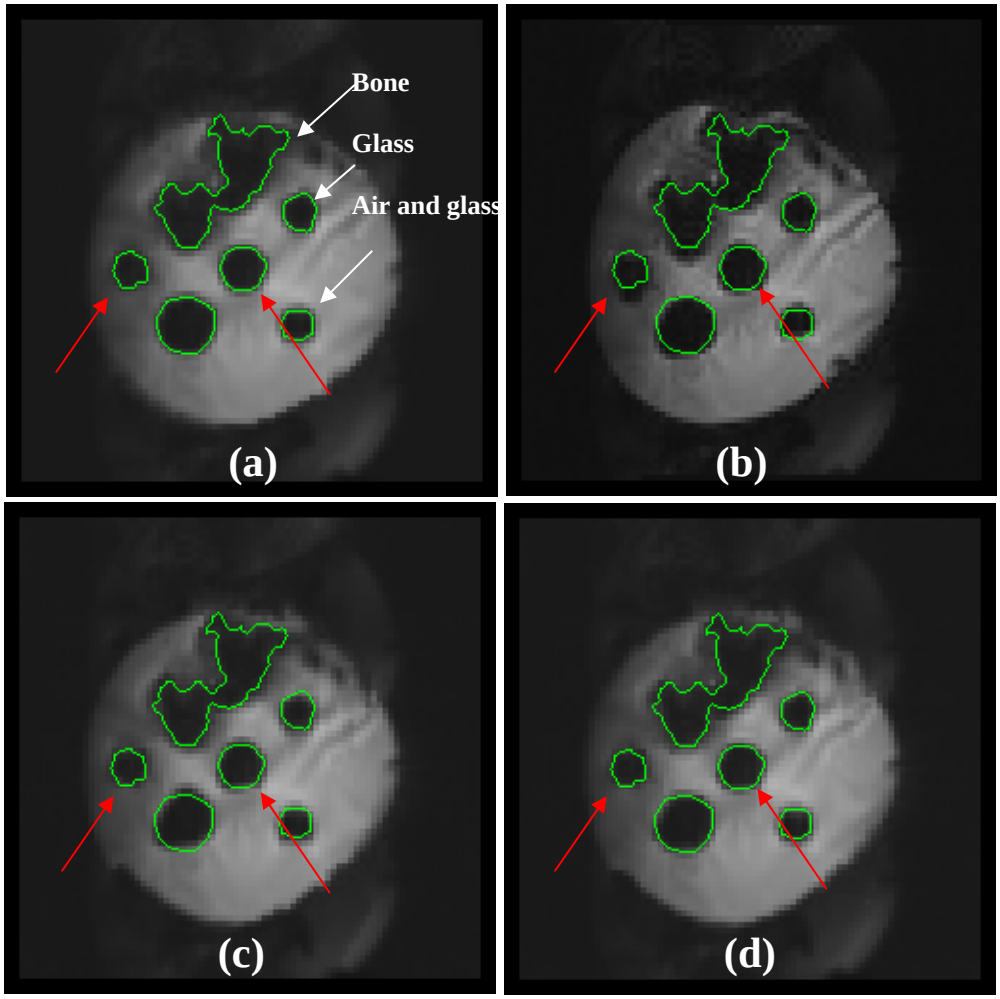

Figure 33. Distortion correction of phantom EPI. (a) is the corrected EPI with a ground-truth field map. (b) is the original EPI. (c) is the corrected EPI with the traditional field-map method. (d) is the corrected EPI with our phase-map method. As it shows, our phase-map method achieves a comparable performance as the correction with the ground-truth field map in terms of recovering the warped geometry of the phantom.

As we can see, the large and medium cylinders filled with of powdered bone could not be corrected successfully even with a correction based on a ground-truth field map because of loss of signal. For all sizes of cylinders with glass rods, the corrected EPI in (a) demonstrates better geometry compared with the original EPI shown in (b). In (c), the geometry of the medium cylinder and the small cylinder with bone are improved compared with the original EPI (b), but the geometry of all sizes of cylinders with glass rods the small cylinder with air still suffer from noticeable warping. It means a correction with the field-map method may be inaccurate. In (d), the EPI corrected with our phase-map method demonstrates a comparable quality as (a) in terms of recovering the warped geometry of the phantom. There is an improvement over (c) for all the glass cylinders and the air cylinder, most noticeable in the largest glass cylinder (bottom left). Thus, our dynamic phase-map method estimates a distortion field that is closer to the ground truth than the static field-map method.

To quantify the performance of the field-map method and our phase-map method on recovering the warped geometry of different cylinders, we measure the DICE similarity [91] of the segmented circles from the original EPI, from the EPI corrected with the ground-truth field map, from the EPI corrected with the traditional field-map method, and the corrected EPI with our phase-map method. The Dice similarity = $2|A \cap B| / (|A| + |B|)$, where A and B are sets of the voxel in the respective shapes being compared. The higher the similarity, the better correction performance is achieved, and it ranges from 0, meaning no similarity, to 0.8, meaning good similarity, to 0.9, meaning excellent similarity, to 1 at perfect similarity. We compute similarities by comparing each

corrected shape in turn as *A* with the ground-truth field map as reference *B*. Table 1 summarizes the comparison results.

Table 1. Dice similarity of the segmented circles from original EPI and the corrected EPI

cylinders	Small (bone)	Large (glass)	Medium (glass)	Small (glass)	Small (air)
original	0.80	0.88	0.92	0.93	0.91
field map	0.92	0.89	0.92	0.85	0.85
phase map	0.92	0.95	0.96	0.93	0.97

According to the results, our phase-map method achieves better performance in terms of recovering the warped geometry of the cylinders in the original phantom image. The field-map method may produce worse results because of inaccurate estimation of the distortion field. For example, after correction with the field-map method, the geometry of the small cylinder with glass rod and the small cylinder with air both become worse. Hence, these results indicate that it is important to correct the image distortion with a dynamic distortion field.

5.4. Validation of our registration method with phase-gradient constraint

We validate our registration method with phase-gradient constraint based on simulated EPI series. The imaging parameters for the simulated EPI are the same as those for the simulated EPI in the previous experiments, and were given in Section 5.1. As explained in Chapter IV, standard Cubic B-spline basis functions are employed to model the distortion field. In our experiments, we place the B-spline basis functions on a grid of every third voxel in the x and in the y direction in the foreground area of the EPI. In

Figure 34, a distortion field fitted by B-spline (left) is compared with the true distortion field (right). A profile plot of the red line in Figure 34 is shown in Figure 35. As it shows, with the modeled distortion field, the ground truth field map can be approximated fairly well.

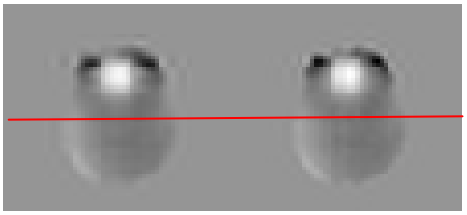

Figure 34. Distortion field fitted with B-spline. Left is the fitted distortion field. Right is the true distortion field. Basis functions are placed on foreground area of the EPI.

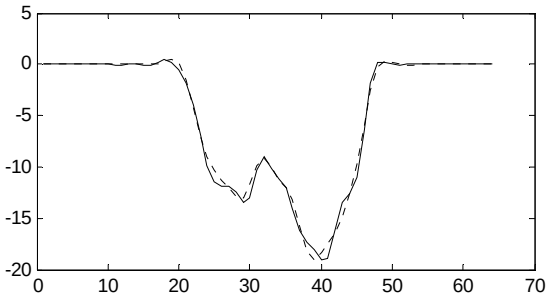

Figure 35. A profile plot of the distortion field (indicated by a red line in Figure 34). The solid line represents the true distortion field, and the dotted line represents the fitted distortion field. As it shows, the true distortion field can be approximated fairly well with the modeled distortion field.

As we discussed in Chapter IV, the phase gradients that are computed from a wrapped phase map have minimum or zero phase wrapping and are approximately proportional to the spatial gradient of the distortion field in distorted space. To verify our theory, we compute the phase-gradient maps from a simulated EPI, and the results are

shown in Figure 36. Because the distortion field is spatially smooth, the gradient maps computed from the image phase have minimum phase wrapping. From the phase-gradient maps, the spatial gradients of the distorted field in distorted space are easily calculated. Figure 36 shows (a) wrapped phase maps, (b) the gradient maps of the distortion field in vertical direction computed from the image phase, and (d) the gradient maps of the distortion field in horizontal direction computed from the image phase. As a comparison, the gradients of the distortion field in vertical direction and in horizontal direction computed from the true field map are shown in (c) and (f). The similarity between (b) and (c), (d) and (f) supports our theory.

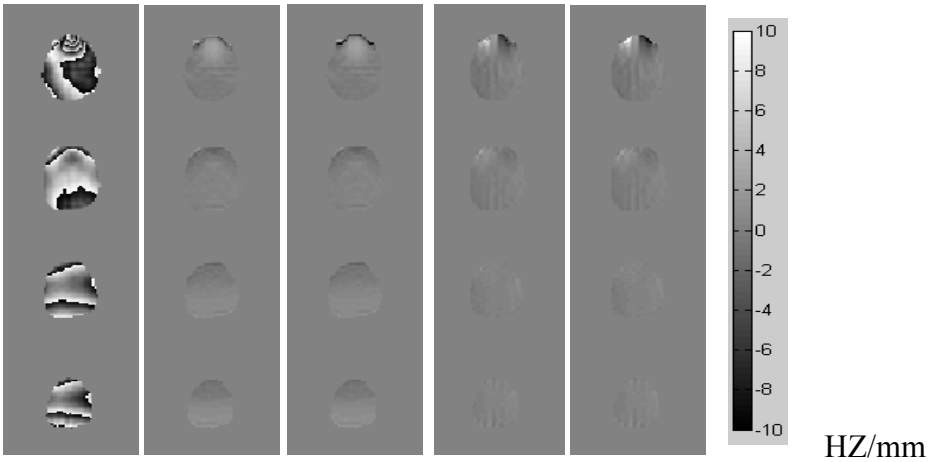

Figure 36. Computation of the gradients of a distortion field from wrapped phase. (a) is a wrapped phase map. (b) is the gradient maps of the distortion field in vertical direction computed from the phase map. (c) is the gradient maps of the distortion field in vertical direction computed from the field map directly. (d) and (e) are the gradient maps in horizontal direction computed from phase map and the field map respectively. Because distortion field tends to be smooth in space, the phase-gradient maps have minimum phase wrapping. From the phase-gradient maps, we can easily calculate the gradients of the distorted field in distorted space. The similarity between (b) and (c), (d) and (e) supports our theory.

We now investigate the effects of using the non-rigid registration method with and without phase-gradient constraint to estimate the distortion field. A distorted EPI is registered to a template EPI which was corrected with the traditional field-map method. Figure 37 shows (a) the estimated distortion field via the standard non-rigid registration method without phase-gradient constraint, (b) the estimated distortion field via our method, and (c) the true distortion field. The estimated errors found in the results from the traditional non-rigid registration (indicated by red arrows) are largely removed by integrating the phase-gradient constraint. The red line in Figure 37 is utilized in Figure 38, and the red circle is utilized in Table 2 below.

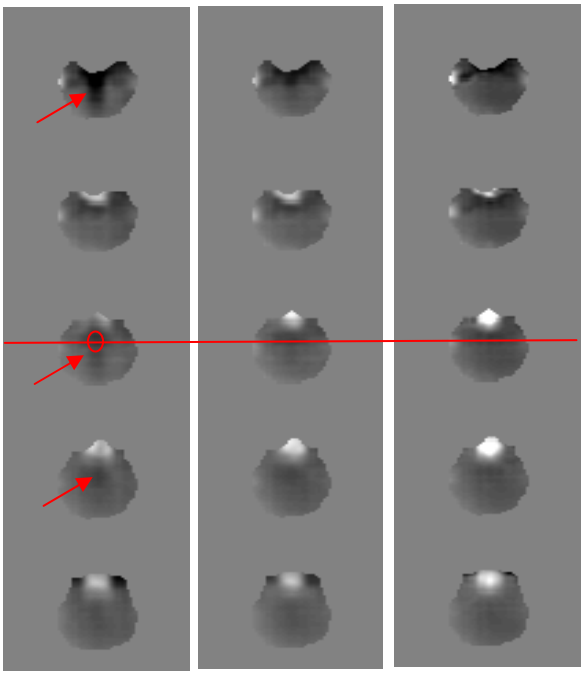

Figure 37. Estimated distortion fields based on non-rigid registration with and without our phase-gradient constraint. (a) is the estimated distortion field without the phase-gradient constraint. (b) is the estimated distortion field with the constraint. (c) is the ground-truth distortion field. With the phase-gradient constraints, the estimation errors are largely reduced. Particularly at the areas pointed at by the arrows. (The circle is referred to in Table 2.)

In the standard non-rigid registration method, the distortion field is estimated based on matching image intensity patterns. The distorted EPI is warped to a corrected EPI. However, the resulting estimated distortion field could be false because it relies only on the intensity patterns. With the incorporation of our phase-gradient constraint, not only the image intensity but also the phase guides the optimization process, thus the chance of getting an inaccurate distortion field is reduced.

To take a closer look at the effect of the incorporation of the phase-gradient constraint in non-rigid registration, we plot the field-map profile (indicated by a red line in Figure 37). In Figure 38, the solid line represents the ground-truth distortion field. The dashed line represents the estimated distortion field based on the standard non-rigid registration method. The dotted line represents the estimated field based on our method. As it shows, the phase-gradient enforces an effective spatial constraint on the generation of accurate distortion field in non-rigid registration method. This comes from the fact that the estimated distortion field using our method is based on an optimization framework with both phase information and intensity information. In the cost function for optimization, not only the similarity of image intensity but also the similarity of the spatial gradients of the distortion field is optimized. Thus, inaccurate estimation of the distortion field can be mitigated by using our method.

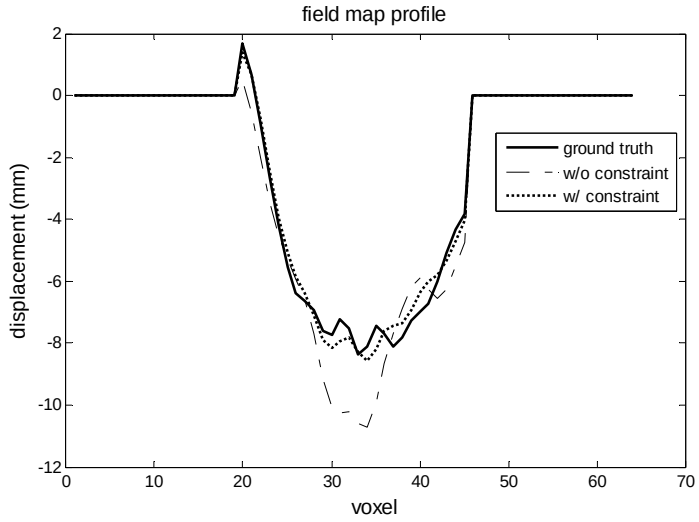

Figure 38. Estimated distortion field and ground-truth distortion field. The solid line represents the ground-truth distortion field. The dashed line is the estimated distortion field with standard non-rigid registration. The dotted line is the estimated distortion field with our phase-gradient constraint. We see that some false spatial variation of the distortion field from the standard non-rigid is suppressed by using our method.

In Figure 39, we show the spatial gradients of the estimated distortion field and those of the ground-truth distortion field. Column (a) shows the spatial gradients of the estimated distortion field based on the standard non-rigid registration method. Column (b) shows the spatial gradients based on our method with the phase-gradient constraint. Column (c) shows the real gradient maps of the distortion field. As can be seen, the spatial gradients of the estimated distortion using our method are closer to the ground truth as expected than the standard non-rigid registration. The false spatial variations of the distortion field in the standard non-rigid registration method (indicated by red arrows in (a)) are largely removed by using our method (shown in (b)). Note, not only the magnitude but also the geometry of the gradient maps should be compared because the

gradient maps are computed when the distortion field is in distorted space. The red line in this figure is utilized in Figure 40.

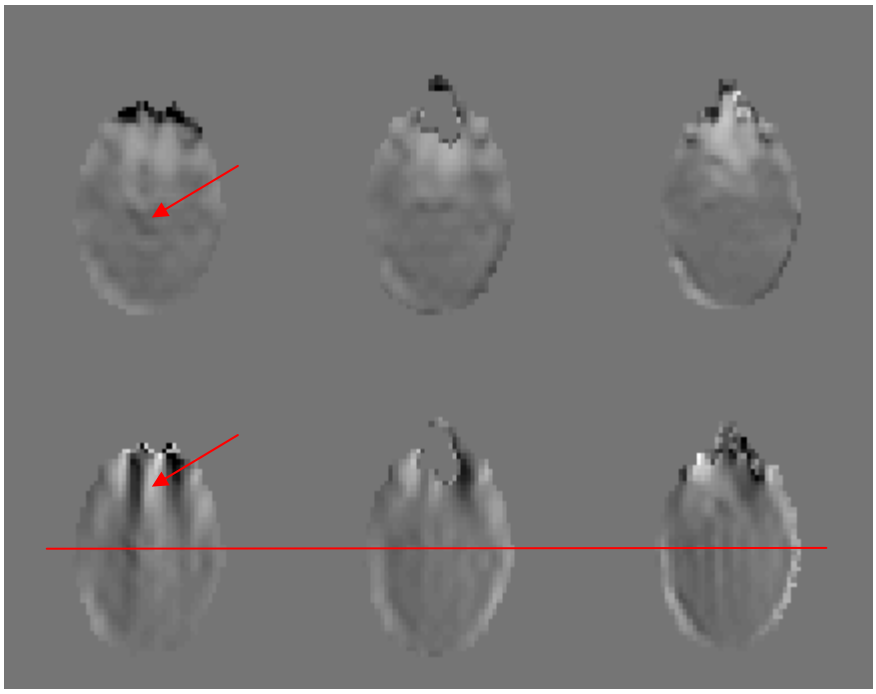

(a) **(b)** **(c)**

Figure 39. Gradient maps of the estimated distortion field and those of the ground-truth distortion field. Top rows are the gradients in the vertical direction and the bottom rows are the gradients in the horizontal direction. Column (a) shows the results from standard non-rigid registration. Column (b) shows the results from incorporating the phase-gradient constraint. Column (c) shows the ground-truth. As expected, our method generates gradient maps that are closer to ground truth in terms of both magnitude and geometric pattern. The false spatial variations of the distortion field in the standard non-rigid registration method (indicated by red arrows in (a)) are largely removed by using our method shown in (b).

A profile plot of the spatial gradient of the distortion fields (indicated by a red line in Figure 39) is shown in Figure 40. The solid line presents the ground truth. The dashed line represents the gradient maps from the results of the standard non-rigid registration. The dotted line represents the results from our method. As it shows, the false spatial

gradients of the estimated distortion field can be suppressed by integrating the phase information.

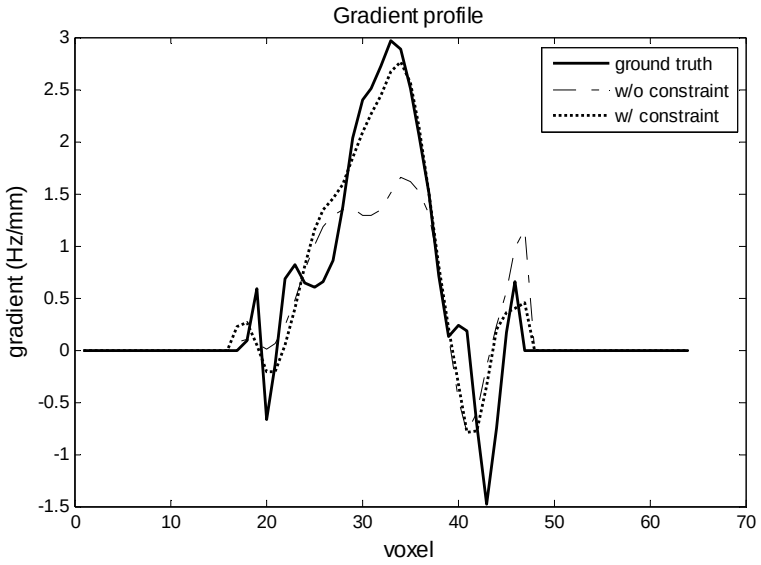

Figure 40. Gradient profile (indicated by a red line in Figure 39). The solid line is the true gradient of the distortion field. The dashed line is the gradient from the estimated distortion with standard non-rigid registration. The dotted line is the gradient from the estimated distortion field with the phase-gradient constraint. As it shows, the gradients of the distortion field computed with the new constraint is closer to that of the ground truth than the standard non-rigid registration without phase information.

To further quantify the effect of incorporating the phase-gradient constraint into the standard non-rigid registration, we compute the RMS errors of the estimated distortion field in a region of interest (indicated by a red circle in Figure 37) at different time points in an EPI time series. The results are summarized in Table 2. As it shows, the integration of the phase-gradient constraint can reduce the estimate errors.

Table 2 RMS error of the estimated field in a ROI (mm)

Time point	1	2	3	4	5	6
No phase-gradient	3.06	3.3	3.60	3.10	3.81	1.52
With phase-gradient	0.83	0.55	0.88	0.45	1.02	0.27

5.5. Comparison of strategies for estimation of ΔB_S

In this experiment, we compare six strategies for the estimation of dynamic distortion fields of a simulated EPI series in the presence of motion and a varying distortion field. The imaging parameters and the out-of-plane motion sequence for the simulated EPIs are the same as those used in Section 5.4. We chose two EPIs from the original time series for evaluation including a template EPI (the first EPI of the series) and a source EPI (an EPI from a selected time point).

Our first strategy is as follows: First, we perform a motion compensation between the source and the template by rigidly transforming the original template to the original source. Then we correct the template EPI using the field-map method. We rigidly transformed the corrected template EPI according the estimated motion parameters. Then we estimate the distortion field for the source EPI ΔB_S by warping the source EPI to the corrected and rigidly transformed template based on standard non-rigid registration. We will call this strategy "intensity method".

In the second strategy, we correct both the source EPI and the template EPI with a single field map. Then we perform a motion compensation based on the corrected EPIs. Then, we estimate ΔB_S based on standard non-rigid registration. We use the field map for the template image (ΔB_T) as an initial estimation of the distortion field for each non-rigid registration to reduce the convergence time. We call this strategy "field correction & intensity method".

The third strategy is similar to the second one except that we correct the source EPI with an estimated field based on our phase-map method (ΔB_{S0}) instead of using the same field map used for the template image. Then we apply standard non-rigid

registration to re-optimize the distortion field ΔB_S. We also use ΔB_{S0} as an initial estimation of the non-rigid registration to reduce the convergence time. We call this strategy "phase correction & intensity method".

The fourth strategy follows the same steps as the third strategy. In the last step, however, we incorporate the phase-gradient constraint into the non-rigid registration method. This strategy is called "phase correction & intensity method with phase constraint".

All these four methods give an estimation of the distortion field for each source EPI ΔB_S with the help of non-rigid registration. We compare the estimation results from these four methods, an approximation of the distortion field based on a static field map (ΔB_T), and the distortion field computed from our phase-map method directly (ΔB_{S0}). Four regions of interests in the EPI are chosen. The RMS errors in different regions of interest are computed for all these methods. The results are summarized in Figure 41.

Among these six strategies, the intensity method, the field correction & intensity method, and the field-map method give the largest errors. Phase correction & intensity method produce fewer estimation errors than these three methods. The two methods—phase correction & intensity method with phase-gradient constraint and the phase-map methods—achieve the best performance among all these six strategies. Based on these results, we reach these conclusions: (a) motion compensation should be performed on EPI series only after they have been corrected for distortion. (b) Each EPI should be corrected with its own distortion field. (c) A standard registration method alone may generate relatively large estimation errors. (d) The incorporation of the phase-gradient constraint imposes an effective spatial constraint on standard non-rigid registration.

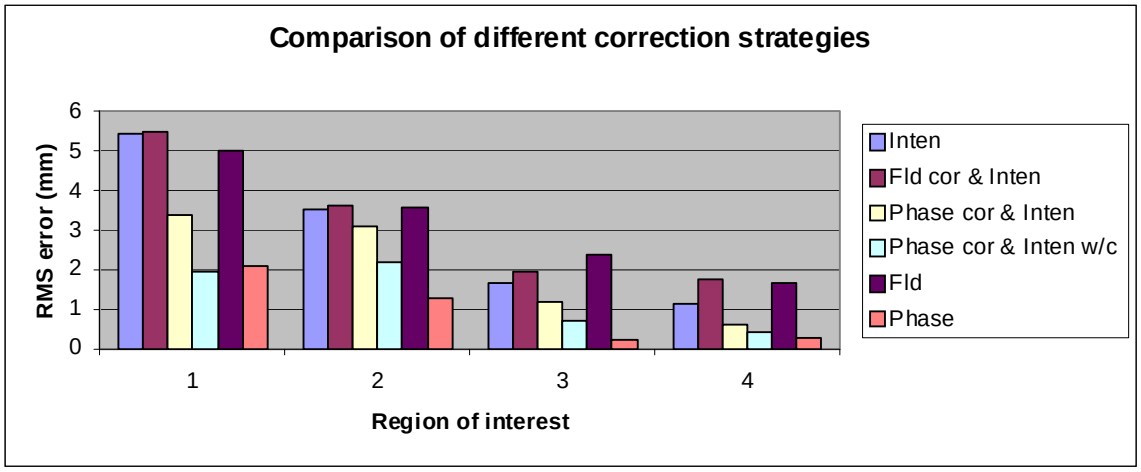

Figure 41. A comparison of different strategies. The phase-map method and the phase correction & intensity method with phase-gradient constraint are the best two among all strategies.

It is not surprising that non-rigid registration would not generate an estimated field as accurate as the phase-map method in which the distortion field is known for each voxel. However, the utilization of non-rigid registration could still be helpful in practice. For example, if the temporal variation of the distortion field is dramatic, then the phase unwrapping algorithm in our phase-map method may fail in those areas, as has already been demonstrated in Figure 22. A subsequent correction based on an erroneous distortion field from the phase-map method could potentially introduce artifacts into the corrected image. Moreover, if large motion exists in a time series, then our phase-map method may produce large estimation errors primarily near the image edge of foreground areas because of the lack of phase information in these areas. These problems can be mitigated by further applying our non-rigid registration method with both phase and intensity information. In Figure 42, the estimation errors of the distortion field in the phase-map method caused by temporal phase wrapping are reduced by means of a non-

rigid registration method with both phase and intensity information. The top panel of Figure 42 shows (a) the estimated distortion field with our phase-map method, (b) the estimated distortion field when the phase-map method is followed by our non-rigid registration with phase-gradient constraint, and (c) the ground-truth distortion field respectively. Bottom panel: (a) and (b) are the results of subtracting the magnitude of the distortion-free image from the magnitudes of the EPI corrected with the phase-map and the EPI corrected with our registration method and (c) is the distortion-free image. As can be seen, the temporal phase wrapping causes artifacts in the corrected image. These errors are reduced by a subsequent registration method with both phase and intensity information.

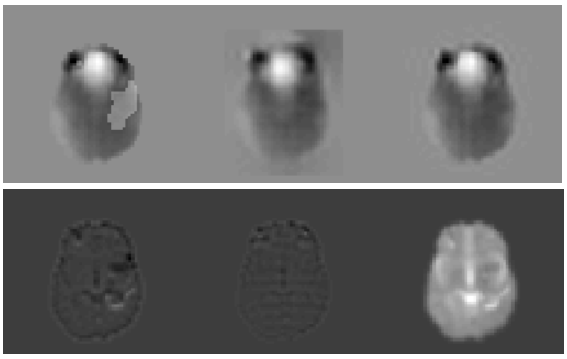

(a) (b) (c)

Figure 42. Temporal phase wrapping remedied via registration. Top panel: (a) is the estimated distortion field with the phase-map method, (b) is the estimated distortion field via our registration method incorporating both phase and intensity information, and (c) is the ground-truth distortion field. Bottom panel: (a) and (b) are the results of subtracting the magnitude of the distortion-free image from the magnitudes of the EPI corrected with the phase-map and the EPI corrected with our registration method and (c) is the distortion-free image. We can see that the estimation error caused by temporal phase wrapping, which is clearly visible in (a), is removed in (b).

There is another aspect in which our registration method could potentially reduce the estimation errors. According to the theory we presented in Chapter III, there is a fundamental assumption for the distortion correction to succeed. The original undistorted

EPI and the distorted EPI should have one-to-one correspondence in image space, which makes the distortion reversible and thus correctable. This assumption is violated in regions where the distortion field changes abruptly in space. In those areas, the image tissues can be squeezed so dramatically that folding can occur. In such regions, a correction based on the phase-map method can introduce severe artifacts in the corrected EPI as shown in Figure 43. The top panel of Figure 43 shows (a) the estimated distortion field with the phase-map method, (b) the estimated distortion field via the registration method with both phase and intensity, and (c) the ground-truth distortion field respectively. The bottom panel of Figure 43 (from left to right) shows the corrected images with the corresponding distortion fields. These artifacts can be reduced in our registration method, in which the distortion field is modeled as a smooth function, and, as a result, a better approximate solution can be produced when folding occurs than that produced by the phase-map method alone. This improvement is the result of the required smoothness of the distortion field and the least-squares solution, both of which limit the propagation of the effect in areas remote from the fold. We can see fewer artifacts in the corrected images with registration method.

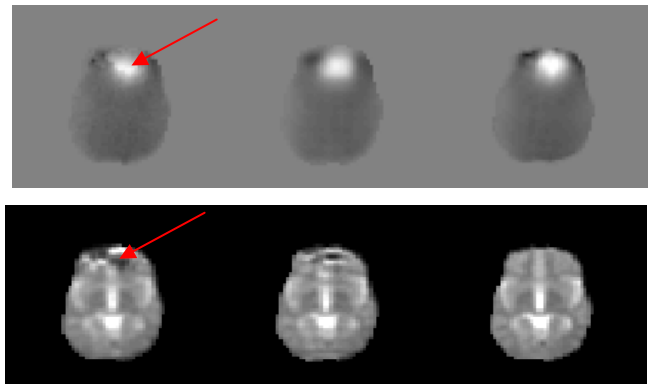

(a) **(b)** **(c)**

Figure 43. Phase-map method versus registration method. The top panel shows (a) the estimated field with the phase-map method, (b) the registration method with both phase and intensity, and (c) the ground-truth distortion field respectively. The bottom panel (from left to right) shows the corrected images with the corresponding distortion fields. In regions where the distortion field changes abruptly in space, the distortion correction as an inverse problem is ill-conditioned. Here registration is superior to the phase-map method.

5.6. Conclusion

In this chapter, we have validated two methods for the estimation of dynamic distortion fields in EPI series. One is the phase-map method. The other one is registration with phase-gradient constraint. The theory associated with these two methods has been presented in Chapter III and Chapter IV. We focused on the validation and evaluation of these two methods in this chapter.

We employed two types of image data for validation. One is a simulated EPI series with realistic motion and a varying distortion field. The other one is real EPI acquisitions of a physical phantom with a geometrical design. Based on the experimental results, our phase-map method properly estimated the dynamic distortion in EPI time series caused by external sources such as respiration and bulk motion, indicating that the

application of our phase-map method can recover the temporal variation of distortion fields. We found that a correction based on our "phase-map" method which estimates a dynamic field is superior to the traditional field-map method in which only a static distortion field is available. The correction of an EPI series based on our phase-map method can reduce the intensity variation caused by dynamic image distortion, which is important for temporal analysis of a series of EPIs.

Image registration, as an important intensity method, has been applied by others to correct the EPI distortion. Based on our simulation, the accuracy of using image registration for estimation of dynamic distortion fields depends on two factors. First, proper motion compensation is critical. Second, an effective constraint on the distortion field is necessary. In this chapter, we validated the theory we presented in Chapter IV based on simulated EPI series. Motion compensation on the corrected EPI series with our phase-map method was found in our experiments to be more accurate than that motion compensation based on either the original EPI series or the EPI series corrected with the traditional field-map method. We also showed that the spatial gradients of the distortion fields can be computed accurately from the image phase and that these gradients impose an effective spatial constraint on the estimation of dynamic distortion fields. We also demonstrated that our registration method with phase-gradient constraint can achieve an accuracy equal to that of our phase-map method in most areas. In addition, the artifacts in the corrected EPI caused by temporal phase wrapping and abrupt spatial variation of the distortion field in the phase-map method can be reduced via our registration method because of the incorporation of intensity information with phase information.

CHAPTER VI

CONCLUSION AND FUTURE WORK

6.1. Conclusion

In this dissertation, we have studied the correction of dynamic image distortion in EPI time series. Two retrospective methods were proposed and tested to achieve this goal. Our methods rely on the well established facts that the dynamic distortion fields are encoded in the image phase from the EPI and that the temporal variation and the spatial variation of the distortion fields are proportional to the temporal variation and the spatial variation of the image phase, respectively. We showed how to take advantage of these facts by overcoming problems of low signal-to-noise ratios and non-overlapping foregrounds by means of an extended regularization approach and combining phase information with intensity information through constrained non-rigid registration. Quantitative validation and evaluation of the proposed methods were performed based both on simulated EPI data and on real EPI data of a physical phantom. Results showed that our methods are superior to the traditional distortion-correction methods with regard to the specific problem of reducing the temporal intensity variation of an EPI series caused by dynamic image distortion.

In Chapter III, we described our "phase-map" method. Based on MR physics, our phase-map method takes advantage of the fact that the temporal variation of the distortion field in an EPI series is encoded in the temporal phase variation. If the variation of the distortion field is sufficiently slow in time, then the phase changes induced by them will be immune to phase wrapping. We looked into the temporal phase evolution of the EPI,

from which the variation of the distortion field was computed. In our method, the phase information of the EPI, in conjunction with one extra EPI reference-image, was used to compute a separate distortion field at each time point. It is well known that EPI phase is notorious noisy. To suppress the effects of noise in the field calculation, we proposed a regularization method for phase calculation. Regularized distortion fields were estimated by using both image phase and image intensity based on maximum likelihood. An application of the regularized distortion fields in distortion-correction helped to reduce artifacts in the corrected images. Because the estimated distortion fields from EPI are geometrically distorted in the same way as the EPI itself, a forward correction was employed for distortion correction. The dynamic image distortion in an EPI series can then be corrected directly with the dynamic distortion fields.

The employment of image registration in motion compensation and distortion correction of EPI series was studied in Chapter IV. We found that the utilization of standard non-rigid registration in correction of dynamic image distortion is limited in that it depends on accurate motion compensation and effective constraint on the distortion field. We suggested a new strategy for motion compensation, in which the motion compensation was performed on the corrected EPIs with our phase-map method. The correction of EPI using a non-rigid registration method is prone to a suboptimal local minimum because a large number of degrees of freedom must be optimized to represent the distortion field. Furthermore, the traditional optimization methods rely entirely on the image differences in intensity patterns between a distorted EPI and a template EPI. To overcome these limitations, we proposed to incorporate the spatial gradient of the distortion field into the non-rigid registration framework. We use the gradient of the

distortion field, computed from the image phase, which we call the "phase gradient" to impose a time-dependent spatial constraint on the distortion field. In this new method, a novel cost function is presented, which depends not only on the similarity of the image intensity patterns but also on the similarity of the gradients of the distortion fields. Compared with standard non-rigid registration, the problem of the suboptimum local minimum in correction of EPI is mitigated by this use of phase information. The application of our phase-map method followed by our registration method, driven by both phase and intensity patterns, achieves a more accurate estimation of the dynamic distortion field in EPI series than traditional methods.

The validation and evaluation of our proposed methods was carried out in Chapter V. A simulated EPI series with realistic motion and a varying distortion field were utilized to generate dynamic image distortion and motion effects. We applied our methods to the simulated EPI series, and performed quantitative evaluation to compare the results from our methods to the known ground truth. The effects of using our methods on the reduction of the temporal intensity variation in EPI series were quantified. Improvements over current approaches were shown by comparing our method with the traditional field-map method and the standard non-rigid registration method. We also validated our methods based on real EPI of a physical phantom. We carefully designed our phantom to create both a spatial variation and a temporal variation of the distortion field. We obtained the ground-truth distortion field by acquiring extra scans. The results of our method were analyzed by means of an evaluation of the estimated distortion field and an evaluation of the corrected EPI. We compared several strategies for estimation of

dynamic distortion fields based on simulated EPI series in the presence of motion and dynamic distortion fields.

6.2. Future work

We developed a phase-map method for the generation of dynamic distortion fields in EPI series. In our derivation, we ignored the effects of the phase errors induced by sources other than the static field inhomogeneity. It was assumed that all the excited spins would be in phase after the 90^0 RF pulse is turned off. The phase evolution of each spin will be affected only by the imaging gradients and static field inhomogeneity. However, the phase errors coming from B_1 field inhomogeneity could have an impact. If the spatial variation of these phase errors is large, they can cause errors when we compute the temporal phase difference. This did not appear to be a problem when we tested our algorithm using real EPI data. However, a study of the magnitude of both the spatial and the temporal distribution of these phase errors could be helpful to increase the robustness of our phase-map method. In fact, if the magnitude of the spatial distribution of these phase errors has a negligible effect, then our phase-map method could be further improved. As we have shown, the temporal phase variation between adjacent EPI volumes cannot be determined in some physical locations when there is sufficiently large motion. This might be improved by the following method. First, the motion of adjacent EPI volumes could be corrected based on an estimation of their relative motion by registering their magnitude images. The overlapping regions of the aligned volumes would be increased. We could then compute the temporal phase difference from the aligned phase volumes. With an estimation of the dynamic distortion fields, each EPI

could be corrected with a separate distortion field. Improved motion compensation could be then recalculated. Iteratively repeating this process, we might achieve a more accurate estimation of the distortion fields. By using the image intensity and the image phase, the motion compensation and the estimation of the distortion field might be improved alternatively.

As we can see from Eqn. (34), our method utilizes the phase information of a reference image acquired at the beginning of the time series to calculate the dynamic distortion field for all other time points. It is expected that noise will be accumulated in our iterative calculation. One solution to this problem is to divide a time series into several sections and acquire a separate reference image at the beginning of each section. In this case, the effect of noise accumulation could be reduced and the temporal resolution of the study will be minor because we are dealing with an EPI time series including hundreds of volumes.

The study of the distribution of phase errors could also be useful for the registration method we developed in Chapter IV. In our method, we incorporated a phase-gradient constraint into the image-registration framework. The phase gradients characterize the spatial gradients of the distortion field. This also depends on the assumption either that the phase errors are small or that they do not have a spatial distribution pattern that is comparable to that induced by the distortion field. Fortunately, our method is based on both image intensity and image phase. The effect of the phase errors is expected to be small. However, it will still be an interesting topic to study the spatial distribution of the phase errors. A pre-processing on the image phase could be useful.

We proposed a phase-map regularization approach in Chapter III, in which the noise in the phase of EPI is assumed to have a Gaussian distribution. It may not be accurate, however, because when each channel of the complex EPI signal is corrupted individually by Gaussian noise, the noise distribution in the phase is more complicated than a simple Gaussian. In future work, the study of the noise distribution of the image phase may be useful to develop a more accurate regularization approach than the current one.

In Chapter IV, we incorporated a phase-gradient constraint into the image-registration framework. We expected that the estimation errors from our phase-map method could be reduced via an image registration method with both phase and intensity information. However, a non-rigid registration is typically very costly. While calculation of a distortion field for an image volume based on our phase-map method takes less than a minute, a subsequent non-rigid registration implemented takes about 20 minutes of computation time on a PC with a 3G Hz CPU and 1GB of RAM using Matlab (The Mathworks, Natick, MA). In fact, the estimated distortion field from our phase-map method is quite close to ground truth, and substantial estimation errors occur only near the edges of foreground areas and near the sinuses. Even errors coming from temporal phase wrapping could be easily identified. Hence, it is not optimum to re-estimate the distortion field for the whole image volume. If the re-optimization of the distortion field is performed only in those problem areas, the computation time could be dramatically reduced.

We can also apply the registration method we developed in Chapter IV to correct EPI for functional localization. Presumably, the registration of an EPI with an anatomical

image is more difficult than registering two EPIs because the EPI and the anatomical image have different contrast, image quality, and resolution. In this application, an integration of the spatial constraint on the distortion field computed from image phase could be quite useful. This will be an interesting topic.

The validation of our methods was performed based on simulated EPI series and real EPI data of a physical phantom. In the future it is hoped that the application of our methods can be extended to clinical applications such as fMRI .

REFERENCES

1. Hutchinson, M. and Raff, U., Fast Mri Data Acquisition Using Multiple Detectors, Magnetic Resonance in Medicine, 6 (1988) 87-91.

2. Mukherjee, P., Bahn, M.M., McKinstry, R.C., Shimony, J.S., Cull, T.S., Akbudak, E., Snyder, A.Z., and Conturo, T.E., Differences between gray matter and white matter water diffusion in stroke: diffusion-tensor MR imaging in 12 patients, Radiology, 215 (2000) 211-220.

3. Fenyes, D.A. and Narayana, P.A., In vivo diffusion tensor imaging of rat spinal cord with echo planar imaging, Magnetic Resonance in Medicine, 42 (1999) 300-306.

4. Werring, D.J., Toosy, A.T., Clark, C.A., Parker, G.J., Barker, G.J., Miller, D.H., and Thompson, A.J., Diffusion tensor imaging can detect and quantify corticospinal tract degeneration after stroke, J Neurol Neurosurg Psychiatry, 69 (2000) 269-272.

5. Bammer, R., Auer, M., Keeling, S.L., Augustin, M., Stables, L.A., Prokesch, R.W., Stollberger, R., Moseley, M.E., and Fazekas, F., Diffusion tensor imaging using single-shot SENSE-EPI, Magnetic Resonance in Medicine, 48 (2002) 128-136.

6. Kwong, K.K., Chesler, D.A., Weisskoff, R.M., Donahue, K.M., Davis, T.L., Ostergaard, L., Campbell, T.A., and Rosen, B.R., MR Perfusion Studies with T-1-Weighted Echo-Planar Imaging, Magnetic Resonance in Medicine, 34 (1995) 878-887.

7. Schwitter, J., Debatin, J.F., von Schulthess, G.K., and McKinnon, G.C., Normal myocardial perfusion assessed with multishot echo-planar imaging, Magnetic Resonance in Medicine, 37 (1997) 140-147.

8. Poncelet, B.P., Koelling, T.M., Schmidt, C.J., Kwong, K.K., Reese, T.G., Ledden, P., Kantor, H.L., Brady, T.J., and Weisskoff, R.M., Measurement of human myocardial perfusion by double-gated flow alternating inversion recovery EPI, Magnetic Resonance in Medicine, 41 (1999) 510-519.

9. Yamada, K., Gonzalez, R.G., Ostergaard, L., Komili, S., Weisskoff, R.M., Rosen, B.R., Koroshetz, W.J., Nishimura, T., and Sorensen, A.G., Iron-induced susceptibility effect at the globus pallidus causes underestimation of flow and volume on dynamic susceptibility contrast-enhanced MR perfusion images, American Journal of Neuroradiology, 23 (2002) 1022-1029.

10. Ye, F.Q., Pekar, J.J., Jezzard, P., Duyn, J., Frank, J.A., and McLaughlin, A.C., Perfusion imaging of the human brain at 1.5 T using a single-shot EPI spin tagging approach, Magnetic Resonance in Medicine, 36 (1996) 217-224.

11. Reeder, S.B., Atalar, E., Faranesh, A.Z., and McVeigh, E.R., Referenceless interleaved echo-planar imaging, Magnetic Resonance in Medicine, 41 (1999) 87-94.

12. Sekihara, K., Kuroda, M., and Kohno, H., Image restoration from non-uniform magnetic field influence for direct Fourier NMR imaging, PMB, 29 (1984) 15-24.

13. Chang, H. and Fitzpatrick, J.M., A Technique for Accurate Magnetic-Resonance-Imaging in the Presence of Field Inhomogeneities, Ieee Transactions on Medical Imaging, 11 (1992) 319-329.

14. Noll, D.C., Meyer, C.H., Pauly, J.M., Nishimura D.G., and Macovski A., A Homogeneity Correction Method for Magnetic Resonance Imaging with Time-Varying Gradients, Ieee Transactions on Medical Imaging, 10 (1991) 629-637.

15. Jezzard, P. and Balaban, R.S., Correction for Geometric Distortion in Echo-Planar Images from B-0 Field Variations, Magnetic Resonance in Medicine, 34 (1995) 65-73.

16. Andersson, J.L.R., Hutton, C., Ashburner, J., Turner, R., and Friston, K., Modeling geometric deformations in EPI time series, Neuroimage, 13 (2001) 903-919.

17. Jezzard, P. and Clare, S., Sources of distortion in functional MRI data, Human Brain Mapping, 8 (1999) 80-85.

18. Howseman, A.M. and Bowtell, R.W., Functional magnetic resonance imaging: imaging techniques and contrast mechanisms, Philos. Trans. R. Soc. Lond B Biol. Sci., 354 (1999) 1179-1194.

19. Ogawa, S., Menon, R.S., Tank, D.W., Kim, S.G., Merkle, H., Ellermann, J.M., and Ugurbil, K., Functional brain mapping by blood oxygenation level-dependent contrast magnetic resonance imaging. A comparison of signal characteristics with a biophysical model, Biophys. J., 64 (1993) 803-812.

20. Bandettini, P.A., Wong, E.C., Jesmanowicz, A., Hinks, R.S., and Hyde, J.S., Spin-echo and gradient-echo EPI of human brain activation using BOLD contrast: a comparative study at 1.5 T, NMR Biomed., 7 (1994) 12-20.

21. Cordes, D., Turski, P.A., and Sorenson, J.A., Compensation of susceptibility-induced signal loss in echo-planar imaging for functional applications, Magnetic Resonance Imaging, 18 (2000) 1055-1068.

22. Stroman, P.W., Krause, V., Frankenstein, U.N., Malisza, K.L., and Tomanek, B., Spin-echo versus gradient-echo fMRI with short echo times, Magnetic Resonance Imaging, 19 (2001) 827-831.

23. Yoder, D.A., Zhao, Y.S., Paschal, C.B., and Fitzpatrick, J.M., MRI simulator with object-specific field map calculations, Magnetic Resonance Imaging, 22 (2004) 315-328.

24. Schmithorst, V.J., Dardzinski, B.J., and Holland, S.K., Simultaneous correction of ghost and geometric distortion artifacts in EPI using a multiecho reference scan, Ieee Transactions on Medical Imaging, 20 (2001) 535-539.

25. Ojemann, J.G., Akbudak, E., Snyder, A.Z., McKinstry, R.C., Raichle, M.E., and Conturo, T.E., Anatomic localization and quantitative analysis of gradient refocused echo-planar fMRI susceptibility artifacts, Neuroimage, 6 (1997) 156-167.

26. Field, A.S., Yen, Y.F., Burdette, J.H., and Elster, A.D., False cerebral activation on BOLD functional MR images: study of low-amplitude motion weakly correlated to stimulus, AJNR Am. J. Neuroradiol., 21 (2000) 1388-1396.

27. Ardekani, B.A., Bachman, A.H., and Helpern, J.A., A quantitative comparison of motion detection algorithms in fMRI, Magnetic Resonance Imaging, 19 (2001) 959-963.

28. Carpenter, P.A., Just, M.A., Keller, T.A., Eddy, W.F., and Thulborn, K.R., Time course of fMRI-activation in language and spatial networks during sentence comprehension, Neuroimage, 10 (1999) 216-224.

29. Gorno-Tempini, M.L., Hutton, C., Josephs, O., Diechmann, R., Price, C., and Turner, R., Echo time dependence of BOLD contrast and susceptibility artifacts, NeuroImage, 15 (2002) 136-42.

30. Callicott, J.H., Ramsey, N.F., Tallent, K., Bertolino, A., Knable, M.B., Coppola, R., Goldberg, T., van Gelderen, P., Mattay, V.S., Frank, J.A., Moonen, C.T., and Weinberger, D.R., Functional magnetic resonance imaging brain mapping in psychiatry: methodological issues illustrated in a study of working memory in schizophrenia, Neuropsychopharmacology, 18 (1998) 186-196.

31. Henkin, R.I. and Levy, L.M., Functional MRI of congenital hyposmia: brain activation to odors and imagination of odors and tastes, J. Comput. Assist. Tomogr., 26 (2002) 39-61.

32. Wilson, M., Tench, C.R., Morgan, P.S., and Blumhardt, L.D., Pyramidal tract mapping by diffusion tensor magnetic resonance imaging in multiple sclerosis: improving correlations with disability, Journal of Neurology Neurosurgery and Psychiatry, 74 (2003) 203-207.

33. Reeder, S.B., Atalar, E., Faranesh, A.Z., and McVeigh, E.R., Multi-echo segmented k-space imaging: An optimized hybrid sequence for ultrafast cardiac imaging, Magnetic Resonance in Medicine, 41 (1999) 375-385.

34. Raj, D., Anderson, A.W., and Gore, J.C., Respiratory effects in human functional magnetic resonance imaging due to bulk susceptibility changes, Phys. Med Biol., 46 (2001) 3331-3340.

35. Sekihara, K., Matsui, S., and Kohno, H., A New Method of Measuring Static-Field Distribution Using Modified Fourier Nmr Imaging, Journal of Physics E-Scientific Instruments, 18 (1985) 224-227.

36. Sumanaweera, T.S., Glover, G.H., Binford, T.O., and Adler, J.R., Mr Susceptibility Misregistration Correction, Ieee Transactions on Medical Imaging, 12 (1993) 251-259.

37. Kadah, Y.M. and Hu, X.P., Algebraic reconstruction for magnetic resonance imaging under B-0 inhomogeneity, Ieee Transactions on Medical Imaging, 17 (1998) 362-370.

38. Munger, P., Crelier, G.R., Peters, T.M., and Pike, G.B., An inverse problem approach to the correction of distortion in EPI images, Ieee Transactions on Medical Imaging, 19 (2000) 681-689.

39. Reber, P.J., Wong, E.C., Buxton, R.B., and Frank, L.R., Correction of off resonance-related distortion in echo-planar imaging using EPI-based field maps, Magnetic Resonance in Medicine, 39 (1998) 328-330.

40. Wan, X., Gullberg, G.T., Parker, D.L., and Zeng, G.L., Reduction of geometric and intensity distortions in echo-planar imaging using a multireference scan, Magnetic Resonance in Medicine, 37 (1997) 932-942.

41. Chen, N.K. and Wyrwicz, A.M., Correction for EPI distortions using multi-echo gradient-echo imaging, Magnetic Resonance in Medicine, 41 (1999) 1206-1213.

42. Chen, N.K. and Wyrwicz, A.M., Optimized distortion correction technique for echo planar imaging, Magnetic Resonance in Medicine, 45 (2001) 525-528.

43. Chiou, J.Y., Ahn, C.B., Muftuler, L.T., and Nalcioglu, O., A simple simultaneous geometric and intensity correction method for echo-planar imaging by EPI-based phase modulation, Ieee Transactions on Medical Imaging, 22 (2003) 200-205.

44. Zeng, H., Gatenby, J.C., Zhao, Y., and Gore, J.C., New approach for correcting distortions in echo planar imaging, Magnetic Resonance in Medicine, 52 (2004) 1373-1378.

45. Robson, M.D., Gore, J.C., and Constable, R.T., Measurement of the point spread function in MRI using constant time imaging, Magnetic Resonance in Medicine, 38 (1997) 733-740.

46. Zeng, H. and Constable, R.T., Image distortion correction in EPI: Comparison of field mapping with point spread function mapping, Magnetic Resonance in Medicine, 48 (2002) 137-146.

47. Zaitsev, M., Hennig, J., and Speck, O., Point spread function mapping with parallel imaging techniques and high acceleration factors: Fast, robust, and flexible method for echo-planar imaging distortion correction, Magnetic Resonance in Medicine, 52 (2004) 1156-1166.

48. Studholme, C., Constable, R.T., and Duncan, J.S., Accurate Alignment of Functional EPI Data to Anatomical MRI Using a Physics-Based Distortion Model, Ieee Transactions on Medical Imaging, 19 (2000) 1115-1127.

49. Kybic, J., Thevenaz, P., Nirkko, A., and Unser, M., Unwarping of unidirectionally distorted EPI images, Ieee Transactions on Medical Imaging, 19 (2000) 80-93.

50. Li, Y., Xu, N., Fitzpatrick, J.M., Morgan, V.L., Pickens, D.R., and Dawant, B.M., Field map constrained nonrigid registration method for correction of distortions in EP images, Proc 14th Int. Soc. Mag. Reson. Med, (2006) 743.

51. Morrell, G. and Spielman, D., Dynamic shimming for multi-slice magnetic resonance imaging, Magn Reson. Med, 38 (1997) 477-483.

52. Chen, N., Li, L., and Wyrwicz, A.M., Optimized phase preparation and auto-shimming technique for gradient-echo imaging, Proceedings of the SMRM, 5th Annual Meeting, Sydney, (1998) 127.

53. Gruetter, R., Rothman, D.L., and Novotny, E.J., fast, non-iterative shimming on spatially localized signals: In vivo analysis of the magnetic field along axes, J. Magn. Reson., 96 (1992).

54. Maudsley, A.A., Simon, H.E., and Hilal, S.K., Magnetic field measurement by NMR imaging, J. Phys. E: Sci. Instrum., 17 (1984) 216-220.

55. Tropp, J., Derby, K.A., Hawryszko, C., Sugiura, S., and Yamagata, H., Automated shimming of Bo for spectroscopic imaging, Journal of Magnetic Resonance, 85 (1989) 244-254.

56. Schneider, E. and Glover, G., Rapid in vivo proton shimming, Magn. Reson. Med., 18 (1991) 335-347.

57. Webb, P. and Macovski, A., Rapid, fully automatic, arbitrary-volume in vivo shimming, Magnetic Resonance in Medicine, 20 (1991) 113-122.

58. Prammer, M.G., Haselgrove, J.C., Shinnar, M., and Leigh, J.S., A new approach to automatic shimming, Journal of Magnetic Resonance, 77 (1988) 40-52.

59. Kanayama, S., Kuhara, S., and Satoh, K., In vivo rapid magnetic field measurement and shimming using single scan differential phase mapping, Magnetic Resonance in Medicine, 36 (1996) 637-642.

60. Chang, H. and Fitzpatrick, J.M., Geometric image transformation to compensate for MRI distortions, Proc. SPIE, Medical Imaging, 1233 (1990) 116-127.

61. Morgan, P.S., Bowtell, R.W., McIntyre, D.J.O., and Worthington, B.S., Correction of spatial distortion in EPI due to inhomogeneous static magnetic fields using the reversed gradient method, Journal of Magnetic Resonance Imaging, 19 (2004) 499-507.

62. Bowtell, R.W., McIntyre, M.C., Commandre, M.J., Glover, P.M., and Mansfield, P., Correction of geometric distortion in echo planar images, Proceedings of the Society of Magnetic Resonance, 2nd meeting, San Francisco, CA, (1994).

63. Reinsberg, S.A., Doran, S.J., Charles-Edwards, E.M., and Leach, M.O., A complete distortion correction for MR images: II. Rectification of static-field inhomogeneities by similarity-based profile mapping, Physics in Medicine and Biology, 50 (2005) 2651-2661.

64. Kannengiesser, S.A.R., Wang, Y., and Haacke, E.M., Geometric distortion correction in gradient-echo imaging by use of dynamic time warping, Magnetic Resonance in Medicine, 42 (1999) 585-590.

65. Skare, S. and Andersson, J.L., Correction of MR image distortions induced by metallic objects using a 3D cubic B-spline basis set: application to stereotactic surgical planning, Magnetic Resonance in Medicine, 54 (2005) 169-181.

66. Weiskopf, N., Klose, U., Birbaumer, N., and Mathiak, K., Single-shot compensation of image distortions and BOLD contrast optimization using multi-echo EPI for real-time fMRI, Neuroimage, 24 (2005) 1068-1079.

67. Anderson, J.L. and Skare, S., Distortions in Diffusion Tensor Imaging (DTI): Putting it all together., Proc. 11th Int. Soc. Mag. Reson. Med., 1032 (2003).

68. Reinsberg, S.A., Moore, L., and Doran, S.J., Mutual Information-Based Correction of B0 Inhomogeneity, Susceptibility- and Chemical-Shift Artefacts, Proc. 11th Int. Soc. Mag. Reson. Med., 1049 (2003).

69. Morgan, P.S., Bowtell, R.W., McIntyre, D.J.O., and Worthington, B.S., Spatial distortion in MRI with application to stereotactic neurosurgery, Thesis/Dissertation, University of Nottingham, (1999).

70. Pruessmann, K.P., Weiger, M., Scheidegger, M.B., and Boesiger, P., SENSE: Sensitivity encoding for fast MRI, Magnetic Resonance in Medicine, 42 (1999) 952-962.

71. Hutton, C., Bork, A., Josephs, O., Deichmann, R., Ashburner, J., and Turner, R., Image distortion correction in fMRI: A quantitative evaluation, Neuroimage, 16 (2002) 217-240.

72. Roopchansingh, V., Cox, R.W., Jesmanowicz, A., Ward, B.D., and Hyde, J.S., Single-shot magnetic field mapping embedded in echo-planar time-course imaging, Magnetic Resonance in Medicine, 50 (2003) 839-843.

73. Ward, H.A., Riederer, S.J., and Jack, C.R., Real-time autoshimming for echo planar timecourse imaging, Magnetic Resonance in Medicine, 48 (2002) 771-780.

74. Hu, X.P. and Kim, S.G., Reduction of Signal Fluctuation in Functional Mri Using Navigator Echoes, Magnetic Resonance in Medicine, 31 (1994) 495-503.

75. Van de Moortele, P.F., Pfeuffer, J., Glover, G.H., Ugurbil, K., and Hu, X.P., Respiration-induced B-0 fluctuations and their spatial distribution in the human brain at 7 tesla, Magnetic Resonance in Medicine, 47 (2002) 888-895.

76. Barry, R.L. and Menon, R.S., Modeling and suppression of respiration-related physiological noise in echo-planar functional magnetic resonance imaging using global and one-dimensional navigator echo correction, Magnetic Resonance in Medicine, 54 (2005) 411-418.

77. Colin Studholme, R.Todd Constable, and James S.Duncan, Accurate Alignment of Functional EPI Data to Anatomical MRI Using a Physics-Based Distortion Model, IEEE Trans. Med. Imaging, 19 (2000) 1115-1127.

78. Gholipour, A., Kehtarnavaz, N., Briggs, R., Devous, M., and Gopinath, K., Brain functional localization: a survey of image registration techniques, Ieee Transactions on Medical Imaging, 26 (2007) 427-451.

79. Fitzpatrick, J.M., Hill, D.L.G., and Maurer, C.R., Image registration, *in Handbook of Medical Imaging*, M. Sonka and J.M. Fitzpatrick, Eds. Bellingham, WA: SPIE Press, vol. 2, Medical Image Processing and Analysis. In: Vol. 2 2000, pp. 447-513.

80. Fessler, J.A., Yeo, D., and Noll, D.C., Regularized fieldmap estimation in MRI, IEEE International Symposium on Biomedical Imaging(ISBI), (2006) 706-709.

81. Fessler, J.A. and Rogers, W.L., Spatial resolution properties of penalized-likelihood image reconstruction: Space-invariant tomographs, Ieee Transactions on Image Processing, 5 (1996) 1346-1358.

82. Friston, K.J., Williams, S., Howard, R., Frackowiak, R.S.J., and Turner, R., Movement-related effects in fMRI time-series, Magnetic Resonance in Medicine, 35 (1996) 346-355.

83. Xu, N., Fitzpatrick, J.M., Li, Y., Dawant, B.M., Pickens, D.R., and Morgan, V.L., Computer-generated fMRI phantoms with motion-distortion interaction, Magnetic Resonance Imaging, 25 (2007) 1376-1384.

84. Li, Y., Xu, N., Fitzpatrick, J.M., Morgan, V.L., Pickens, D.R., and Dawant, B.M., Accounting for signal loss due to dephasing in the correction of distortions in gradient-echo epi via nonrigid registration, Ieee Transactions on Medical Imaging, 26 (2007) 1698-1707.

85. Rueckert, D., Sonoda, L.I., Hayes, C., Hill, D.L., Leach, M.O., and Hawkes, D.J., Nonrigid registration using free-form deformations: application to breast MR images, Ieee Transactions on Medical Imaging, 18 (1999) 712-721.

86. Rohde, G.K., Aldroubi, A., and Dawant, B.M., The adaptive bases algorithm for intensity-based nonrigid image registration, Ieee Transactions on Medical Imaging, 22 (2003) 1470-1479.

87. Wahba,G., Spline models for observational data 1990.

88. Chui, H. and Rangarajan, A., A new point matching algorithm for non-rigid registration, Computer Vision and Image Understanding, 89 (2003) 114-141.

89. Raj, D., Paley, D.P., Anderson, A.W., Kennan, R.P., and Gore, J.C., A model for susceptibility artefacts from respiration in functional echo-planar magnetic resonance imaging, Phys. Med Biol., 45 (2000) 3809-3820.

90. Jenkinson, M., Fast, automated, N-dimensional phase-unwrapping algorithm, Magnetic Resonance in Medicine, 49 (2003) 193-197.

91. Zijdenbos, A.P. and Dawant, B.M., Morphometric analysis of whilte matter lesions in MR images: Method and validation, Ieee Transactions on Medical Imaging, 13 (1994) 716-724.